THERMOGRAPHIC ANALYSIS OF HEAT GENERATION DURING UCS TESTING OF ROCKS

A THESIS SUBMITTED TO
THE GRADUATE SCHOOL OF NATURAL AND APPLIED SCIENCES
OF
MIDDLE EAST TECHNICAL UNIVERSITY

BY

ALPER KIRMACI

IN PARTIAL FULFILLMENT OF THE REQUIREMENTS
FOR
THE DEGREE OF MASTER OF SCIENCE
IN
MINING ENGINEERING

JANUARY 2020

Approval of the thesis:

THERMOGRAPHIC ANALYSIS OF HEAT GENERATION DURING UCS TESTING OF ROCKS

submitted by **ALPER KIRMACI** in partial fulfillment of the requirements for the degree of **Master of Science in Mining Engineering Department, Middle East Technical University** by,

Prof. Dr. Halil Kalıpçılar
Dean, Graduate School of **Natural and Applied Sciences** _____

Prof. Dr. Naci Emre Altun
Head of Department, **Mining Engineering** _____

Assist. Prof. Dr. Mustafa Erkayaoğlu
Supervisor, **Mining Engineering, METU** _____

Examining Committee Members:

Prof. Dr. Celal Karpuz
Mining Engineering Department, METU _____

Assist. Prof. Dr. Mustafa Erkayaoğlu
Mining Engineering, METU _____

Prof. Dr. Bahtiyar Ünver
Mining Engineering Department, HU _____

Date: 10.01.2020

I hereby declare that all information in this document has been obtained and presented in accordance with academic rules and ethical conduct. I also declare that, as required by these rules and conduct, I have fully cited and referenced all material and results that are not original to this work.

Name, Surname: Alper Kırmacı

Signature:

ABSTRACT

THERMOGRAPHIC ANALYSIS OF HEAT GENERATION DURING UCS TESTING OF ROCKS

Kırmacı, Alper
Master of Science, Mining Engineering
Supervisor: Assist. Prof. Dr. Mustafa Erkayaoğlu

January 2020, 149 pages

Mining activities concentrate on the production of underground resources for energy generation and raw material requirements worldwide, as it is also the case in Turkey. For this reason, the exploration of new resources proceeds consistently to meet the increasing raw material demand of the industry. Rock mechanics has a vital role in underground mining and surface mining. At present, the devices and instruments used in rock mechanics laboratory testing, for example, uniaxial compressive strength test, have inferior sensing capability of the initial formation of cracks. Therefore, some inferences must be made by analyzing the data collected during tests. However, this effort cannot be supported with crucial and reliable visual data at the initial crack formation. Regarding this, in this thesis study, the failure behavior of different types of rock specimens was analyzed by a thermal camera during uniaxial compressive strength tests. Hence, this thesis study is expected to become one of the current studies in rock mechanics literature. Therefore, it is foreseen that this subject will make a significant contribution to literature. The experiment results show that gneiss-schist specimens have greater uniaxial compressive strength values than andesite samples. Temperature increase at the failure moment was detected as 4.45 ℃ and 9.58 ℃ for andesite and gneiss-schist specimens, respectively. Higher temperature increase was observed with respect to UCS value. Besides, a temperature decrease was recorded

during marble specimens. The amount of temperature decrease was detected about 0.5-0.6 ℃. The temperature change at the specimen causes the radiation energy release. As a result of the porosity tests, it was observed that increase in the porosity rate is parallel to higher radiation energy released, from 17.72 kJ to 107.81 kJ.

Keywords: Rock Mechanics, Temperature Effects, Laboratory Experiments, Thermography Images, Infrared Thermal Camera

ÖZ

TEK EKSENLİ BASINÇ DAYANIMI DENEYİ SIRASINDA KAYALARIN ISI OLUŞUMUNUN TERMOGRAFİK ANALİZİ

Kırmacı, Alper
Yüksek Lisans, Maden Mühendisliği
Tez Danışmanı: Dr. Öğr. Üyesi Mustafa Erkayaoğlu

Ocak 2020, 149 sayfa

Madencilik faaliyetleri ülkemizde olduğu gibi dünya çapında da yer altı kaynaklarına yönelik hem enerji üretimi hem de hammadde gereksinimi nedeniyle yoğunlaşmaktadır. Bu sebepten ötürü, sanayinin artan hammadde talebinin karşılanması amacıyla madencilikte yeni kaynak arayışları sürekli olarak devam etmektedir. Madencilik faaliyetlerinin temel olarak gerçekleştirildiği yeraltı ve yer üstü işletmelerinde kaya mekaniği önemli bir paya sahiptir. Günümüzde kaya mekaniği deneylerinde kullanılan, örneğin tek eksenli basma dayanımı deneylerin de, cihaz ve ekipmanların ilk çatlak oluşma anını algılama yetenekleri oldukça düşüktür. Bu nedenle, deney sırasında kayıt altına alınan veriler incelenerek bazı çıkarımlar yapılmak zorunda kalınmaktadır. Ancak bu çıkarımlar, ilk çatlak oluşum anına dair güvenilir ve hassas bir görsel veriyle desteklenememektedir. Buna ilişkin olarak, bu tez çalışmasında farklı tip kaya örneklerinin tek eksenli basınç deneyleri sırasında yenilme davranışları termal kamera ile izlenmiştir. Bu sayede, söz konusu tez çalışmasının kaya mekaniği literatüründeki güncel çalışmalardan birisi olarak literatüre büyük ölçüde katkıda bulunacağı öngörülmektedir. Yenilme anındaki sıcaklık artışı andesite ve gnays-şist numuneleri için sırasıyla 4.45 ℃ ve 9.58 ℃ olarak tespit edilmiştir. Bu nedenle, UCS değerindeki artış ile birlikte daha yüksek

sıcaklık artışı görülmüştür. Ayrıca, mermer numunelerinde deney sırasınca sıcaklık değerinin düştüğü görülmüştür. Sıcaklık düşüşündeki değer yaklaşık olarak 0.5-0.6 ℃ civarında görülmüştür. Örnekteki sıcaklık değişi ışınım enerjisi salınımına neden olmaktadır. Yapılan porozite deneyleri sonucunda, gözeneklilik oranındaki artış ile birlikte enerji salınımının da 17.72 kJ'dan 107.81kJ'a kadar yükseldiği görülmüştür.

Anahtar Kelimeler: Kaya Mekaniği, Sıcaklık Etkisi, Laboratuvar Deneyleri, Termografi Görüntüleri, Kızılötesi Termal Kamera

To my wife and my family

ACKNOWLEDGEMENTS

I would like to express my deepest gratitude to my advisor Assist. Prof. Dr. Mustafa Erkayaoğlu for his valuable support, encouragement and his guidance. I am also grateful to my committee members Prof. Dr. Celal Karpuz and Prof. Dr. Bahtiyar Ünver. I would also like to extent my thanks to Assist. Prof. Dr. Ali İmer for his help.

I would like to thank Hakan Uysal for his support, help and his guidance during laboratory works.

I am sincerely thankful to my dearest friend Kutay Emre Karadeniz for his encouragement and help during my work. I would like to thank Doğukan Güner for his guidance and support. I want to extent my thanks to Dr. Selin Yoncacı for her help and guidance. I want to thank my friends Firuz Can Arı, Adil Aras Nuray, Hamdi Gurur Çelebi, Ege Karaman and Miraç Eren Aydoğan for their friendship and support during my study. Finally, I also thank all my colleagues Cengiz Kaydım, Ceren Karataş Batan, Enver Yılmaz, and Merve Özdemir Aydın for their help and friendship.

I must thank all administrative, academic, and technical staff of the Department of Mining Engineering, METU, for their support during my education.

Finally, I am immensely grateful to my wife Fahriye Nur Kırmacı, my mother Filiz Kırmacı, my sister Özge Canşe and my father Ahmet Kırmacı for their love and supports. This thesis study could not be completed without their encouragement and belief. I dedicate this thesis study to them.

TABLE OF CONTENTS

LIST OF TABLES

TABLES

LIST OF FIGURES

FIGURES

LIST OF ABBREVIATIONS

ABBREVIATIONS

m	Meter
mm	Millimeter
μm	Micrometer
k	Thermal conductivity coefficient
A	Applied force area of the sample
d	Diameter of the sample
h	Height of the sample
ΔT	Temperature change
Δt	Elapsed Time
^{o}C	Celsius
s	Second
N	Newton
J	Joule
Pa	Pascal
UCS	Uniaxial Compressive Strength
LWIR	Longwave Infrared
DIC	Digital Image Correlation
σ_c	Uniaxial Compressive Strength
F_c	Failure Load
P_v	Pore Volume

W_{sat}	Saturated Weight
G_w	Mineral Weight
ρ_w	Water Density
B_v	Bulk Volume
n_{eff}	Effective Porosity
μ_g	Grain Density
μ_d	Dry Density
n_{tot}	Total Porosity
E	Young's Modulus
N	Poisson's Ratio
LVDT	Linear Variable Differential Transformer

CHAPTER 1

INTRODUCTION

Mining activities primarily aim the extraction of resources for energy generation and raw material requirements. There is a global trend of operating underground operations due to the scarcity of remaining shallow resources, as it is also the case in Turkey. For this reason, exploration of new resources is continuously in progress, aiming to meet the increasing demand for raw material of humankind. These exploration activities led to the discovery of new resources and enabled the development of underground mining activities that have to be more efficient and safer. For these reasons, the utilization of innovative technologies is always a necessity for the mining industry related to all stages of production, including the engineering studies performed before operation, such as geotechnical studies.

Rock mechanics is a field of research that analyses the behavior of rocks under stress and tension conditions. It has an essential role in tunneling activities, underground and surface mining. It is commonly the basis of various engineering studies, such as the design of underground openings, bench stability, tunneling activities, dam construction, or storing nuclear waste in rock settings (Deb and Verma, 2016). Theoretical studies of rock mechanics started at the beginning of the 1900s (Ulusay et al., 2016), and it is known that there are still points that could be improved related to the integration of new technologies both on laboratory scale and in field studies. As an example, researchers investigate the behavior of crack and failure with the help of current technologies such as high-speed cameras (Zhang and Zhao, 2014; He et al., 2015 Yin et al., 2015; Akdag et al., 2018), thermal infrared cameras, DIC systems (Ghabraie et al., 2015; Belrhiti et al., 2017; Patel and Martin, 2018) and acoustic emission systems (Young and Collins, 2001; Read, 2004; Cai and Kaiser, 2005, Aydan and Ulusay, 2013). This thesis study focuses on the thermal imaging of different types

of rock specimens during UCS determination in a displacement-controlled testing environment. The detection of the failure behavior of the rock specimens is performed by an uncooled LWIR thermal camera. The heat dissipation during failure is detected by thermographic analysis with a thermal camera.

The literature research conducted for this thesis study revealed that recent studies in this field are mostly focused on using high-speed cameras and DIC systems. Therefore, this thesis study can be considered as part of the up-to-date research in rock mechanics literature and it is expected to contribute to this field by implementing thermal cameras for laboratory testing of rocks. In this context, it will provide an opportunity to utilize available technology to improve the existing knowledge related to the detection of crack initiation points, crack propagation, crack coalescence, and failure behavior of rocks.

1.1. Problem Statement

Rock mechanics is an engineering discipline continuously developed by the integration of new technologies. As a result of the literature research on the applications of rock mechanics, it was noticed that majority of current studies in this field were performed by using high-speed cameras and DIC systems. It is known that most of the measurement equipment still used in rock mechanics experiments, such as the UCS test or indirect tensile strength (Brazilian) tests has a low ability to detect the first crack formation on the sample and failure behavior of the samples. This leads to the necessity of making some inferences regarding the crack formation and failure behavior during the conducted experiments. However, these inferences cannot be supported by reliable and detailed visual data at the moment of the failure and crack formation. To support this visual deficiency, the failure behavior of rock samples was investigated and recorded by a thermal infrared camera during UCS tests. In addition to this, the stress-strain graphs obtained from UCS tests can be used to measure the total energy generated by the rock specimens. The thermal infrared camera can support the information about energy generation indirectly by providing the thermal change in

the sample. This knowledge can provide information about the rate of the thermal energy released out of the total energy generated by the sample.

1.2. Research Objectives

This thesis study aims to obtain reliable and accurate data about the failure behavior of rock samples during UCS testing and to analyze the energy produced during UCS testing. Different types of rock samples were used for the experimental studies within the scope of the thesis study. As a result of the experiments, UCS values, stress-strain relationships, and thermographic results were obtained. With the help of the thermal infrared camera, initial crack formation, failure behavior, and the generated energy amounts were examined. During experiments, the MTS 815 Test system and COX thermal infrared camera were used.

1.3. Research Methodology

The research methodology consists of the steps summarized below;

- Literature research
- Training for the thermal camera hardware and software
- Preparation of rock samples for the experiments
- Performing static deformability, indirect tensile strength and UCS tests and recording of the result with the thermal camera
- Determination of true and relative porosity of rock samples
- Thin section from the failure plane of the specimen
- Analysis of the test results

1.4. Thesis Outline

This thesis study consists of 5 chapters and three appendices. Chapter 1 provides general information about the thesis covering problem statement, objectives of the study, and methodology of the study. In Chapter 2, literature research of the thesis

study is provided. Chapter 3 explains the methodology followed for the experimental study. In this section, information about the thermal camera and testing system is given. In Chapter 4, the test results are evaluated and analyzed. Finally, the conclusion and some recommendations are provided in Chapter 5.

Appendix A provides photos of the rock samples before the experiment and after the experiment. In Appendix B, the thermal images of the rock samples can be seen. The temperature increases for each sample during the failure moment is indicated on these images. Finally, Appendix C covers the analysis of the experiments and stress-strain graphs, force- temperature difference- time graphs.

CHAPTER 2

LITERATURE REVIEW

The analysis of rock mechanics experiments with various instrumentation is concentrated on different researchers using thermal cameras for different purposes. Summary of the previous studies related to the thermal camera usage in rock mechanics experiments is summarized in Table 2.1.

Table 2.1. *Summary of the literature review related to thermal camera usage in rock mechanics*

Researchers	**Year**	**Subject**
Wu et al.	2006	Usage of thermal camera in rock mechanics laboratory experiments
Aydan et al.	2014	
Liu et al.	2016	
Pappalardo et al.	2016	
Wang et al.	2016	
Mineo and Pappalardo	2016	
Antony et al.	2017	
Aydan et al.	2017	
Salami et al.	2017	
Li et al.	2018	
Qin et al.	2018	
Lou and He	2018	
Wang et al.	2018	
Gong et al.	2012	Modeling of the physical environment of the mining area to be laboratory scale and carrying out related experiments
Gong et al.	2015	
Sun et al.	2017	
Sun et al.	2018	

According to Table 2.1, some researchers created a physical environment of the mining area the laboratory scale (Gong et al., 2015, 2018; Sun et al., 2017, 2018). In addition to this, some researchers analyzed the rock behavior by thermal cameras during experiments. They used different types of rock for different testing purposes. (Antony et al., 2017; Aydan et al., 2014; Lou & He, 2018; Liu et al., 2006; Tan et al., 2007; Wu et al., 2006; Pappalardo et al., 2016; Wang et al., 2016).

Antony et al. (2017) had the objective to estimate the initiation point of the crack by changing the V-shape chevron of the notch angle in sandstone samples. For this purpose, a thermal imager was used and a relationship between the zones where temperature increased and the crack initiations points were investigated. The point load test methodology was followed for the experiments to initiate the crack. Because of the large number of particles in the sandstone, stress distribution and stress transfer between particles could be seen clearly by the thermal camera. Therefore, usage of the sandstone samples in the experiments provided advantages during experiments and analysis. Notch angles of 40° and 45° were used respectively, and the zones where temperature increased and crack initiation points were examined. From the loading area to the bottom of the sample, 5 points were identified and numbered from 1 to 5 top to bottom. As a result of the experiments, the temperature concentration and crack initiation point of the sample with a notch angle of 40° was observed at number 1, that is, the loading area (Figure 2.1). An increase of approximately 2 ℃ was observed in the crack initiation region.

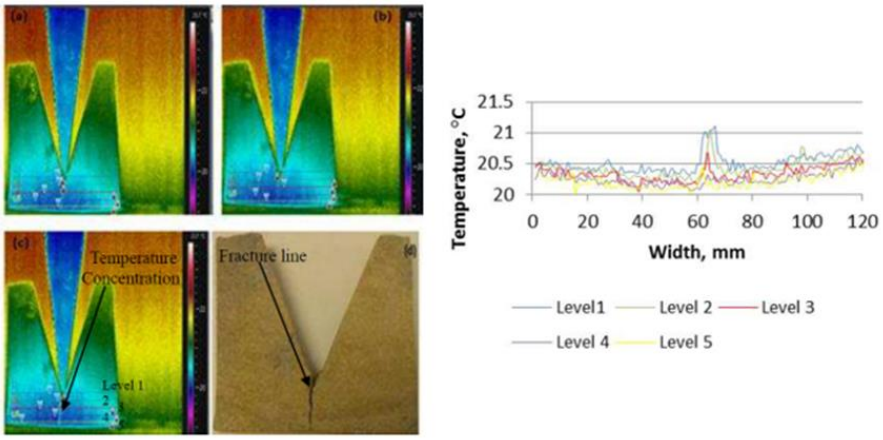

Figure 2.1. Loading and crack initiation moment and temperature profile of the chevron sample with 40° notch angle (Antony et al.2017)

Similarly, the sample with a notch angle of 45° was tested under loading conditions, and the temperature increase was again observed at point 1. An increase of 18 ℃ was observed in the crack initiation region. There was a sudden increase in the temperature value together with the increase of the notch angle. The reason of this phenomenon is explained by the formation of multiple cracks with an increased notch angle (Antony et al., 2017). Figure 2.2 shows the temperature increase at the crack initiation point of the sample with a notch angle of 45°.

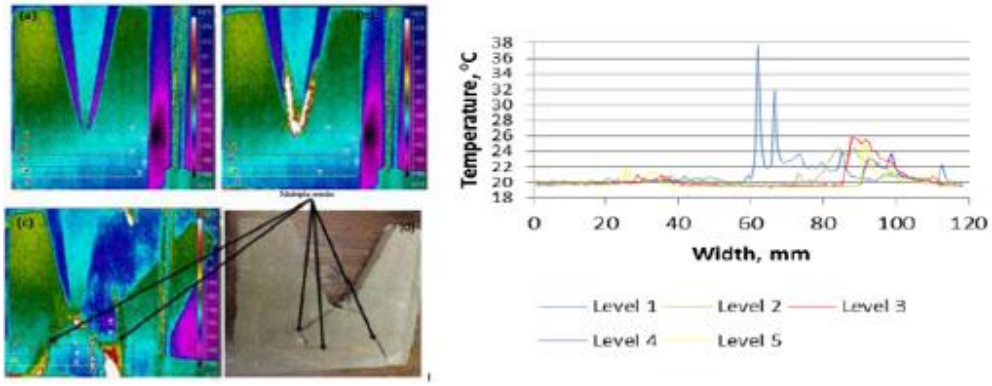

Figure 2.2. Loading of multiple crack initiation of the chevron sample with a notch angle of 45° and temperature profile (Antony et al.2017)

Li et al. (2018) investigated the risks that may occur due to temperature increase and gas pressure in coal by thermal imager systems. Coal samples were placed into

airproof cylinders and the samples were subjected to lateral pressure through gas. In addition to the lateral pressure, the uniaxial load was applied to the system. By the usage of the gas pressure, it was aimed to expand the cracks due to triaxial loading and create new temperature increase zones. For this purpose, the experiments, as shown in Figure 2.3, were monitored with a thermal imager. Light color regions represent the higher temperature value of the sample. 50 N/s load was applied for uniaxial load and the gas pressure was fixed at 0.2 MPa for the experiments. As a result of the study, the actual cracks started to form at 1047.9 seconds, as it can be seen in Figure 2.4. Accordingly, temperature of the coal samples was decreased slightly during experiment. As the loading progressed, the temperature value was sharply increased at the failure.

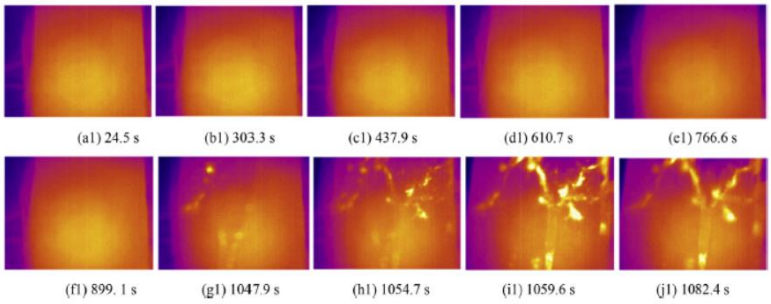

Figure 2.3. Investigation of loading moment and temperature changes with a thermal imager (Li et al., 2018)

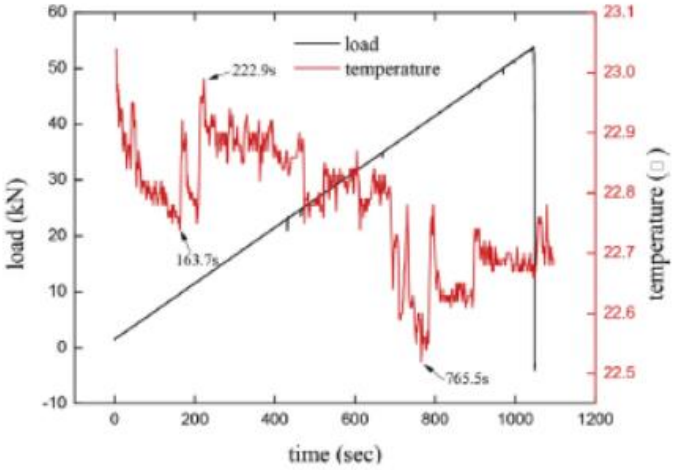

Figure 2.4. Load- Temperature- Time graph (Li et al., 2018)

It can be understood from the sudden drop in the load-time and temperature-time graph that the failure occurred within this second. From the thermal camera image, the temperature change in the crack can be seen at this second. In addition, the effect of the gas used in the lateral pressure application process on the crack was investigated with the thermal imager as seen in Figure 2.5, and the effect of the gas released from the cracked regions and the pressure formed was again examined with the thermal imager. As a result, gas pressure causing damage on the samples was determined.

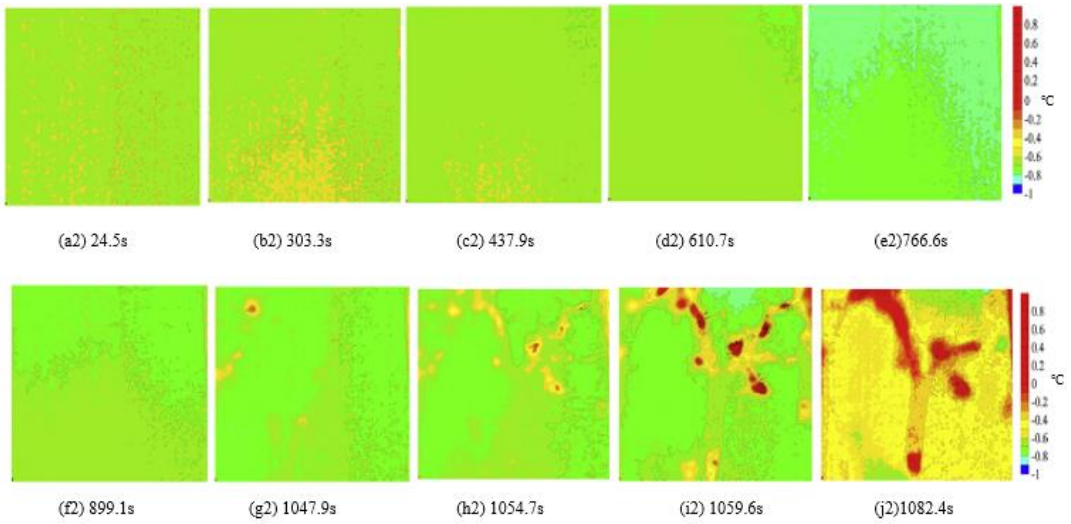

Figure 2.5. Effect of the gas pressure on the sample (Li et al., 2018)

Qin et al. (2018) investigated the formation and properties of cracks caused by the cooling behavior of liquid nitrogen by injecting it into coal samples. Triaxial tests were performed and as a result, the difference between a single injection and cyclic injections was demonstrated. Liquid nitrogen is capable of descending to -196 °C (Cai et al., 2014). Therefore, liquid nitrogen was used as a refrigerant and the behavior of the specimen was examined by the thermal camera. As it can be seen in Figure 2.6, the liquid volume increased by 9% in the pores due to the freezing in the single injection, while this ratio increased with cycling injection and caused multiple crack formations.

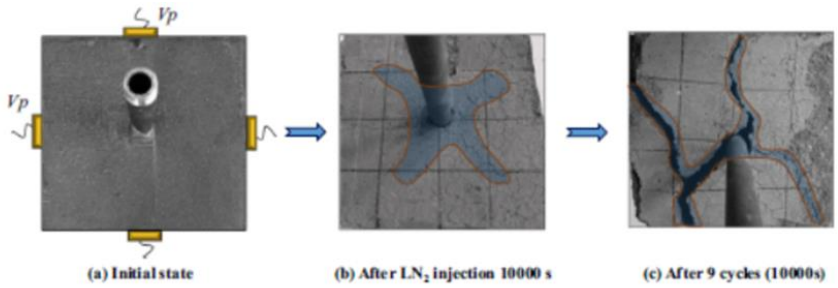

Figure 2.6. Investigation of crack formation by injecting liquid nitrogen during the triaxial test (Qin et al., 2018)

The difference between the cooling behavior between a single injection and cyclic injections was examined by the thermal camera and it was found that liquid nitrogen filled the formed crack and cooling was only observed in this area. In contrast, as a result of nine cycles of injecting, liquid nitrogen was injected into the sample at regular intervals, so the nitrogen spread into all crack formations. Hence, the same cooling behavior was observed on all surfaces, not just in one region of the sample.

As shown in Figure 2.7, only the lower part of the sample cooled as a result of the single injection, and this cooling amount was recorded down to -19.47 ℃. As a result of the 9-cycle injections, the whole sample was cooled down and this cooling amount was recorded as low as -176.65 ℃. Consequently, the effect of cooling on the crack formation and the crack propagation was investigated.

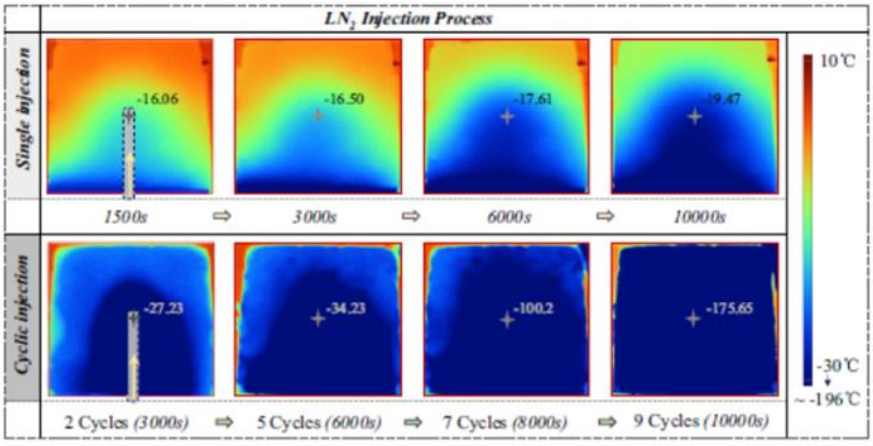

Figure 2.7. Cooling behavior difference between single and 9-cycle injection (Qin et al., 2018)

Lou and He (2018) examined the crack formation and propagation of cracks during UCS testing of concrete samples. For this purpose, it was aimed to specify the possible crack formation regions by evaluating the temperature increasing areas using thermal cameras. By increasing the amount of load over time, the formation of cracks from the temperature increase regions was determined, as shown in Figure 2.8.

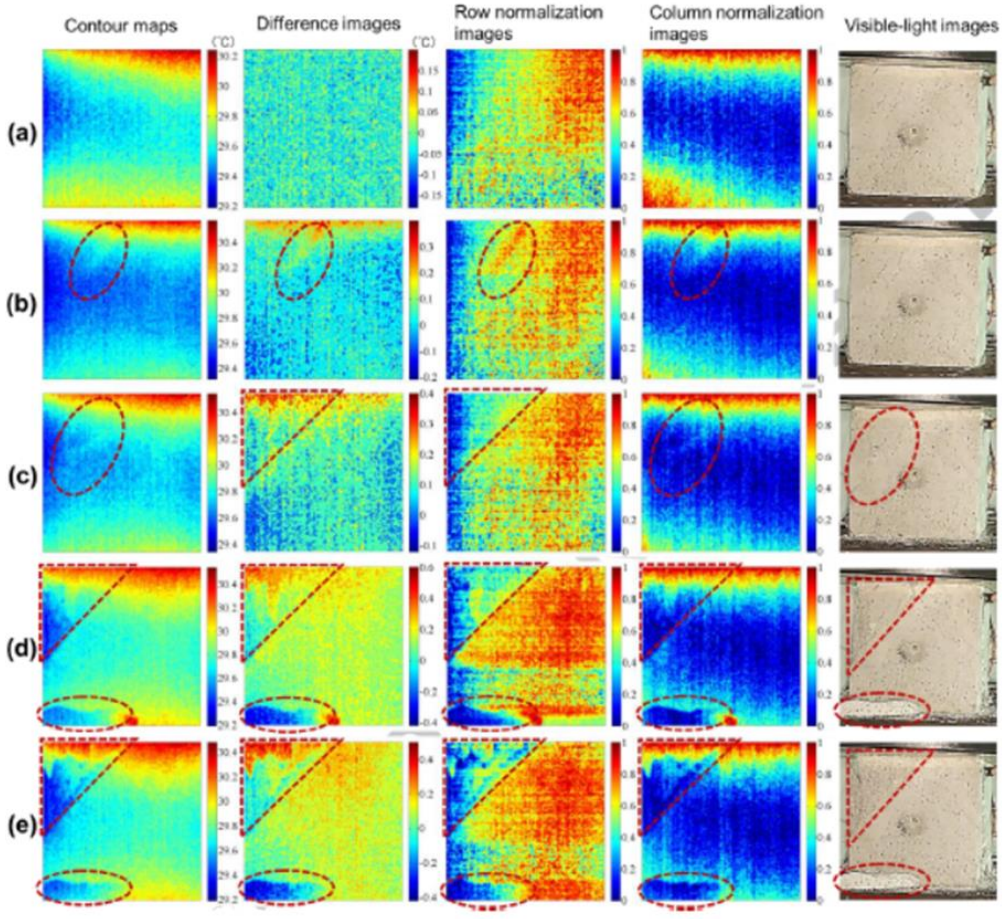

Figure 2.8. Different loading amounts and temperature increase regions; a) time: 6s, load ratio: 0.5% b) time:115s, load ratio: 66.6%, c) time: 155s, load ratio: 89%, d) time: 197s, load ratio: 88.2%, e) time:246s, load ratio: 32.1% (Lou & He, 2018)

The same experiments were performed on different concrete samples, and all of them showed failure zones within the temperature increasing zones (Figure 2.9). As a result

of the experiments, it was concluded that a thermal imager could be an essential tool used to detect the crack formation and examination of the propagation of cracks.

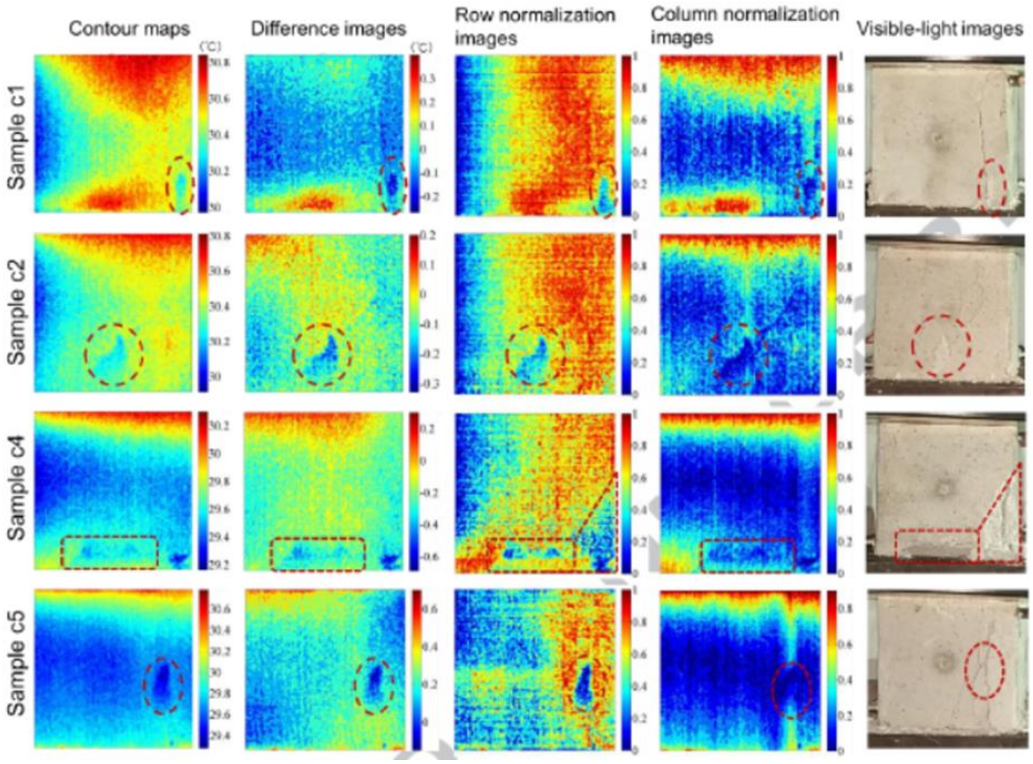

Figure 2.9. Detection of crack formation areas in different concrete samples by the thermal camera (Lou & He, 2018)

Liu et al. (2006) examined the failure characteristics of rock samples by using different types of rock in various experiments. During these experiments, the failure zones and their properties were examined with the help of the thermal camera. UCS tests were performed on marble and gabbro, and their failure behavior at the failure was compared. As a result of the experiments, the temperature increases in the gabbro samples were recorded as instantaneous and higher than the recordings of the marble samples. This behavior is explained by the fact that gabbro is more brittle than marble. Since gabbro was more brittle than marble, the level of noise generated during the failure was also higher than the level of noise recorded during the failure of marble. Figures 2.10 and 2.11 show the moment of failure and temperature increase of marble and gabbro, respectively.

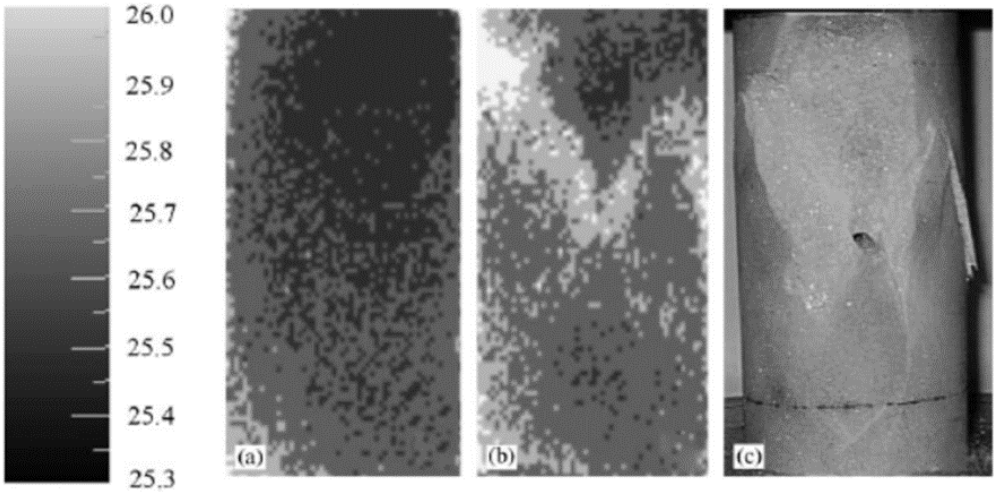

Figure 2.10. Thermal images of marble samples during loading and failure moment (Liu et al., 2006)

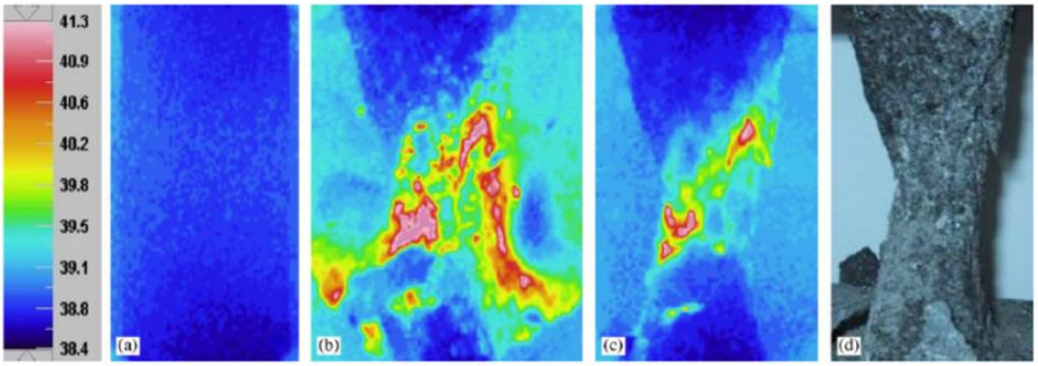

Figure 2.11. Thermal images of gabbro samples during loading and failure moment (Liu et al., 2006)

After the UCS experiments on marble and gabbro samples were completed, a three-point bending test was conducted on granodiorite samples, and the properties at failure caused by the tensile force were investigated. The thermal camera recorded these behaviors, and the temperature increase on the failure surface did not change significantly because of the tensile failure; however, the temperature increase was seen in the contact area between the sample and contact. In Figure 2.12, the regions with temperature increase during the three-point bending experiments can be seen.

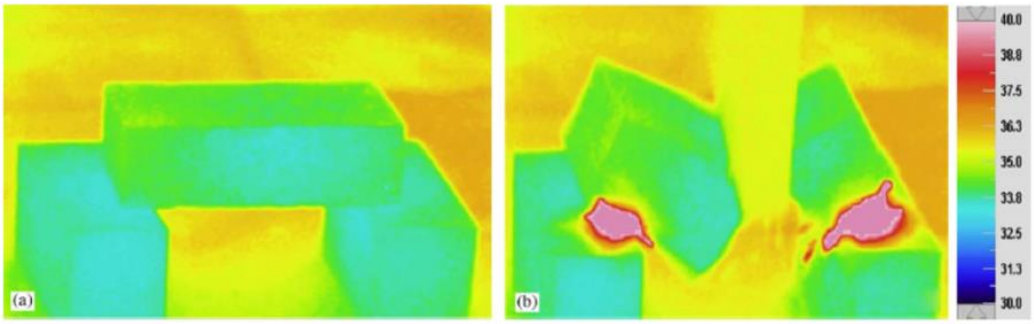

Figure 2.12. Three-point bending test of granodiorite samples and thermal image (Liu et al., 2006)

Aydan et al. (2017) studied the problems around tunnels by a thermal camera and aimed to identify the areas that would be affected by possible failure regions. UCS tests were performed on andesite samples taken from Sinop region (Figure 2.13). As a result of the experiments, heat dissipation was observed in the failure regions. These results have contributed to the researchers' determination of rock failure, where the temperature around the tunnel increased.

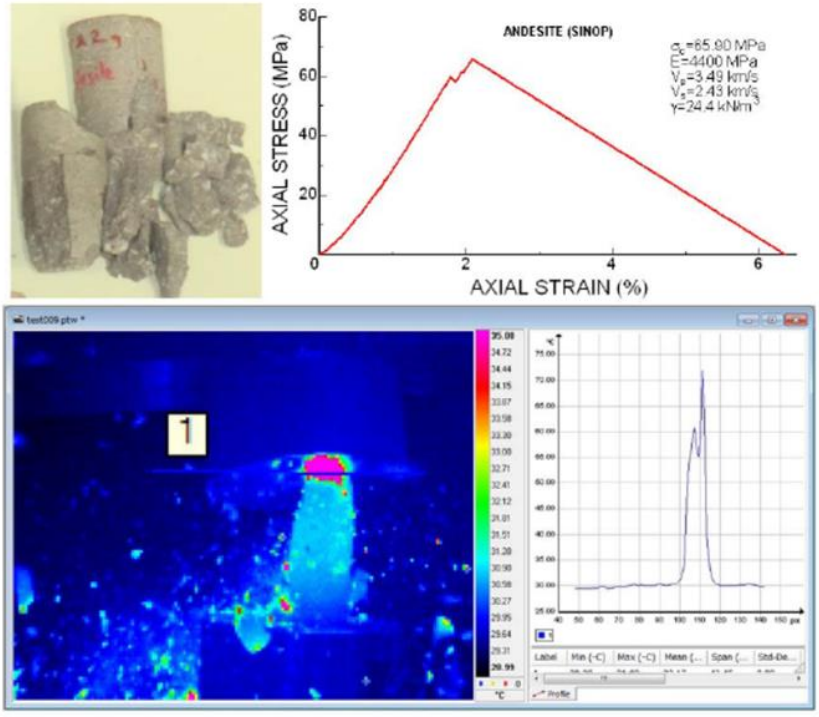

Figure 2.13. Temperature increase regions of Sinop Andesite as a result of the uniaxial compression test (Aydan et al., 2017)

Afterward, UCS tests were performed with samples taken from the Tarutoge tunnel in Japan, and the results were monitored with a thermal camera. As shown in Figure 2.14, holes were drilled in the center points of the samples. Then, the relationship between the regions where the rock failure occurred and the temperature increase was investigated. As a result of the experiment, high-temperature regions were specified in the areas where the failure occurred. As the stress increased, these regions became more extensive, and cracks began to form. After the formation of the cracks in these regions, the temperature began to decrease. The reason for this is the heat release from these cracks. The thermal camera captured these behaviors of the rock. It has been stated that the use of the thermal camera is an effective method for ensuring safety and stability for engineers working in the geotechnical field.

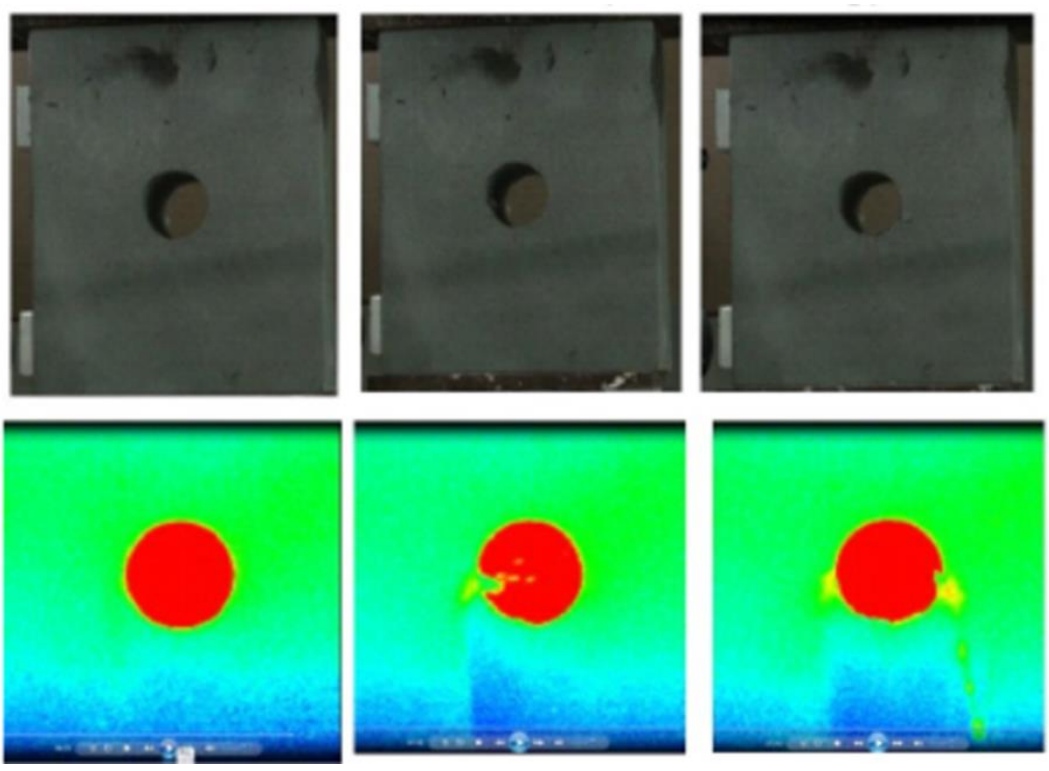

Figure 2.14. Thermal image of the rock sample (Aydan et al., 2017)

Besides, some investigations were made with a thermal camera in tunnel construction (Figure 2.15). As a result of these investigations, it has been observed that many incidents cannot be seen with the naked eye due to dust, such as the stress discharge and water leakage areas. It has been stated that thermal cameras are enabling a useful aspect of thermal camera usage.

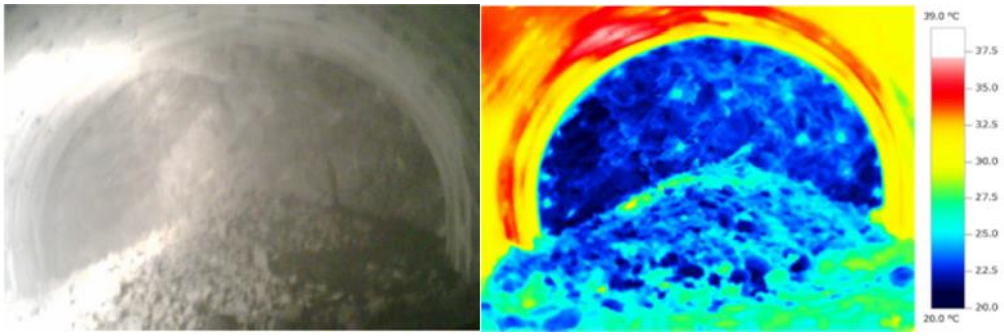

Figure 2.15. Visual and thermal image of the tunnel immediately after the blasting (Aydan et al., 2017)

Wang et al. (2018) conducted UCS tests on concrete samples and examined the results with the help of a thermal camera. The experiment was performed on cylindrical specimens of 50 mm diameter and 100 mm length (Figure 2.16). As a result of the experiment, it was observed that the temperature in the sample first increased from 11 ℃ to 11.5 ℃. After the failure, the temperature decreased to 10.95 ℃ due to the heat release from the cracks.

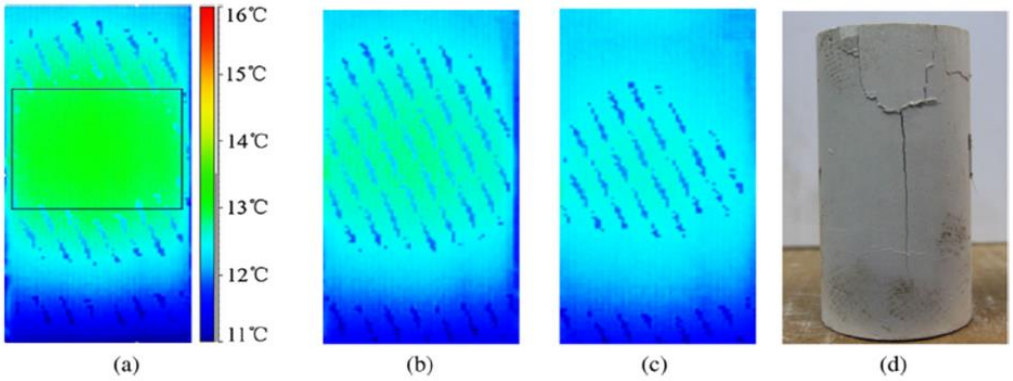

Figure 2.16. Investigation of the uniaxial compressive strength test result of cylinder concrete sample by the thermal camera; a) Before Loading b) Before Failure c) After Failure d) Visual Image of Sample After Failure (Wang et al., 2018)

Following these tests, UCS tests were applied on concrete slabs with cylindrical cavities and the results were re-evaluated (Figure 2.17). A thermographic analysis was carried out at specific time intervals. Initially, the slab was in one piece and after a particular time, the first excavation process was performed. Later, the excavated area was filled, and it represented the excavated area. Finally, the excavation was performed again by filling material. During the test, temperature changes were recorded by the thermal camera.

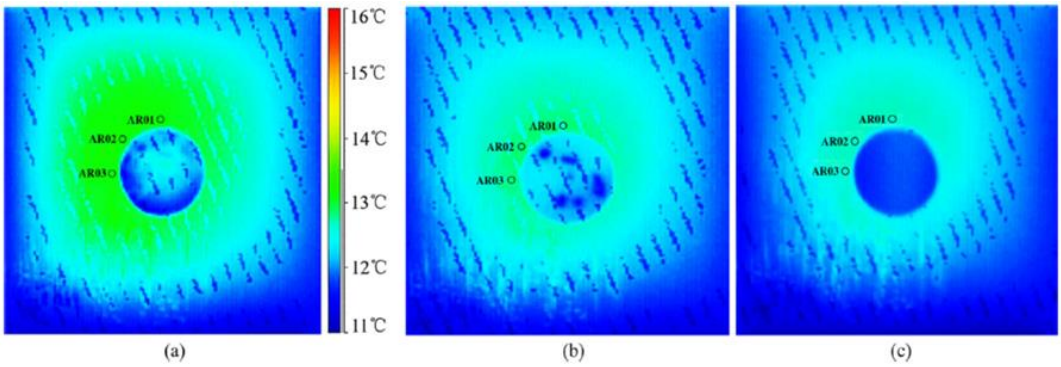

Figure 2.17. Investigation of uniaxial compressive strength test results in the concrete slab with the thermal camera; a) Preload phase b) First excavation (660 seconds) c) Second excavation (1180 seconds) (Wang et al., 2018)

As a result of the experiments, it has been observed that the temperature decreased from 13 ℃ to 12.7 ℃ on the concrete slabs during the preload phase. After the first excavation, the temperature dropped to 12.5 ℃ whereas during the filling process, the temperature increased to 12.8℃. As a result of the second excavation, the temperature decreased to 12.3 ℃ which can be concluded as, except for the filling stage, the temperature values decreased during the UCS tests performed on the concrete samples.

Aydan et al. (2014) examined the failure behavior of the different types of rocks by performing various mechanical experiments. It has been observed that a measurable amount of thermal energy is released at the failure points that can be measured by thermal cameras and this information could be used to determine critical regions being prone to concepts such as rockburst or rock squeezing.

Initially, UCS tests were performed on low strength rocks, claystone samples taken from the Seyitömer region were evaluated according to the temperature change behavior of the test results (Figure 2.18). It was mentioned that the temperature increasing regions indicated the crack initiation regions. Besides, failure of rock specimens started in these regions. Similarly, it was mentioned that the region characterized by a temperature increase in tuff samples taken from Sinop clearly indicated the failure plane (Figure 2.19).

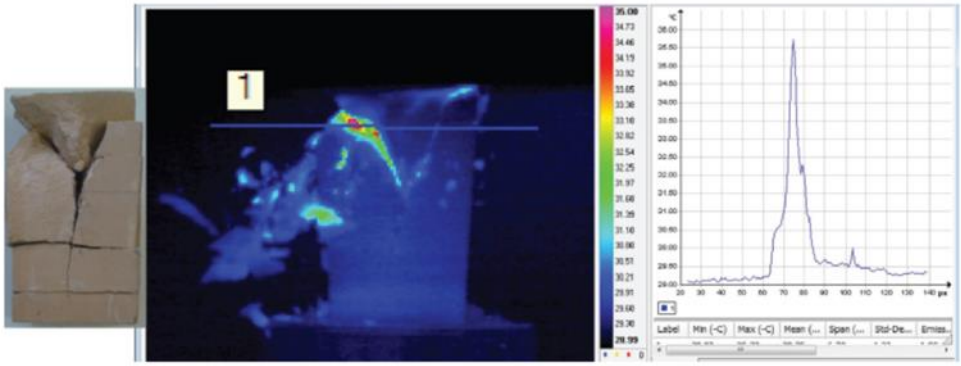

Figure 2.18. Visual and thermal image of Seyitömer Claystone and graph of temperature change along the selected line (Aydan et al.,2014)

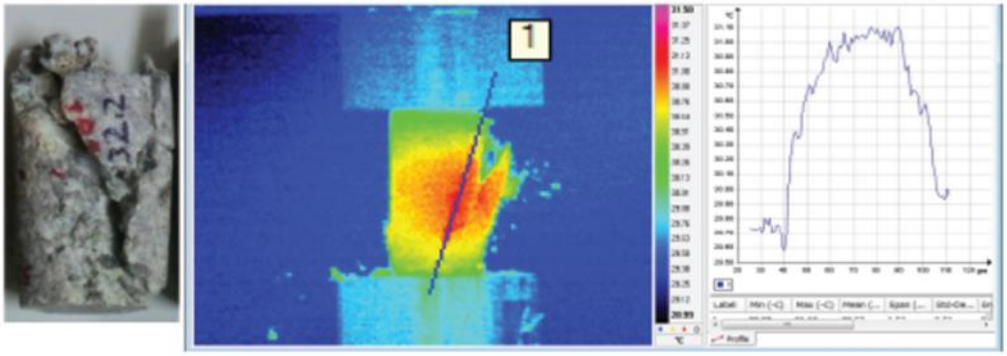

Figure 2.19. Visual and thermal image of Sinop Tuff and graph of temperature change along the selected line (Aydan et al.,2014)

In a similar way, UCS tests were also performed on medium strength rocks, and the tests were monitored with a thermal camera. As shown in Figure 2.20, about 5 ℃ temperature increase between the contact area and the test equipment was observed for the marble samples taken from the Kuşini region. As a result of the experiments,

failure was observed in two different regions, and the temperature increase in these regions reached up to 33 ℃ for the sandstone samples from the Ehime region (Figure 2.21).

Figure 2.20. Visual and thermal image of Kuşini marble and temperature change along the selected line (Aydan et al., 2014)

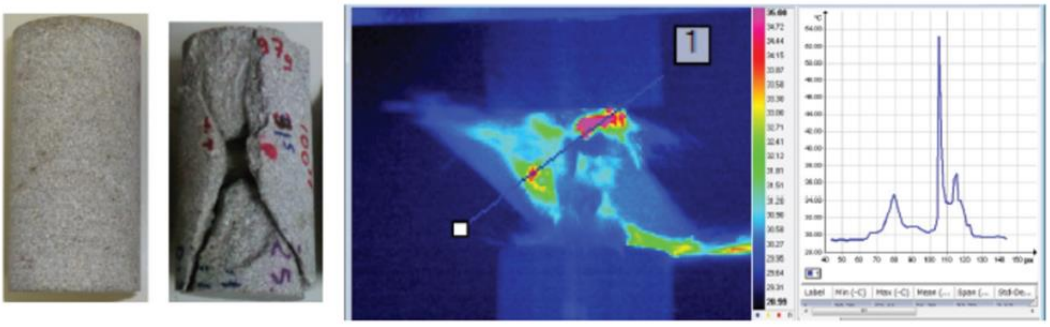

Figure 2.21. Visual and thermal image of the Ehime Sandstone and temperature change along the selected line (Aydan et al., 2014)

Finally, UCS tests were performed on high strength rocks, such as andesite samples from the Sinop region that resulted in lots of cracks along the failure plane (Figure 2.22). Temperature increase reached up to 42℃, and due to the catastrophic failure of the specimen, rock fragments burst out of the sample. Granite samples that were taken from the Ehime region also indicated a temperature increase of up to 47 ℃ (Figure 2.23).

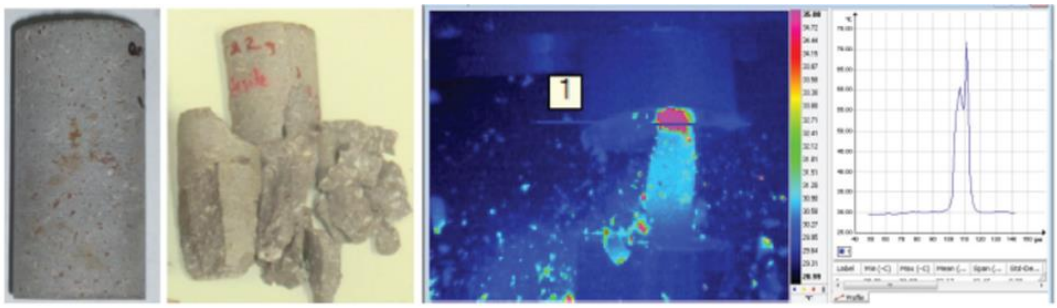

Figure 2.22. Visual and thermal image of Sinop Andesite and temperature change along the selected line (Aydan et al., 2014)

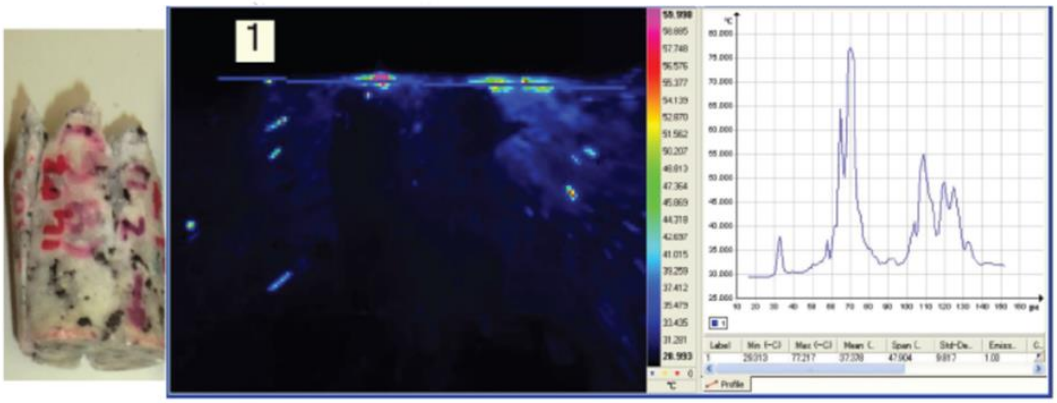

Figure 2.23. Visual and thermal image of Ehime granite and temperature change along the selected line (Aydan et al., 2014)

In addition to the UCS tests, indirect tensile strength tests were performed on samples, and a thermal camera recorded the complete test duration. As a result of the experiments carried out in the granite samples taken from the Ehime region, it was observed that high-temperature bands were formed close to the failure planes (Figure 2.24). Besides, the crack initiation points were found to be related to the highest temperature points. As a result of the experiments with rhyolite samples taken from the Kaore region, similarities were found with the findings of the test results of granite samples (Figure 2.25). It was also observed that the temperature difference in rhyolite samples was higher than the temperature difference in granite samples.

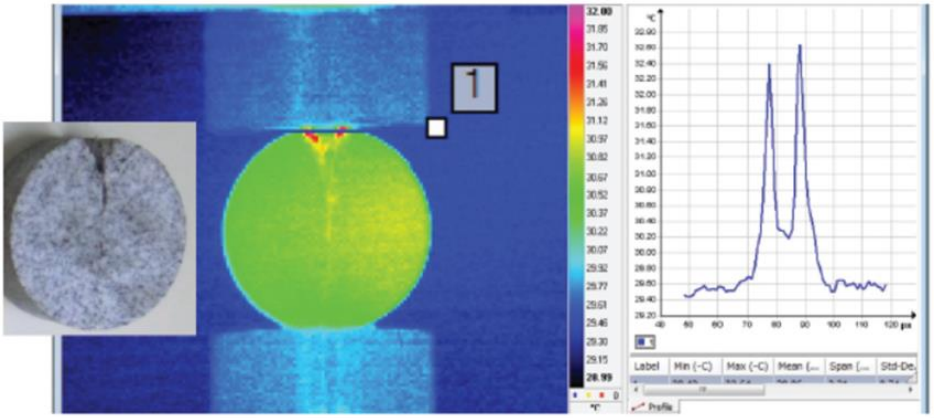

Figure 2.24. Investigation of indirect tensile strength test results of Ehime granite by thermal camera and graph of temperature change along the selected line (Aydan et al., 2014)

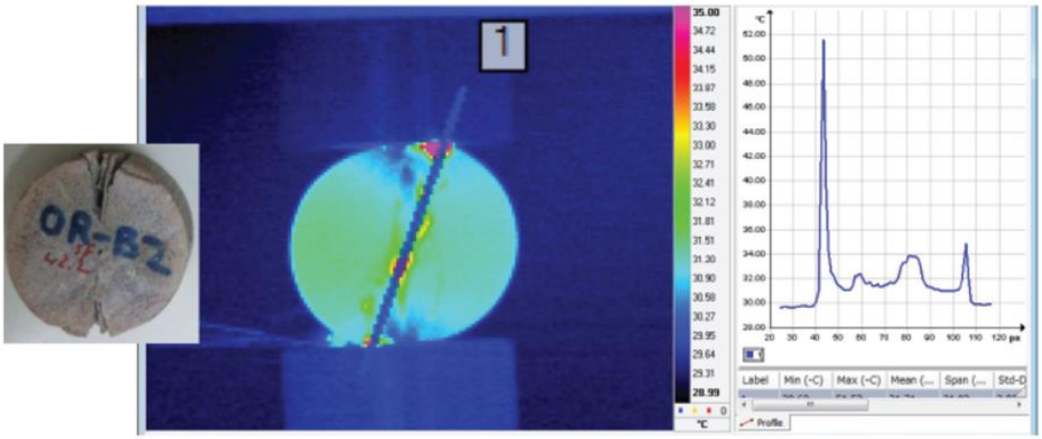

Figure 2.25. Investigation of indirect tensile strength test results of Kaore rhyolite by thermal camera and graph of temperature change along the selected line (Aydan et al., 2014)

Hence, as the strength of the rock samples increased, the temperature increase was higher in the temperature change region where the failure plane was formed. Besides, it was observed that the samples exhibited a more brittle behavior during failure with increasing strength values.

Wu et al. (2006) examined the failure patterns of different types of rock samples by applying UCS tests. A thermal camera was used to determine the potential failure patterns and as a result, three types of failure patterns were determined. These were

defined as “X”- formed, “//”- formed, and “|”- formed. Experiments in the marble sample showed that the temperature concentration was “X”- formed (Figure 2.26). In Figures 2.27 and 2.28, as a result of the experiments carried out on granite samples, it was observed that the temperature concentration was “//” and “|”- formed.

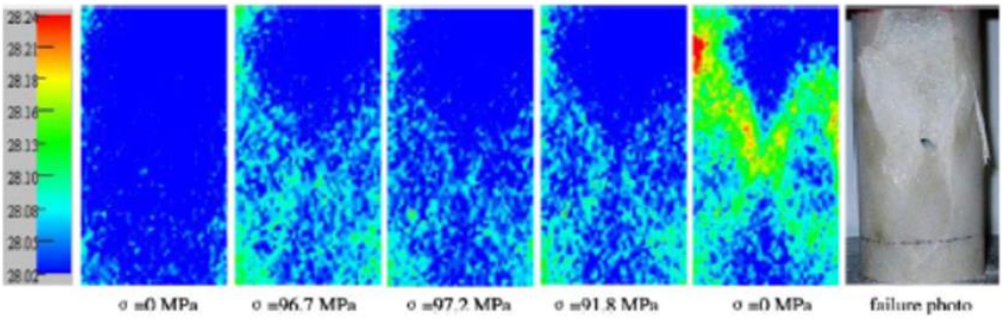

Figure 2.26. Marble specimen showing “X”- formed failure as a result of the uniaxial compression test (Wu et al.,2005)

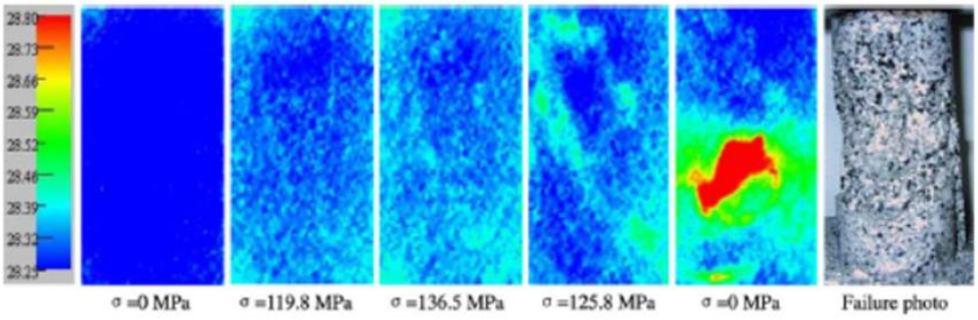

Figure 2.27. Granite specimen showing “//”- formed failure as a result of the uniaxial compression test (Wu et al.,2005)

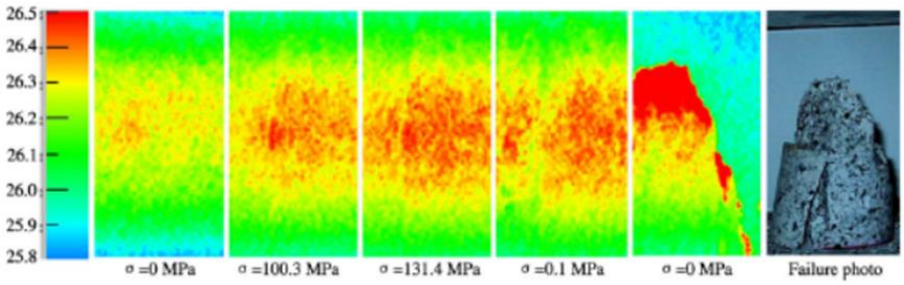

Figure 2.28. Granite specimen showing "|"- formed failure as a result of the uniaxial compression test (Wu et al.,2005)

As it can be seen from Figure 2.26, 2.27, and 2.28, there is a direct relationship between the temperature concentration regions and the failure plane of the rock. Therefore, thermal cameras were stated as an effective method for the determination of the failure behavior.

Thermal cameras are also used to detect the initial crack formation during static deformation and other rock mechanics related tests of rock samples. This behavior is provided by monitoring the heat transfer that occurs due to shear on the failure surface. Pappalardo et al. (2016) examined the cooling rate indices associated with the crack conditions of rock masses by using a thermal imager under different climatic conditions. The relationship between the measurable crack development and the thermal behavior of the rock masses was evaluated. The representative thermal camera image shown in Figure 2.29 shows that the temperature values of the different filling materials within the discontinuity may also be different.

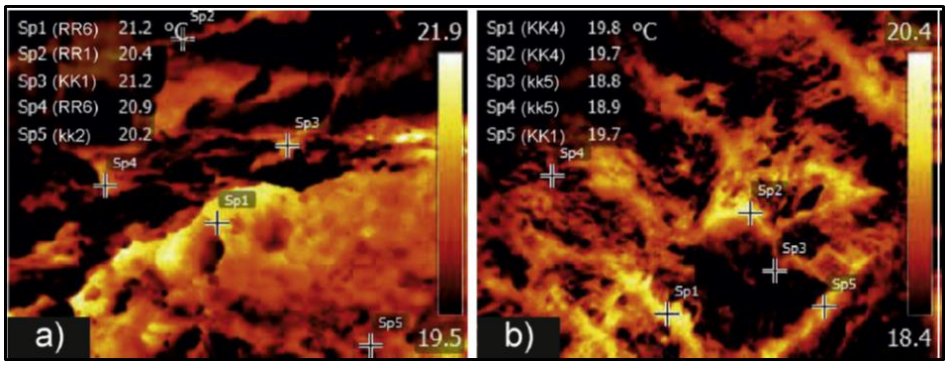

Figure 2.29. The temperature readings of different filling materials in the discontinuity (Pappalardo et al., 2016)

The existence of a relationship between thermal behavior and volumetric joint number was determined by using regression methods. It has been concluded that the use of IR thermal cameras should be investigated in more detail for the remote detection of cracks and different discontinuities.

Salami et al. (2017) stated that real-time IR thermography methods could monitor the energy generated by the breaking of particles in rock samples and especially friction. As shown in Figure 2.30, the change in the tensile strength caused due to the thermo-elastic effect was monitored by thermographic images. It is seen especially at the contact points before and after the experiment.

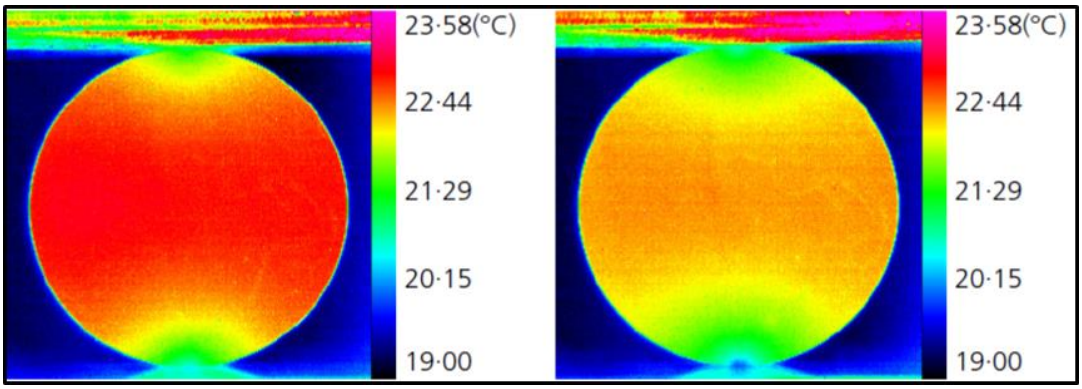

Figure 2.30. Temperature concentration at the contact points before and after the experiment (Salami et al., 2017)

A high-speed IR thermal camera was used to measure the amount of the heat generated at the crack end of experiments, especially for the determination of crack. A sudden temperature change was observed in the rock samples. It was concluded that the measured maximum temperature value depends on the rock type.

Tan et al. (2007) examined the distribution of heat exchange on granite samples, by drilling holes with a diameter of 1 cm in the center of the specimens (Figure 2.31). Considering that the temperature values to be measured from the sample may vary depending on the sample size, different sizes of samples had to be examined.

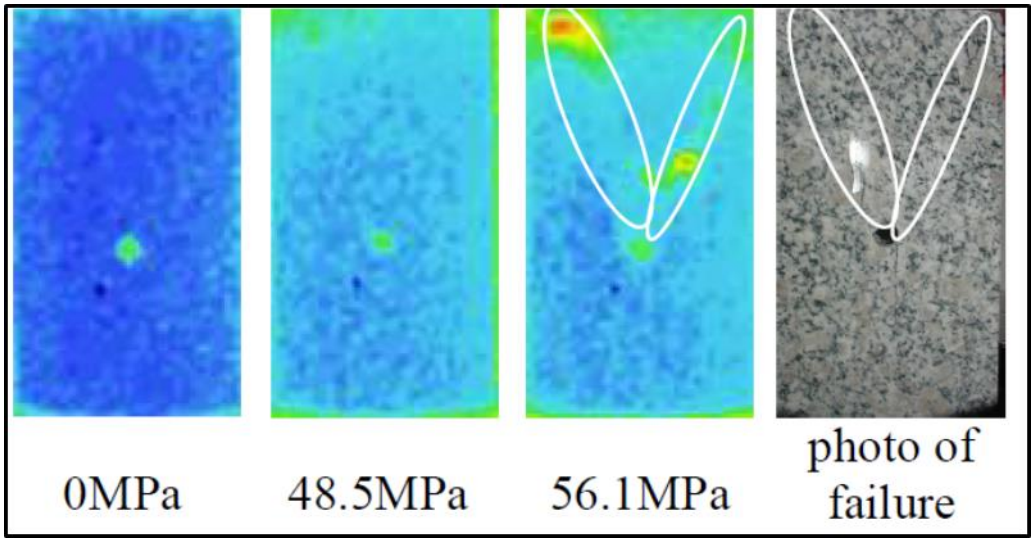

Figure 2.31. Temperature changes observed during crack formation (Tan et al., 2007)

As a result, high-temperature values were recorded on the surface of the failure region during the formation of measurable cracks. It was observed that the temperature values measured before the crack formation increased and decreased during the loading, and immediately before the crack formation, consequently increased suddenly at the failure moment. However, it is predicted that this behavior can vary even during experiments using samples prepared for the same rock type. For this reason, it is of great importance that different types of the rock should be monitored by using IR thermal cameras.

Wang et al. (2016) aimed to predict the points that limestone sample would fail during the UCS tests by using a thermal camera. It was concluded that there might be a significant relationship between the change in the stress values recorded during deformation and failure, and the temperature values monitored by a thermal imager. As shown in Figure 2.32, different temperature profiles were obtained during the UCS tests.

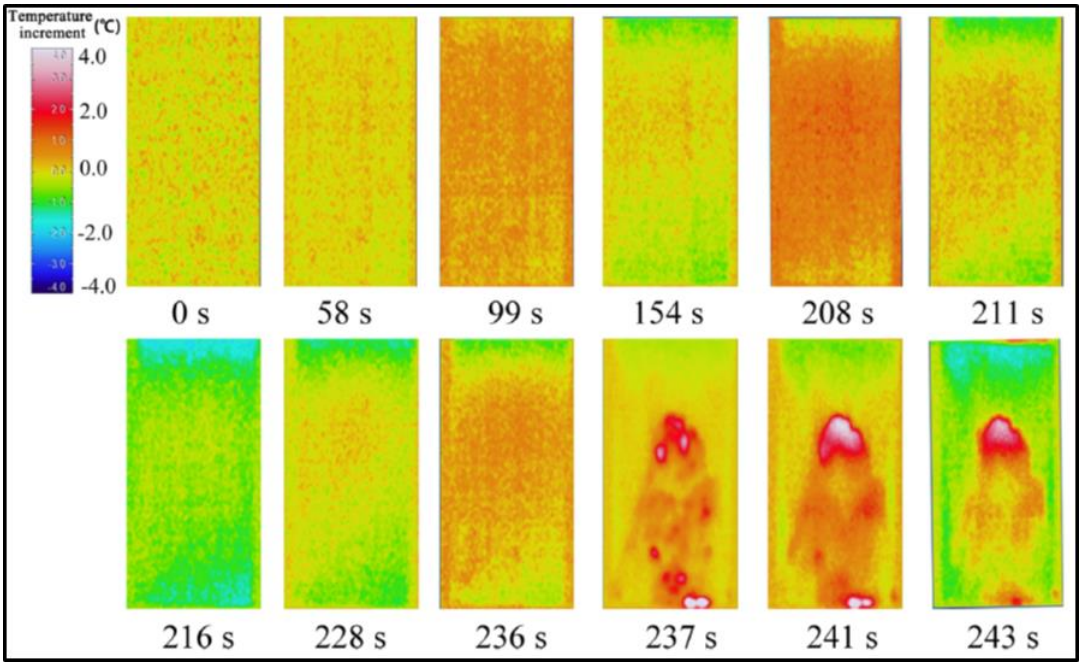

Figure 2.32. Time- spatial formation of different thermograms (Wang et al., 2016)

In particular, the point at which the measured average temperature value starts to decrease after the sudden rise can be used as the predicting point where the failure will begin. Therefore, it is thought that the relationship between stress and temperature values recorded by using IR thermal camera for different loading speeds and different rock types should be examined in more detail.

Mineo and Pappalardo (2016) proposed a new method for the determination of the porosity of rock samples by using an IR thermal imager. An innovative approach has been described for calculating the porosity value of rock samples, which are known to affect the mechanical behavior of rocks, using cooling behavior in the laboratory environment. As shown in Figure 2.33, rock samples with different porosity values were recorded with the help of the IR thermal camera.

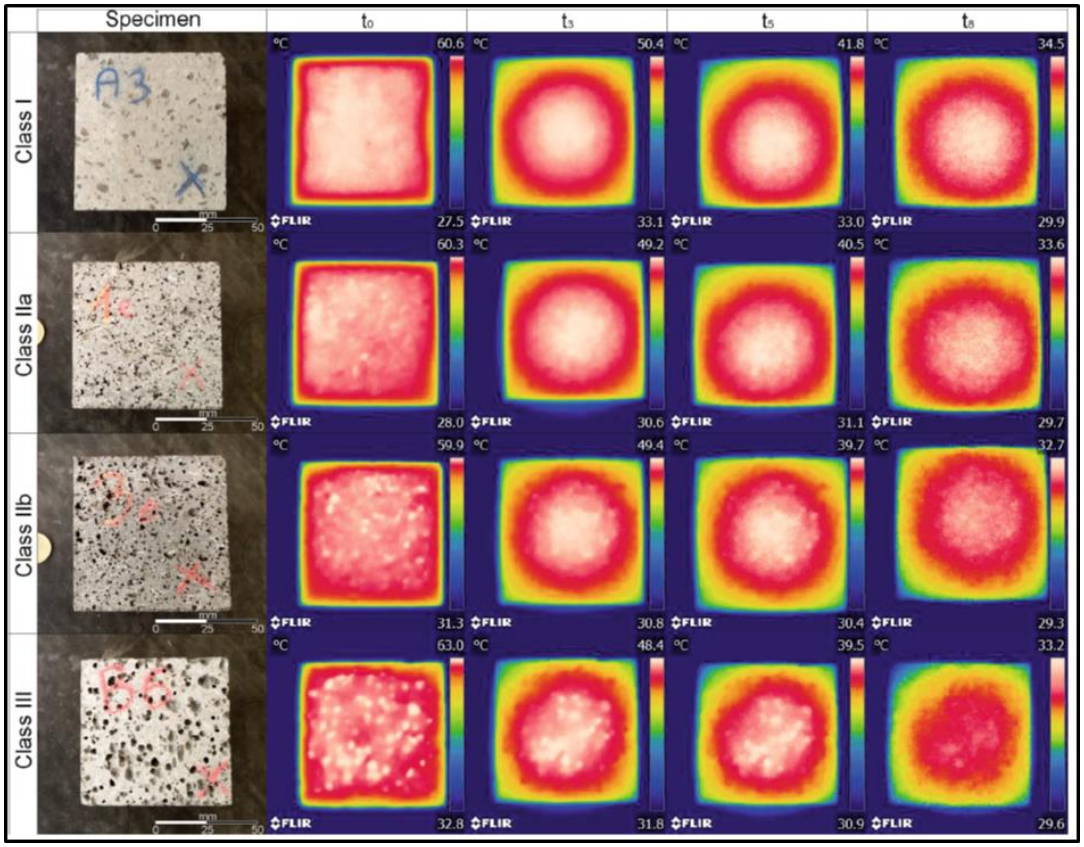

Figure 2.33. IR thermal images of rock samples with different porosity values (Mineo & Pappalardo, 2016)

As a result of their experiments, more temperature decrease was detected depending upon the porosity rate of the specimens. Hence, they show that temperature decrease can be seen instead of a sudden temperature increase at the failure moment by considering the rock type. This temperature decrease amount is directly related to the porosity rate of the sample.

In addition to rock mechanics experiments in the laboratory environment, some researchers modeled the physical environment of the mining area to be examined at laboratory scale. Afterwards, these researchers carried out experiments on these physical environments and monitored the results of the experiments with the help of the thermal camera.

Gong et al. (2012) modeled the construction of a road in a multi-layer coal mine with a 60° slope and tried to determine the damage on the tunnel walls according to the change in the temperature. The rock layer was modeled as coal in the layer where excavation would take place. For lower and upper layers, sandstone and claystone were taken as rock layers, respectively.

The results of the study were compared with the results of the previous studies in the literature, which are about inclined layers with a slope of 0°, 45°, and 90°. The excavation of the road was performed manually with a hammer and a chisel. It continued from the back surface of the model to the front surface. With the thermal camera in front of the model, it was aimed to understand the temperature changes and the damage that these changes can cause. According to the results of this research, the temperature change in the 0° slope layer was distributed differently and heterogeneously all over the model. In the 45° slope layer, the temperature changes were weak in a specific region. In the 60° and 90° slope layers, the temperature changes were also concentrated in a specific region, and their intensity was relatively higher (Figure 2.34).

As a result, the model representing the slope layers 60° and 90° were identified as having a high probability of significant damage. Therefore, it is stated that precautions should be taken especially for these cases.

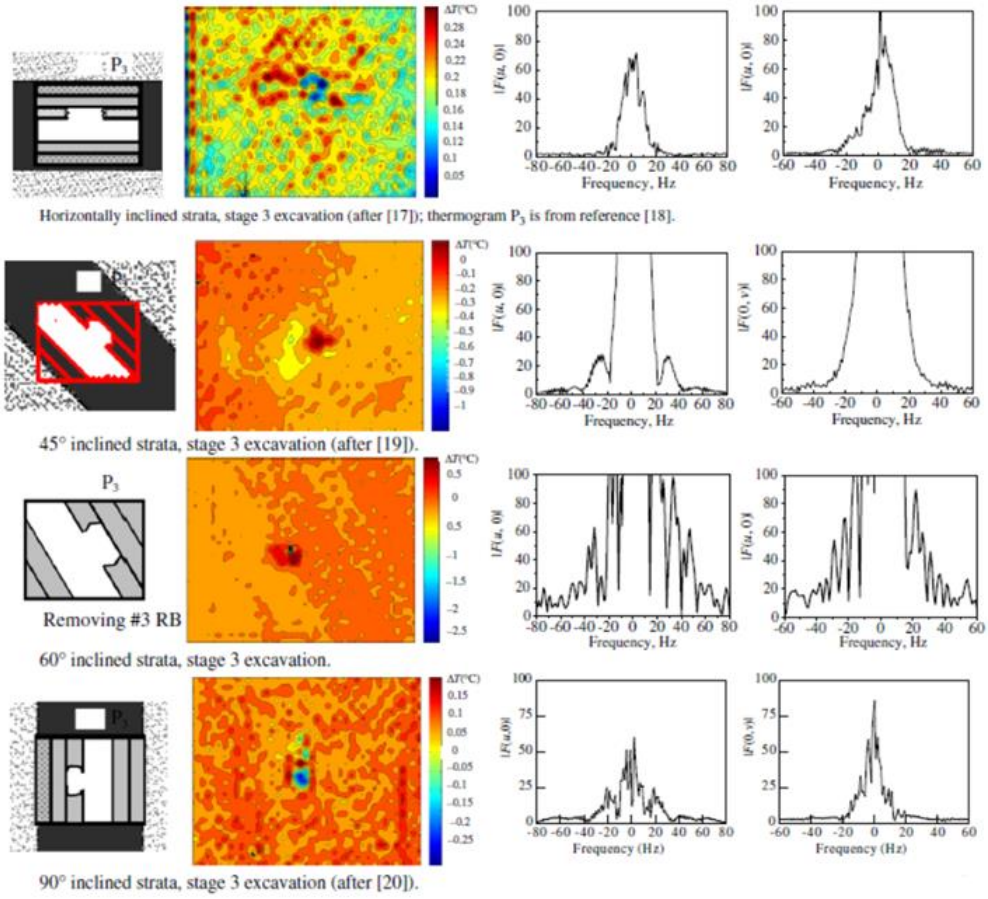

Figure 2.34. Investigation of the temperature change resulting from the road excavated in the slopes of 0°,45°,60° and 90° (Gong et al., 2012)

Gong et al. (2015) investigated the stress distribution and the possible failure behavior around a planned tunnel. This tunnel is located in the Xuzhou mining region of China and was planned to be opened from a depth of 300 meters to 1000 meters. The mine strata were modeled in nine layers, and the coal seam was placed in the fourth layer. After modeling the strata of the mine, stress levels were changed vertically and horizontally. The behavior around the tunnel was investigated according to temperature changes by the thermal camera. First, hydrostatic stress, horizontal and vertical stresses were increased up to 0.8 MPa. As a result of this, small deformations were observed and the stresses were increased to 1.4 MPa by increasing both the horizontal and vertical stresses. In this stress level, failure regions became visible on

the side surfaces. Based on the thermal camera recordings, the regions in dark red color represent the failure region (Figure 2.35).

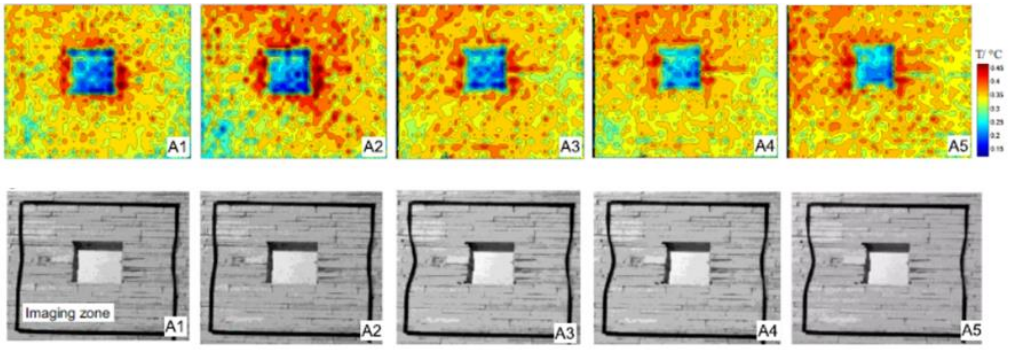

Figure 2.35. Thermal camera images taken at that moment; stress conditions (MPa); A1(0.8,0.8), A2(0.8,0.8), A3(0.8,0.8), A4(1.4,1.4), A5(1.4,1.4) (Gong et al.., 2015)

Afterward, the horizontal stress was kept constant at 1.4 MPa, and the vertical stress was increased to 2.5 MPa and 6 MPa, respectively. After this stress level, it was seen that the dark red colors started to get concentrated on the corners and the side surfaces of the tunnel boundary. There was also floor heave on the ground. Therefore, the red color was more intense in this region by considering the thermal image. Due to these behaviors, possible failure was expected in these regions. Figure 2.36 shows the thermal response of the tunnel as a result of the increase of vertical stress. It has been observed that the red color darkens where the stress is concentrated.

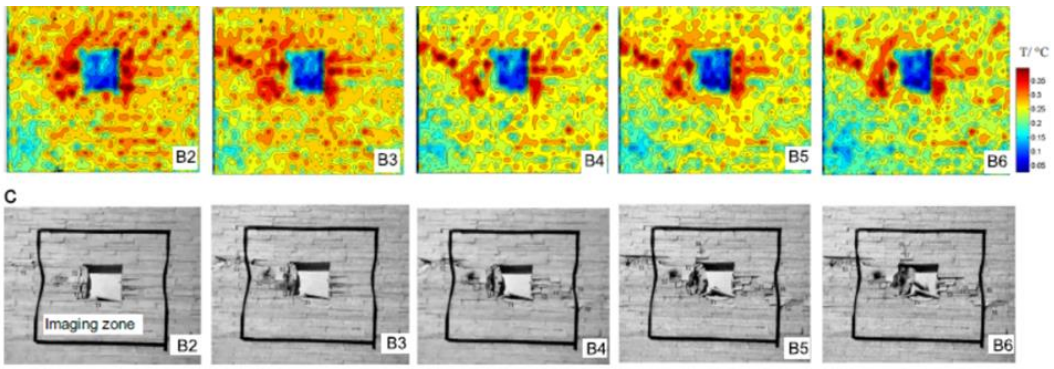

Figure 2.36. Thermal camera images taken at that moment; stress conditions (MPa); B2(2.5,1.4), B3(3,1.4), B4(4,1.4), B5(5,1.4), B6(6,1.4) (Gong et al., 2015)

As a result, it is concluded that the thermal camera can be used as an equipment for the determination of the stress concentration and possible failure zones.

Rockburst is a problem that can be seen at deep mines. According to Kaiser et al. (1996) and Hedley (1992), rockburst is defined as the sudden release of the high amount of energy held by the rock towards the excavated free surface. Sun et al. (2017) examined the use of thermal cameras in detecting rockburst conditions. Tuff sandstone samples were used and modified true-triaxial apparatus, which is developed for the detection of the rockburst used in the experiments. Data were recorded with the thermal camera placed in front of the model to analyze the thermal behavior.

Modeling was performed to represent a tunnel project in China with 720 meters of depth. Vertical stress was applied as 16.2 MPa, and horizontal stresses as 15.1 MPa and 11.1 MPa, respectively. The samples were kept under these stresses for 20 minutes. Then the 11.1 MPa horizontal stress was removed, and the vertical stress was increased suddenly. The removal of the horizontal stress represents the tunneling activity, and the increase of the vertical stress represents the stress concentration after the tunnel is opened.

As a result of the experiments, the rockburst phenomena was divided into four different phases. Phase 1 is called silent period. During the silent phase, the energy was collected in the specific regions of the sample. The thermal camera determined temperature changes in these areas. In regions where energy is collected, the temperature increases from 20.8 ℃ to 22.6 ℃. Figure 2.37 shows the temperature increase in the first phase.

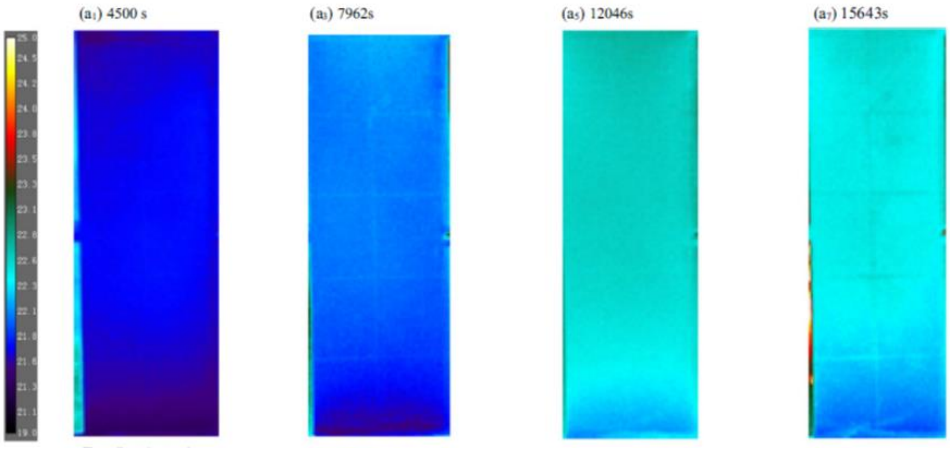

Figure 2.37. Time-dependent development of the silent period (Sun et al., 2017)

Figure 2.38 shows the second phase, which is called the crack propagation phase. In this phase, the formation and expansion of the cracks were seen with the thermal camera. The temperature increase was observed in the fractured areas.

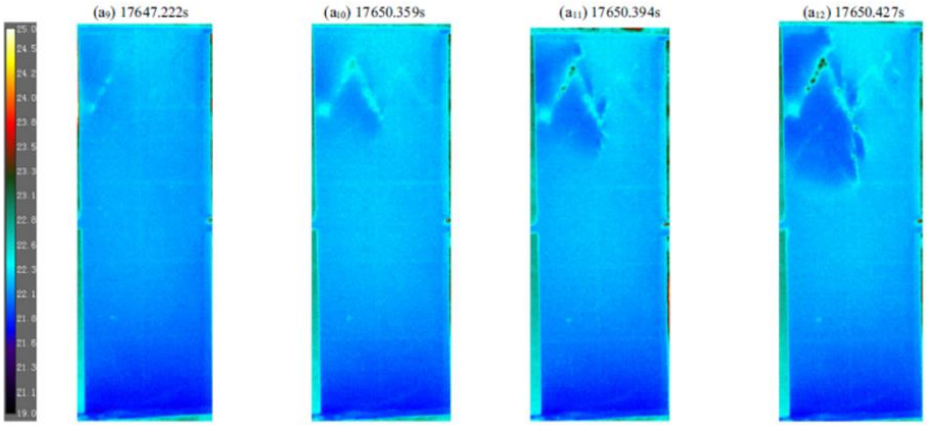

Figure 2.38. Time-dependent development of the crack propagation phase (Sun et al., 2017)

The third phase is called the particle removal phase. In this phase, the cracks were enlarged, and the small particles burst out from the specific regions. Figure 2.39 shows the particle removal phase.

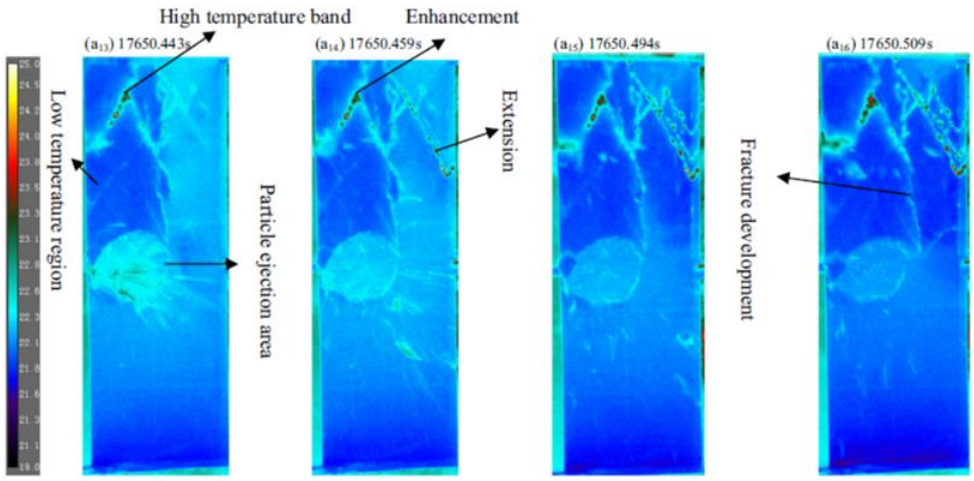

Figure 2.39. Time-dependent development of the particle removal phase (Sun et al., 2017)

The last phase is called the rock eruption phase. At this stage, a sudden increase in the temperature was observed in specific regions of the sample. It was also observed that the particles were poured in the form of flaking. The sudden increase at the temperature, which is from 22.3 to 23°C, explains the transition from the elastic phase to the plastic phase.

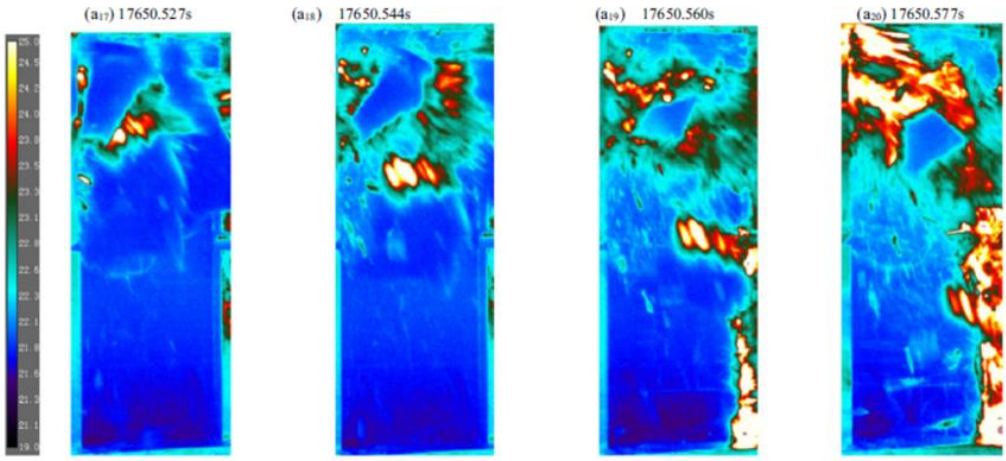

Figure 2.40. Time-dependent development of the rock eruption phase (Sun et al., 2017)

They concluded their study as the temperature increased linearly with the increasing stress in the elastic stage. However, they detected that the temperature is rapidly increased in the plastic stage. This phenomenon is an important precursor before

rockburst occurred. As a result, it was concluded that the thermal camera is an essential equipment for rockburst detection.

Sun et al. (2018), in another study, investigated the deformation of a tunnel to be excavated in a deep rock layer. They examined the relationship between deformation and temperature change around the tunnel during the excavation. Modeling was carried out in Xin'an Coal Mine in Gansu, China. Tunnel excavations at a depth of 730 m were modeled. Triaxial compression tests were carried out for the modeling studies, and the predetermined stresses were applied on the model. The excavation modeling of the tunnel was also represented by excavating inward stages. In this context, the tunnel was divided into eight separate layers at a depth of 50 mm, and each layer was examined separately. Figure 2.41 shows these stages.

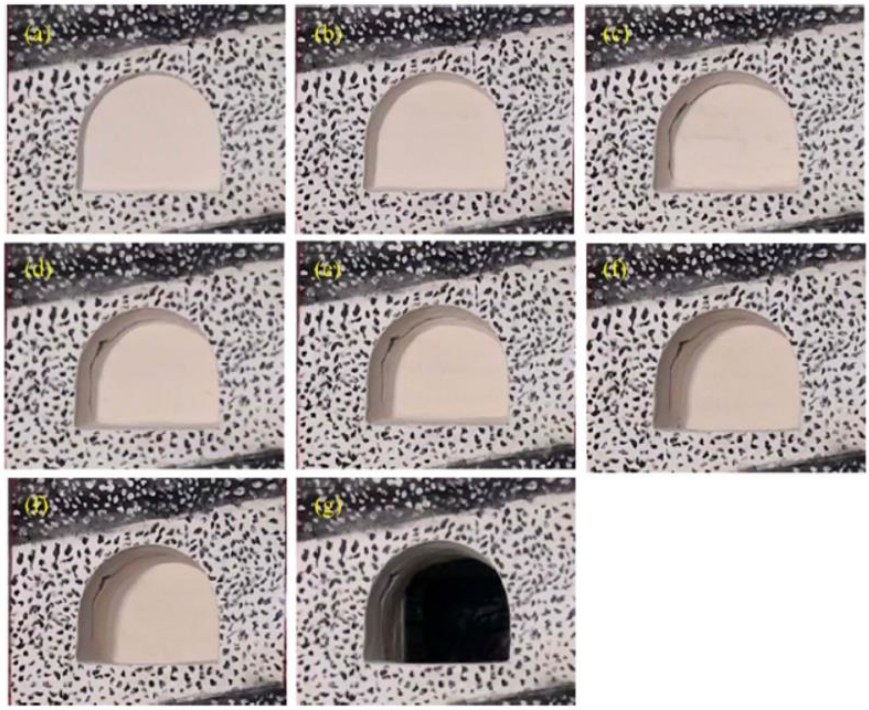

Figure 2.41. Eight stages of the excavation (Sun et al., 2018)

As a result of their experiment, the thermal imager did not show a significant increase in temperature from the first stage to the sixth stage. After step six, the increase in the temperature was monitored until the eighth stage. This increase in temperature was observed in the areas where friction was in action. There was also a temperature decrease, which is observed in the micro fractures. Figures 2.42, 2.43 and 2.44 show the temperature change behavior of stages 1, 6 and 8, respectively.

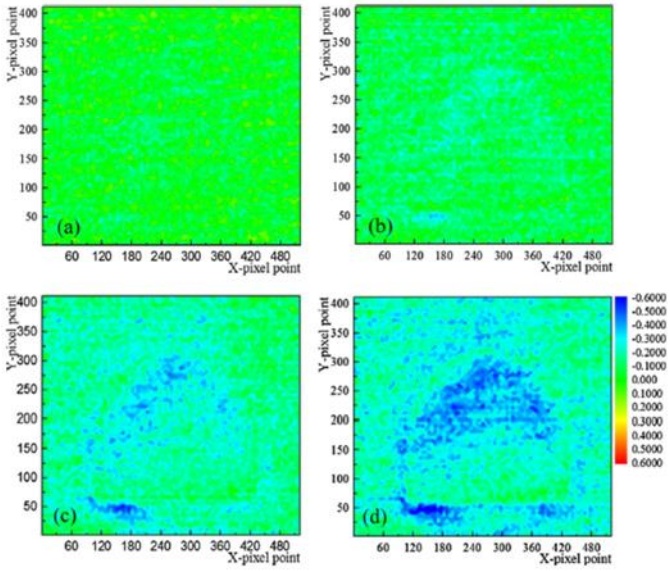

Figure 2.42. Temperature change in the first stage (Sun et al., 2018)

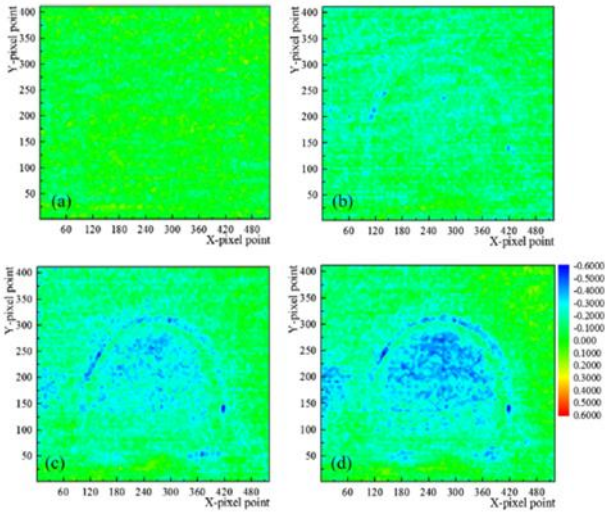

Figure 2.43. Temperature change in the sixth stage (Sun et al., 2018)

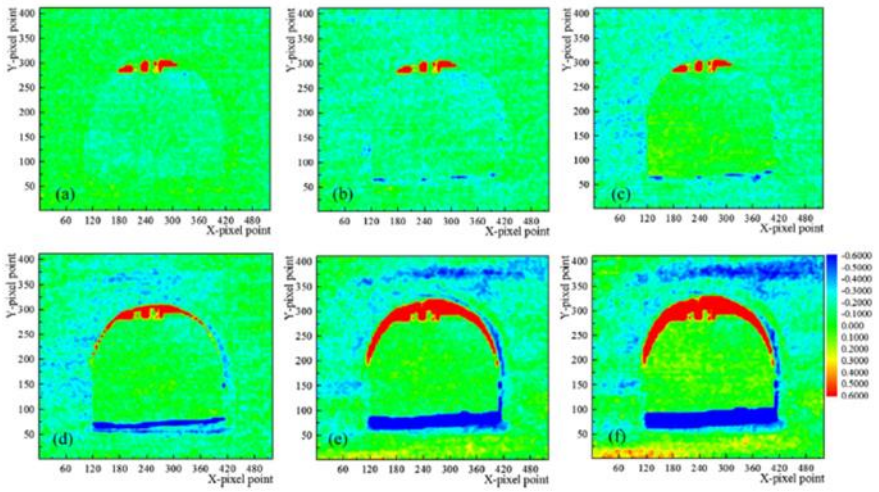

Figure 2.44. Temperature change in the last stage (Sun et al., 2018)

Hence, it was observed that the temperature changes were directly related to the behavior of the rock surrounding the tunnel. The causes of the temperature decrease were determined as the stress drop and the formation of the micro cracks. It was mentioned that the temperature increase caused by friction during the excavation.

Sun et al. (2017), in another study, modeled a tunnel planned to be opened in a deep rock formation with 10° of inclination. They tried to examine the effect of the stress on the sidewalls and swell of the ground. Modeling is based on the Xuzhou Coal Mine in China. The evaluation was made with a thermal camera according to the regions where the temperature is concentrated. The experiments were carried out in three different stages, and these stages were named A, B, and C. In stage A, the horizontal and the vertical stress were increased incrementally from 0 to 2.5 MPa. This stress level was kept constant in both directions for stage B. In stage C, the vertical stress was kept constant at 2.5 MPa, and the horizontal stress was gradually increased up to 4.5 MPa. As a result of this, stage C was examined with the thermal camera, and inferences were made. This gradual stress change was divided into four stages from 2.5 MPa to 4.5 MPa, which are named C1, C2, C3, and C4. Figures 2.45, 2.46, 2.47 and 2.48 represent the thermal imaging of these stages, respectively.

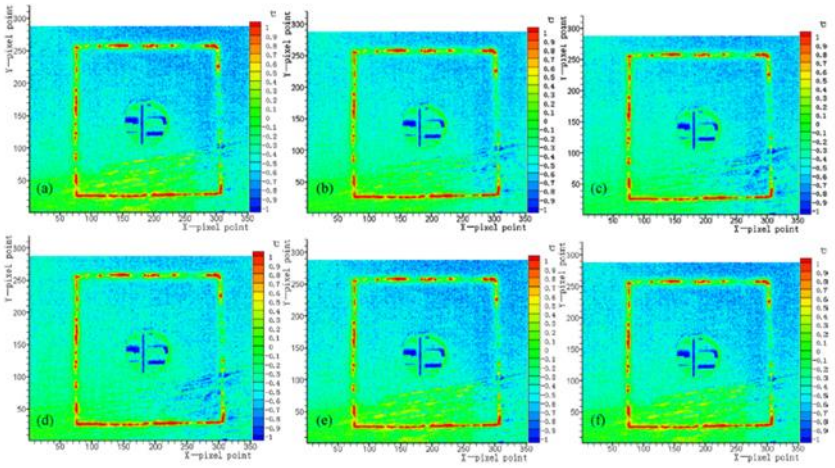

Figure 2.45. Temperature change during stage C1 (Sun et al., 2017)

In stage C1, a small amount of the temperature increase was observed on the roof and the sidewalls, while the temperature on the floor sometimes decreased and sometimes increased. The temperature change was determined between 0.5 ℃ and 0.8 ℃.

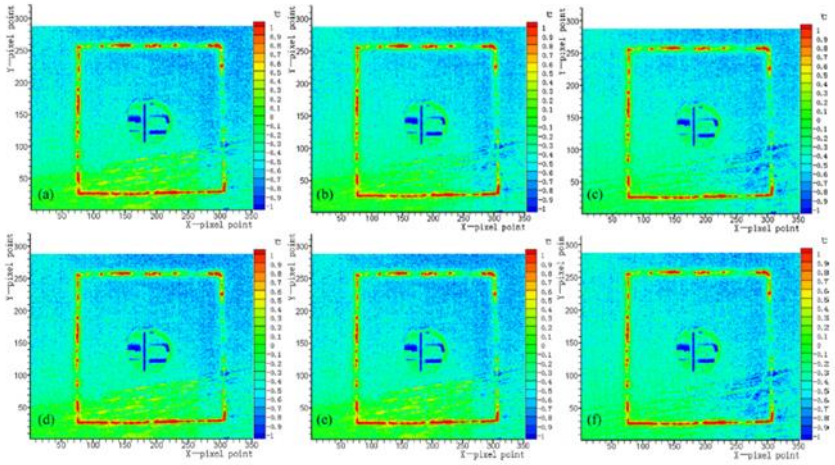

Figure 2.46. Temperature change during stage C2 (Sun et al., 2017)

Stage C2 has almost the same characteristics as C1. The temperature change is between 0.6 ℃ and 0.9 ℃.

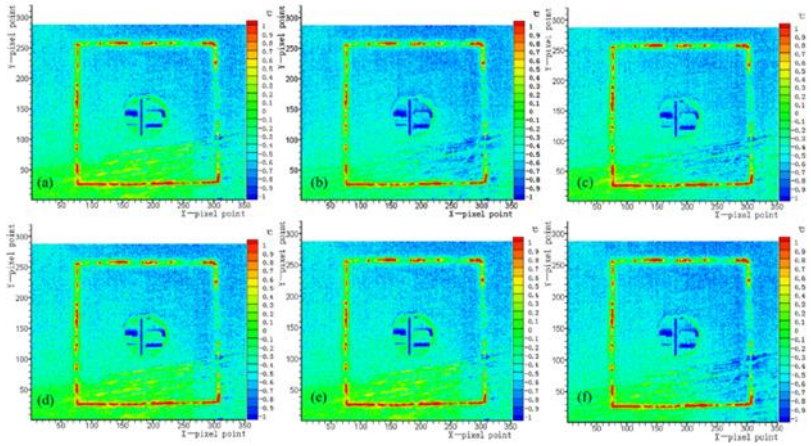

Figure 2.47. Temperature change during stage C3 (Sun et al., 2017)

In C3 stage, it was seen that the temperature change regions on the floor were considerable.

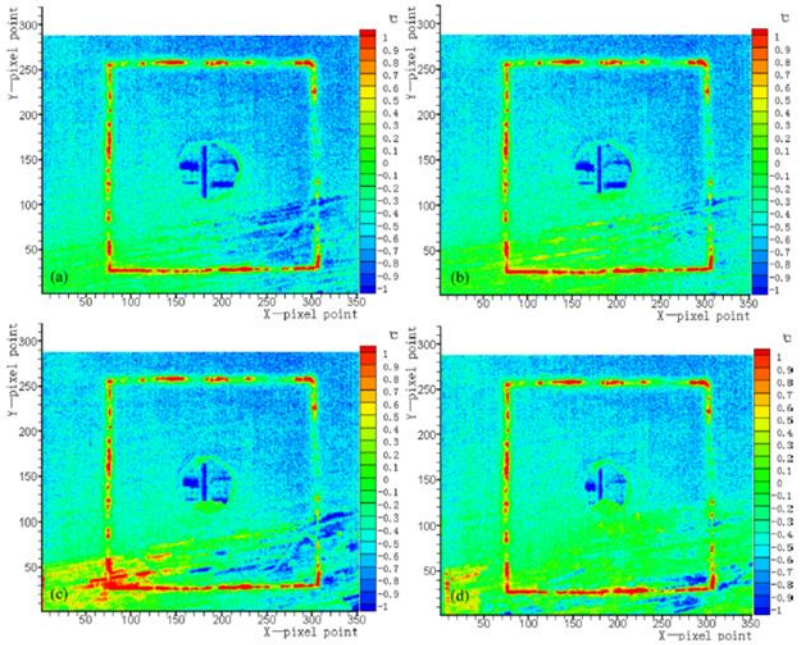

Figure 2.48. Temperature change during stage C4 (Sun et al., 2017)

Finally, C4 stage showed almost the same characteristics as C3 stage. However, the situation examined in the C4 stage is more clearly observed. It was also stated that the friction caused by the stress increases the temperature while the new formed micro

cracks decrease the temperature. This behavior is the reason for the temperature increase and decrease in some regions. As a result, the temperature change range was measured between 0.5 ℃ and 0.9 ℃.

The literature survey conducted within the scope of this thesis study indicated that researchers performed their experimental studies on different types of rock samples utilizing thermal imaging devices. The experiments carried out in this thesis study are UCS, static deformability and indirect tensile strength tests in a displacement-controlled environment. As a result of the experiments, the initial crack formation, temperature change at the moment of failure, and energy losses of samples after failure were investigated. For samples which are taken from the rock blocks, relationship between the porosity rates and energy dissipation were analyzed. Porosity rate can affect the structure of the rock (McWilliams,1966; Engelder and Plumb, 1984; Fitzner, 1994; Winkler, 1997; Almeida et al., 1998). Since porosity can affect the failure behavior of the rock sample, it plays an essential role for characterization of rocks (Dunn et al.,1973; Dearman et al., 1978; Tuğrul and Gürpınar, 1997, Palchik and Hatzor, 2004; Sousa et al., 2005; Baud et al., 2014; Di Benedetto et al., 2015). Analysis of the relationship between porosity rate and energy dissipation of the specimens can be found in Chapter 4.

CHAPTER 3

LABORATORY STUDIES

Laboratory studies cover rock mechanics laboratory tests including indirect tensile(Brazilian), static deformability tests, and uniaxial compressive strength tests. Andesite, marble, gneiss- schist and claystone samples were used at experiments. First of all, indirect tensile (Brazilian) tests were conducted on the andesite samples. The crack initiation points and crack coalescence of the sample were tried to be followed with the help of a thermal camera. The indirect tensile strength values of the andesite samples were obtained by these tests. These experiments were followed by static deformability tests. These tests were carried on the andesite and claystone samples. From these tests, rock properties, Elastic Modulus (E) and Poisson Ratio (ν) were obtained. The experiments were also recorded by the thermal camera. Finally, UCS tests on the andesite, marble and gneiss- schist specimens were carried out to obtain the uniaxial compressive strength of the materials. All tests were carried out according to the International Society of Rock Mechanics (ISRM) suggested methods.

3.1. Testing Equipment Utilized in the Experimental Study

In order to obtain the rock parameters, which are E, ν, σ_t, UCS, rock mechanics tests are required. Since these values had an essential effect on the modelling, laboratory work should be carried out very carefully. It is known that rock properties can affect the experiment results. At this point, detection of the failure region requires more attention. In this study, experiments were followed by thermal camera to detect the failure regions on the sample. Table 3.1 summarizes the performed rock mechanics experiments within the scope of this thesis study.

Table 3.1. *General information about the experiments*

Rock Type	**Experiment**	**Diameter(mm)**	**Number of Experiment**
Claystone-Conglomerate	Static Deformability Test	63	6
Andesite	Brazilian Test	75	3
Andesite	UCS Test	75	5
		63	14
		53	5
		42	5
Marble	UCS Test	75	5
		63	9
		53	5
		42	5
Gneiss-Schist	UCS Test	63	25

3.1.1. Testing Machine

Different loading cycles were defined in the MTS 815 testing device which is a displacement-controlled environment with a maximum loading capacity of up to 500 kN as seen in Figure 3.1. This testing machine consists of a highly stiff load frame, fixed crossheads and single-ended actuators. These parts make the experiments suitable for the post-failure behavior. The test procedure was based on the suggested methods of the ISRM standards (Ulusay & Hudson, 2007). The samples used in the

experiments were prepared as having a height/ diameter ratio of 2.5-3 for UCS and static deformability tests. According to these values, samples were taken from the rock block with the help of a rock coring machine. Later, both surfaces of the samples were flattened to apply the same load symmetrically. As a result of the experiments, the force and displacement values recorded by the MTS 815 testing environment were evaluated. The results were obtained with the help of LVDT and differential pressure transducer by transferring the data to the FlexTest 40 data acquisition system. The moment of the failure could be specified from the sudden drop in the force-time graph, and the stress-strain graph.

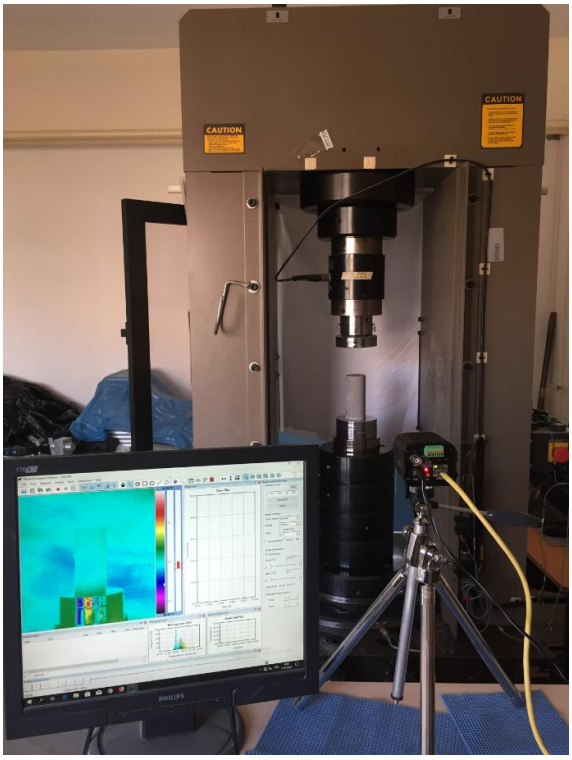

Figure 3.1. MTS 851 test system

3.1.2. Thermal Camera

Experiment results were recorded by a thermal camera as seen in Figure 3.2, manufactured by COX. The camera is an uncooled long-wavelength infrared thermal camera.

Figure 3.2. COX, thermal camera

There is also a software of the thermal camera that is used to analyze the results. This software enables the user to divide the displayed area by the pixel dimensions of the camera, giving the temperature value detected at each pixel. Geometric shapes such as square, rectangle, or circle can be defined from any desired region in the interface of the program to query the temperature readings. In this area, average, minimum, and maximum temperature values can be determined. The graphs of these values can also be obtained with the help of this software. An example of the interface of the software is shown in Figure 3.3.

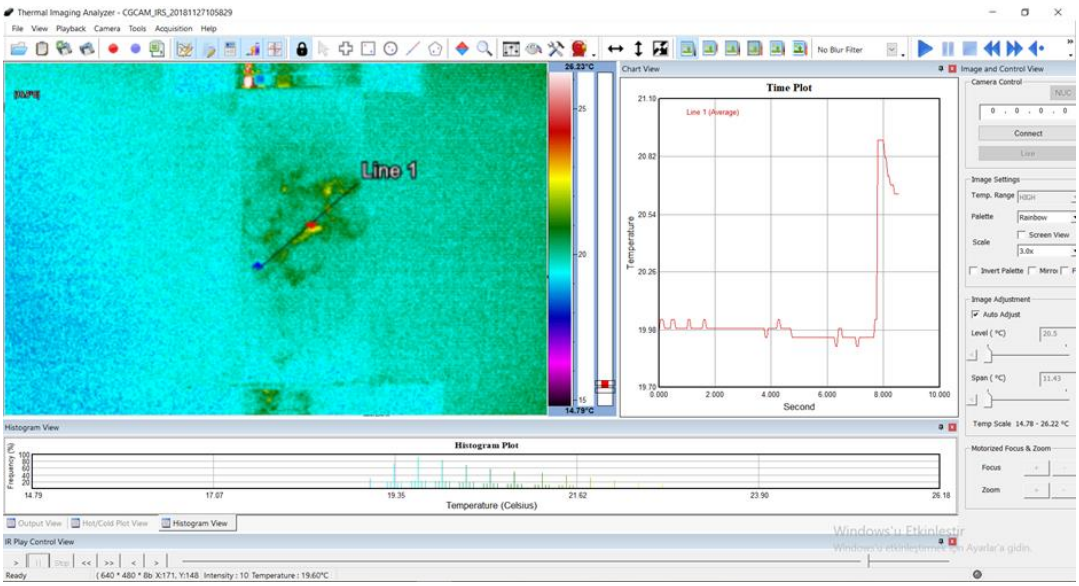

Figure 3.3. Interface of the Thermal Camera Software

Figure 3.4 shows the electromagnetic wave spectrum. As it can be seen, the wavelength range visible to the human eye is between 400 and 700 nanometers, whereas the infrared range is between 750 nanometers and 1-millimeter wavelength. That is why a naked eye cannot see the infrared rays. Thermal cameras can convert infrared ray to visible images. For this reason, using a thermal camera instead of the video camera in the analysis of the experimental results gives more detailed information about the behavior of the rock sample during the failure.

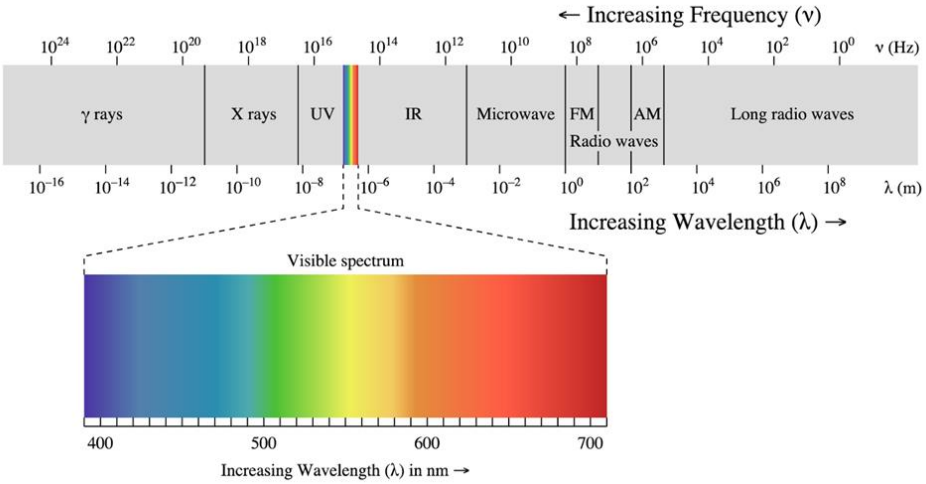

Figure 3.4. Electromagnetic wave spectrum (Retrieved from http://spmphysics.onlinetuition.com.my/2013/07/electromagnetic-waves-spectrum.html)

According to Fematek (2018), a long-wavelength thermal camera operates at 8-14 $x10^{-6}$ m, a medium-wavelength thermal camera at 3-5$x10^{-6}$ m, and a short-wavelength thermal camera operates at wavelengths up to 1.5 $x10^{-6}$ m. At room temperature, the wavelength emitted from the objects is at a maximum level of 10 $x10^{-6}$ m. At 300 ℃, the emitted wavelength is 5 $x10^{-6}$ m, while the emitted wavelength from the sun is 0.5 $x10^{-6}$ m. For these reasons, the ideal camera type for laboratory experiments has been identified as long-wavelength thermal camera.

The reason for choosing an uncooled thermal camera is that the cooling systems are more expensive and require continuous maintenance due to additional components.

Besides, cooling systems are often used for long-distance measurements. In the experiments carried out, there were no such requirements, so uncooled systems were preferred. The uncooled systems can be used with long-wavelength cameras, while the cooling systems can be used with medium and short-wavelength cameras.

Thermal cameras divide images into pixels based on their resolution, which improves the image quality in direct proportion to the number of pixels. The camera used in the experiments has a resolution of 640x480. It means that the thermal camera divides the image into 307,200 squares with 640 pixels from the left and 480 pixels from the top. In the middle of each square, the temperature values were recorded through the thermal camera software during the experiment. As mentioned before, any region can be selected through pixels after the following experiments in which temperature change occurs in this region. That is to say, as a result of the experiments, the failure regions in the samples can be determined, and the coordinates of this region can be obtained. These values are monitored from the beginning of the experiments until the end of the experiments. As a result, the temperature change in the failure zone can be followed.

By following the ISRM suggested methods, indirect tensile strength tests, static deformability tests and uniaxial compressive strength tests were performed. The experiments were monitored with a thermal camera. Tensile strength of andesite samples was obtained by Brazilian test. Young's Modulus and Poisson's ratio of claystone samples were obtained by static deformability tests. UCS value of the andesite, marble and gneiss- schist samples were obtained by UCS tests.

3.2. Indirect Tensile (Brazilian) Tests

The experimental studies of this thesis study were initiated with indirect tensile strength determination, Brazilian tests. The Brazilian discs were prepared at about 75 mm diameter and 43 mm thickness. The Brazilian discs were loaded a displacement rate of 0.002 mm/s. The initial objective of the research was to capture the initial crack formation and to determine the coalescence of the crack with the thermal camera.

However, it was seen that it was very difficult to capture this moment without a high-speed thermal camera since the formation and coalescence of the cracks events that occurred instantly. In order to capture the crack initiation moment, a high speed thermal camera is required. As a result of the experiments, tensile strength of the andesite samples was found as 11.80 MPa. Figure 3.5 shows an example of the Brazilian test, which was conducted and monitored with the thermal camera. Hence, Brazilian test for remaining samples were not conducted because of the lack of high speed thermal camera.

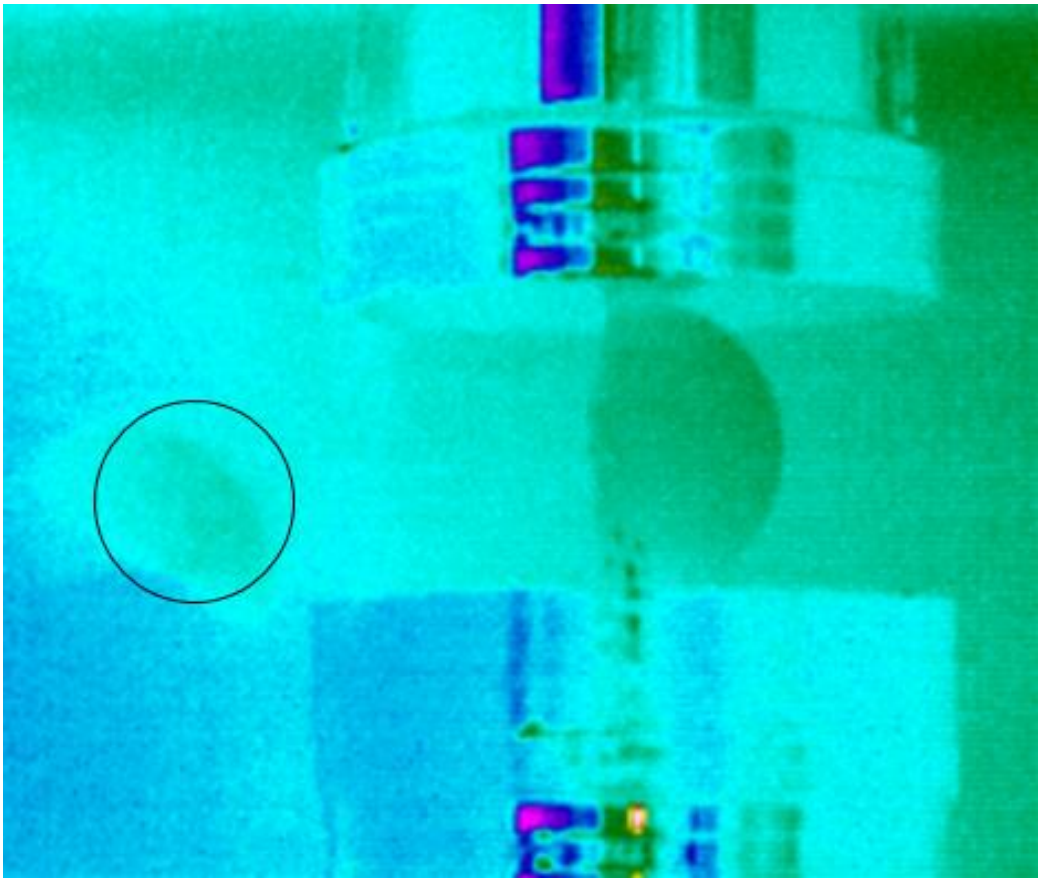

Figure 3.5. Thermal image of Brazilian test

As it can be seen from Figure 3.5, there was no distinct temperature change recorded during the tests and the moment of failure could not be captured as aimed. The specimen failed instantaneously and the left half of the specimen fell apart.

3.3. Static Deformability Tests

After the Brazilian tests, static deformability experiments were conducted on claystone samples to investigate the behavior of the rocks. However, during these experiments, it was seen that the extensometers used on the displacement-controlled setup to determine the Elastic Modulus and Poisson's ratios affect the temperature values measured by the thermal camera. This effect led to misleading results. Therefore, static deformability experiments could not be performed efficiently. Figure 3.6 shows the example of the static deformability experiment, which was conducted and monitored with a thermal camera. As a result of experiments, Elastic Modulus and Poisson's ratios values for claystone-conglomerate was obtained as 55.55 GPa and 0.19, respectively.

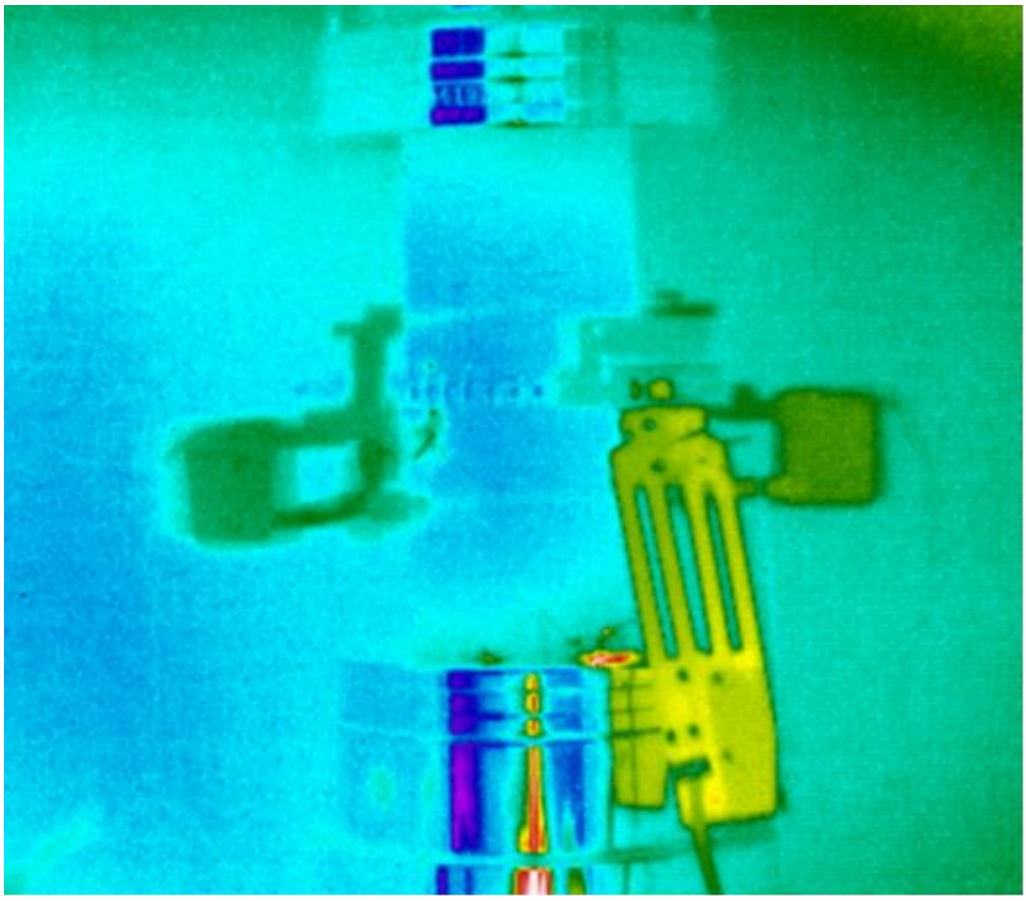

Figure 3.6. Thermal image of static deformability experiment

The circumferential extensometer used with the testing system had a considerably higher temperature during the experiments and blocked the visibility to a certain extent. Therefore, it was preferred to conduct UCS tests with the same setup.

3.4. Uniaxial Compressive Strength Tests

In UCS tests, the aim is to find the maximum amount of force that can be withstand by the rock specimen before failure. As a result of the UCS experiments, the results were obtained properly. This force value is evaluated by converting it to the strength value of the sample to define the rock mass and strength classifications. (Singh and Goel, 2012). Andesite, marble and gneiss-schist specimens were used for the UCS tests. Andesite and marble specimens were used with different diameter since they were prepared by taking cores from the rock blocks.

3.4.1. UCS Tests of Andesite Samples

According to the petrographic analysis of the andesite samples, the samples represent a fairly fresh, gray colored vesicular volcanic rock displaying aphanitic textures. Major phenocrysts of feldspar and hornblende are surrounded by a fine-grained groundmass. Hornblende crystals appear to be oxidized into Fe-Ti-oxides. Rock contains abundant but small-sized vesicles developed during magmatism, as well as sparse dissolution cavities formed by subsurface weathering and oxidation. Sample did not react with dilute HCl, suggesting absence of carbonate minerals. Attraction to magnetism is weak, which indicates presence of minor amounts of magnetite. The andesite specimens were prepared with four different diameters for UCS testing at a displacement rate of 0.002 mm/s. This loading rate was applied to the rock sample to analyze a proper experiment. For 75 mm, 53 mm, and 42 mm diameter size, five andesite specimens were examined. For 63 mm andesite specimens, more experiments were carried out since a comparison was made with greater number of available gneiss-schist specimens.

3.4.1.1. Andesite Specimens with 75 mm diameter

Five specimens with 75 mm diameter andesite were prepared for UCS tests. Figures 3.7 and 3.8 represent photos taken before and after the test of andesite specimens, respectively.

Figure 3.7. Andesite specimens with 75 mm diameter before test

Figure 3.8. Andesite specimens with 75 mm diameter after test

At the end of the experiments, 75A-1,75A-3, 75A-4 and 75A-5 specimens showed a temperature increase trend at the failure moment.

3.4.1.2. Andesite specimens with 63 mm diameter

14 andesite specimens of 63 mm diameter were prepared for UCS testing. Figures 3.9 and 3.10 provide the photos taken before and after the tests. The other test images of these specimens can be found in Appendix A.

Figure 3.9. Andesite specimens with 63 mm diameter before test

Figure 3.10. Andesite specimens with 63 mm diameter after test

At the end of experiments, 63A-1, 63A-2, 63A-4, 63A-5, 63AA-2, 63AA-4, 63AA-6 and 63AA-9 specimens were characterized with a sudden temperature increase during failure.

3.4.1.3. Andesite specimens with 53 mm diameter

Five andesite specimens with 53 mm diameter were prepared for the uniaxial compression test. Figures 3.11 and 3.12 represent the specimens before and after the test, respectively.

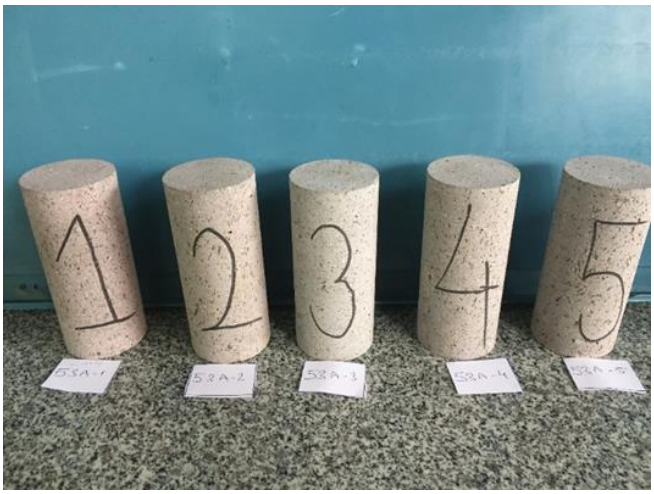

Figure 3.11. Andesite specimens with 53 mm diameter before test

Figure 3.12. Andesite specimens with 53 mm diameter after test

At the end of five experiments, 53A-1, 53A-4 and 53A-5 samples showed a sudden temperature increase during failure.

3.4.1.4. Andesite specimens with 42 mm diameter

Five andesite specimens with 42 mm diameter were prepared for the uniaxial compression test. Figures 3.13 and 3.14 show before and after the test of andesite specimens, respectively.

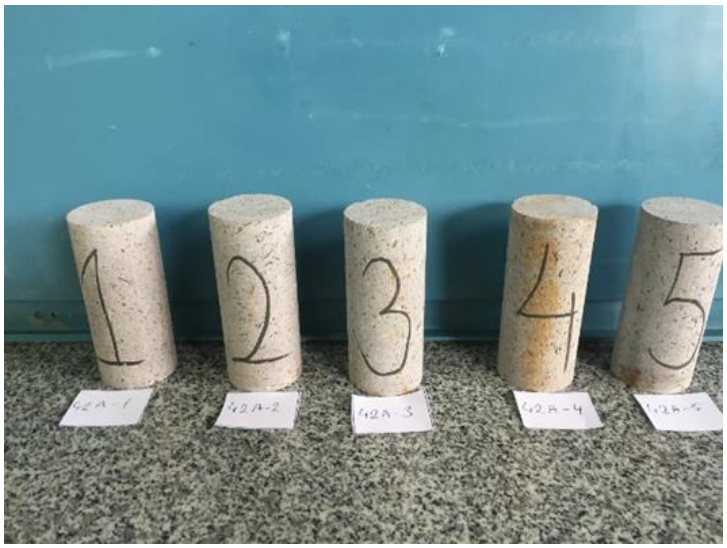

Figure 3.13. Andesite specimens with 42 mm diameter before test

Figure 3.14. Andesite specimens with 42 mm diameter after test

At the end of five experiments, 42A-2 and 42A-5 specimens showed a sudden temperature increase during failure.

3.4.2. UCS Tests of Marble Samples

As in the andesite samples, four different diameters of marble specimens were prepared for UCS tests at a displacement rate of 0.002 mm/s. This loading rate was applied to the rock sample to analyze a proper experiment. For 75 mm, 53 mm and 42 mm diameter size, five marble specimens were examined. For 63 mm marble specimens, more experiments were carried out since the results were compared with the greater number of available gneiss-schist specimens with this size. The experiments were conducted on marble specimens with 75 mm, 63 mm, 53 mm, and 42 mm diameter.

3.4.2.1. Marble specimens with 75 mm diameter

Five marble samples with 75 mm diameter were prepared for UCS tests. Figures 3.15 and 3.16 represent the marble samples before and after the tests. The specimens were named 75M-1, 75M-2, 75M-3, 75M-4, and 75M-5, respectively.

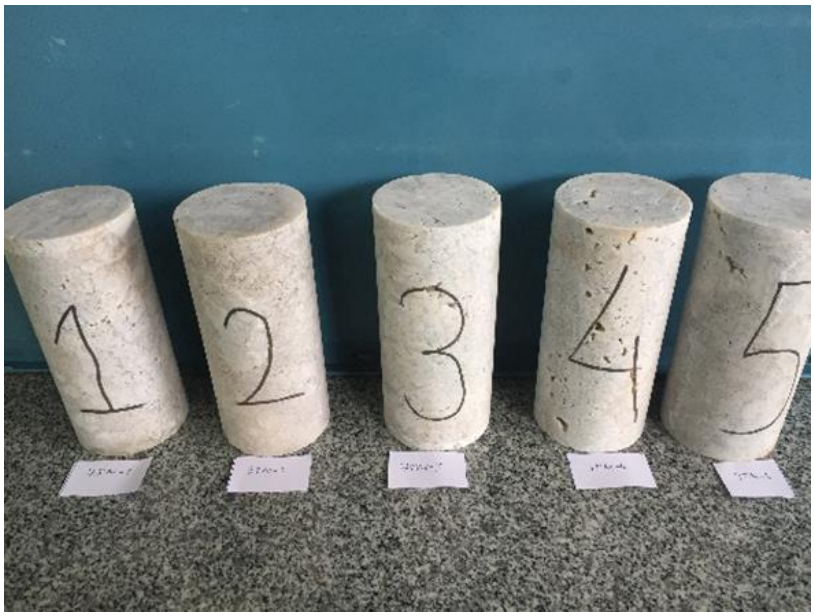

Figure 3.15. Marble specimens with 75 mm diameter after test

Figure 3.16. Marble specimens with 75 mm diameter after test

At the end of the five experiments, no considerable temperature change was measured at any surface.

3.4.2.2. Marble specimens with 63 mm diameter

Nine marble specimens with 63 mm diameter were prepared for UCS tests. The marble specimens before and after the test are represented in Figures 3.17 and 3.18, respectively. Other photos taken of these samples can be found in Appendix A.

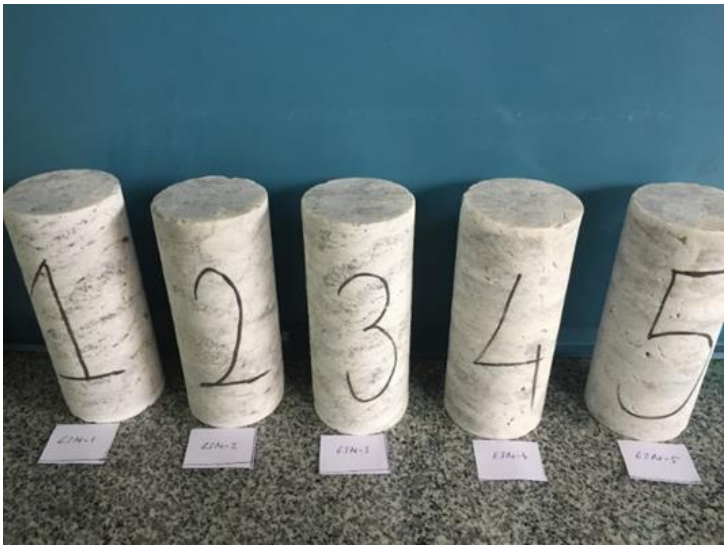

Figure 3.17. Marble specimens with 63 mm diameter before test

Figure 3.18. Marble specimens with 63 mm diameter after test

At the end of nine experiments, 63M-2, 63M-3 and 63M-4 specimens showed cooling behavior during experiments.

3.4.2.3. Marble specimens with 53 mm diameter

Five marble specimens with 53 mm diameter were prepared for UCS tests. Figures 3.19 and 3.20 represent the marble samples before and after the test.

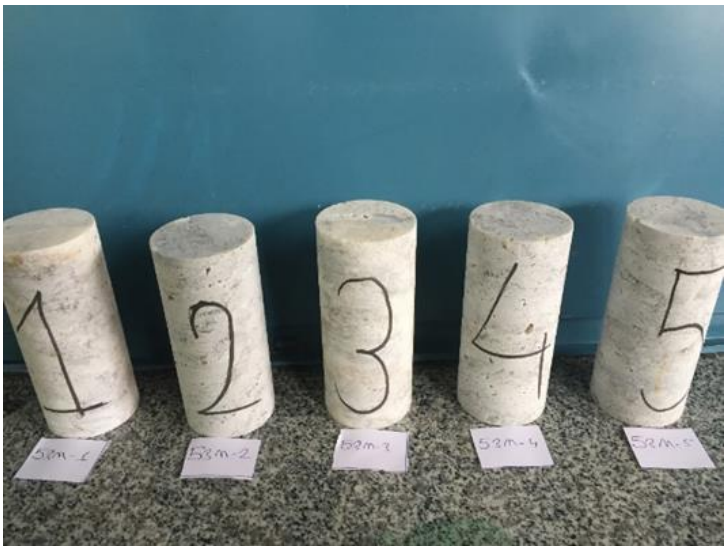

Figure 3.19. Marble samples with 53 mm diameter before test

Figure 3.20. Marble samples with 53 mm diameter after test

At the end of five experiments, 53M-1, 53M-2 and 53M-4 specimens showed cooling behavior during experiments.

3.4.2.4. Marble specimens with 42 mm diameter

Five marble specimens with 42 mm diameter were prepared for UCS tests. Figures 3.21 and 3.22 represent the samples before and after the test, respectively.

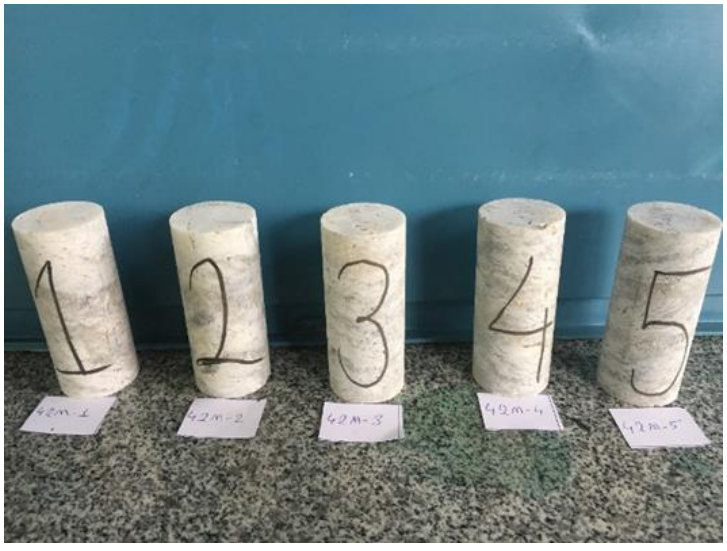

Figure 3.21. Marble specimens with 42 mm diameter before test

Figure 3.22. Marble specimens with 42 mm diameter after test

At the end of five experiments, 42M-2, 42M-3 and 42M-4 specimens showed cooling behavior during experiments.

3.4.3. UCS Tests of Gneiss-Schist Samples

Gneiss-Schist samples were prepared by using the geotechnical drill cores in the rock mechanics laboratory. According to data which is taken from (Bae Mountain Mining Corporation, 2018), amphibolite gneiss, leucocratic gneiss, schist and some quartz layers were observed in the content of the rock. The samples have a diameter of 63 mm. Amphibolite gneisses are layers of hornblende, plagioclase, and biotite minerals containing the dark-colored fine-medium particles. The other mineral of Leucocratic gneisses is light-colored layers containing a small number of ferromagnesian minerals. These layers contain at least 90% quartz, feldspar, and muscovite. Lastly, the schist layers are mostly composed of muscovite, chlorite, sericite, talc, biotite, feldspar, and quartz minerals. However, quartz and feldspar content in the schist samples is less than gneiss samples.

Figure 3.23 and Figure 3.24 represent some of the specimens before and after the experiments. The remaining specimen photos can be found in Appendix A.

Figure 3.23. Gneiss-schist samples with 63 mm diameter before test

Figure 3.24. Gneiss-schist samples with 63 mm diameter after test

At the end of 25 experiments, NLUCS-40, 37, 55, 56, 49, 57, 58, 41, 62, 47, and 48 specimens showed sudden temperature increase behavior at the failure moment.

3.5. Porosity Tests

Some rock properties have been considered as causes of the energy release. One of them is the porosity ratio in the rocks. In this context, density and porosity experiments were performed for andesite and marble samples, which were taken from rock blocks by coring. Effective and total porosity ratios of rock samples were calculated. For effective porosity, first of all, rock samples were kept in the water for two days, and their pores were allowed to absorb water. After weighing the saturated weight, the sample was placed in the desiccator for one day, and its dry weight was also found. The effective porosity ratios were then calculated using these values and the dimensions of the sample. Figure 3.25 shows these steps.

Figure 3.25. The samples in the water and in the desiccator

The effective porosity ratio was found by using the following formulas.

$$P_v = (W_{sat} - G_w)/\rho_w \quad (1)$$

$$B_v = \pi \times d^2 \times h \quad (2)$$

$$n_{eff} = \frac{P_v}{B_v} \times 100\% \quad (3)$$

By using these calculations, the effective porosity for andesite and marble samples were found as 5.81% and 0.59%, respectively.

After effective porosity calculations, total porosity ratios were calculated by using a pycnometer. In this method, rock samples were grinded under 0.2 mm.

The pycnometer is a small bottle fitted with a ground-glass stopper through which a capillary opening has been drilled. The pycnometer was first weighted dry and empty, and named P1. After that, the grinded rock sample was placed into the bottle. The weight was named P2. Subsequently, distilled water was added to pycnometer, shaking for one minute to allow water bubbles to escape. The resulting weight of this process was named P3. Finally, the pycnometer was weighed only by filling with distilled water, and named P4. Total porosity was calculated as a result of these processes. Figure 3.26 shows these steps.

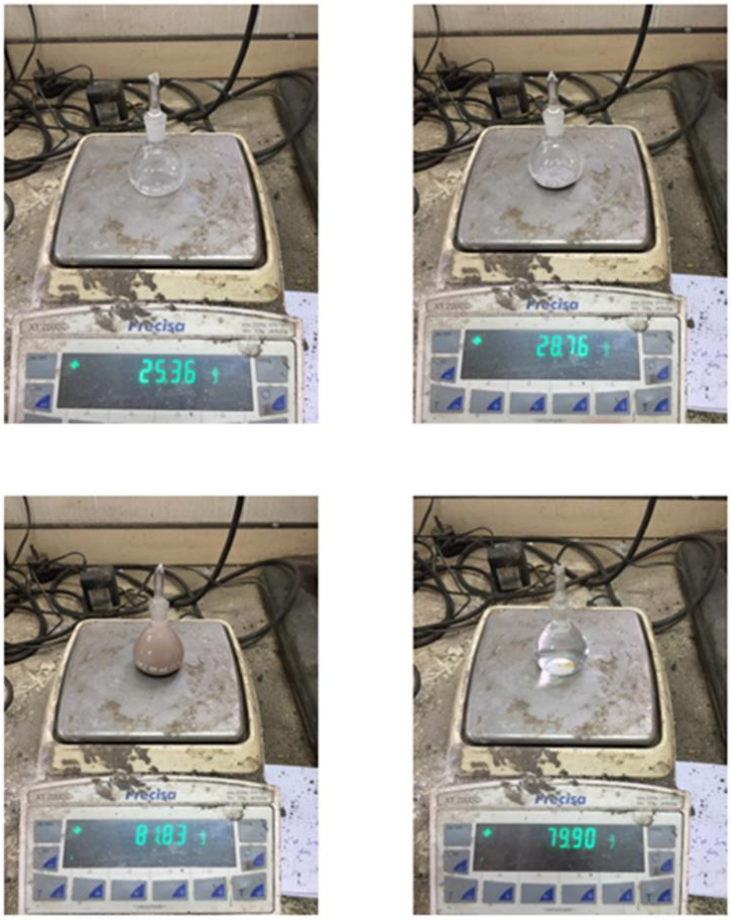

Figure 3.26. P1, P2, P3 and P4 weights of samples, respectively

The total porosity ratio was found by using the following formulas.

$$\mu_g = \frac{(P2-P1)\times\rho_w}{(P4+P2-P1-P3)} \quad (4)$$

$$\mu_d = \frac{G_w}{B_v} \quad (5)$$

$$n_{eff} = \frac{(\mu_g-\mu_d)}{\mu_d} \times 100\% \quad (6)$$

By using these calculations, the total porosity for andesite and marble samples were found as 20.97% and 10.79%, respectively.

CHAPTER 4

RESULTS AND DISCUSSION

This section covers the results of UCS tests of andesite, marble and gneiss-schist specimens. Andesite and marble specimens with different diameter size were prepared from rock blocks by using a coring machine at rock mechanics laboratory, whereas gneiss-schist specimens were taken as a results of geological drilling. Therefore, gneiss-schist specimens were tested into one diameter size. From the experimental results, UCS values for rock types were obtained. Besides, experiments were followed with the help of the thermal camera. Hence, thermal results and energy dissipation of different type of rock specimens were analyzed during UCS tests. Andesite, gneiss-schist, and marble specimens were named as based on diameter, capital initial letter of rock type and experiment order, respectively.

4.1. Determination of Thermal Change of Rock Specimens

Rock samples used in UCS tests were monitored with the thermal camera. The thermal camera gives information about the thermal change at the surface of the sample during the experiment. Temperature change amounts and regions provide information depending on the rock type.

4.1.1. Thermal Responses of Andesite Specimens

The UCS tests of andesite samples with 75 mm, 63 mm, 53 mm, and 42 mm diameter were carried out, respectively. Although all experiments were completed according to the procedure, the result of some experiments could not be examined by the thermal camera. There are two main reasons for this, failure is initiated within the sample and the amount of energy released might not be observed on the surface of the sample. The second reason is that failure might occur on the surface of the specimen that was not recorded with the thermal camera. As a result of the experiments, some samples

showed a considerable temperature increase at the failure plane. In contrast, some were characterized by lower temperature change. In order to perform a consistent review, samples with considerable temperature change and lower temperature change were evaluated as two individual groups. The samples which showed high temperature change at the failure moments were marked with "*" in the following Table 4.1, 4.2 and 4.9.

4.1.1.1. Thermographic analysis of Andesite samples with 75 mm diameter

The samples were named as 75 A-1, 75A-2, 75A-3, 75A-4, and 75A-5, respectively. As a result of the experiments, 75A-1, 75A-3, 75A-4, and 75A-5 samples showed a temperature increase during failure. The 75A-1 sample showed a considerable temperature increase on the failure plane, whereas other samples showed low temperature increase. The determination of the failure surface of 75A-1 sample can be seen in Figure 4.1 as an example. The figures of other samples which show temperature increase during failure can be seen in Appendix B.

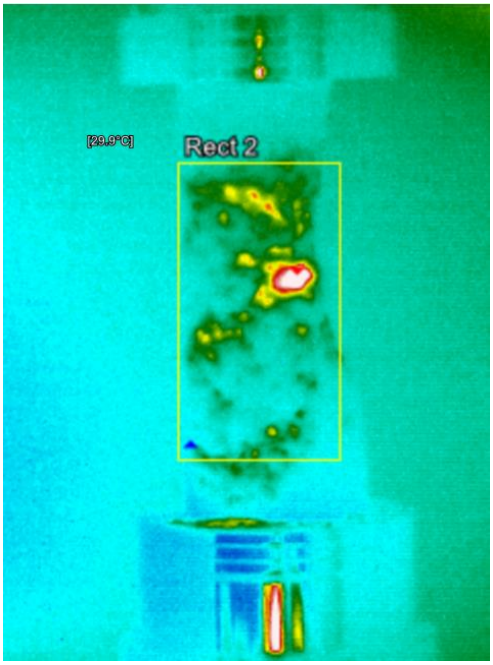

Figure 4.1. Failure plane detection of the 75A-1 sample by the thermal camera

According to Figure 4.1, Red and white color regions represent the high temperature bands. Hence, it can be said that these regions are related with high stress concentration points and failure regions. Particle ejection regions and failure planes can be obtained from these regions.

Figure 4.2 shows the force-time and temperature change-time graphs of the 75A-1 sample.

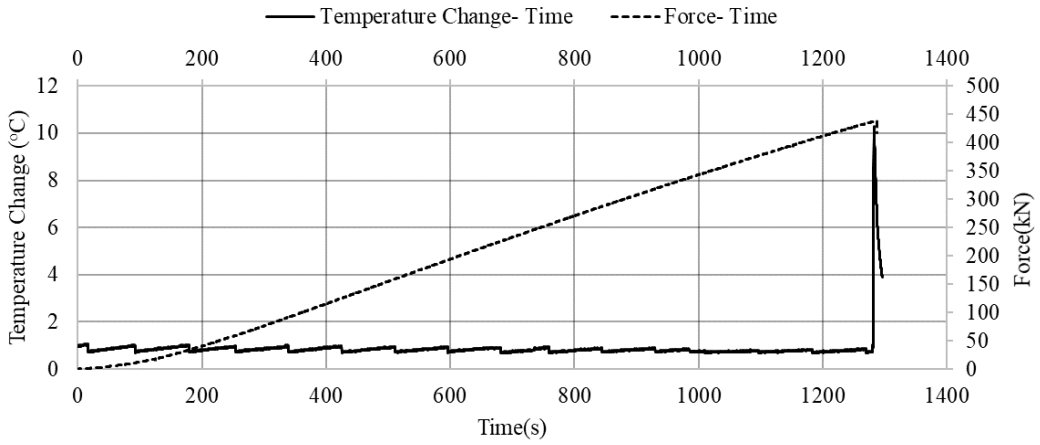

Figure 4.2 Temperature change- Force- Time graph of the 75A-1 sample

As it can be seen from Figure 4.2, the applied force reaches a maximum value and this can eventually be interpreted as the value at which the sample failed. Besides, there is a sudden increase in the temperature value during this time interval. This andesite sample failed at a load of 437.6 kN, and the temperature increase at this force value was found to be 10.29℃. The graphs of the other andesite samples with 75 mm diameter can be seen in Appendix C. Table 4.1 summarizes the results of the andesite samples with a diameter of 75 mm.

Table 4.1. *The UCS test results of the andesite samples with a diameter of 75mm*

Sample Code	Failure Load(kN)	Temperature Increase(℃)
75A-1	437.60	10.29*
75A-2	421.90	-
75A-3	437.40	1.88
75A-4	296.00	0.66
75A-5	330.50	0.81
Average	384.68	1.12

By considering Table 4.1, the average failure load of the andesite specimens with 75 mm diameter is found 384.68 kN. By isolating sample 75A-1, since it is compared only with specimens with a high temperature increase, the average temperature increase is found 1.12 ℃.

4.1.1.2. Thermographic analysis of Andesite specimens with 63 mm diameter

The samples were named as 63A-1, 63A-2, 63A-3, 63A-4, 63A-5, 63AA-1, 63AA-2, 63AA-3, 63AA-4, 63AA-5, 63AA-6, 63AA-7, 63AA-8, and 63AA-9, respectively. As a result of the experiments, samples 63A-1, 63A-2, 63A-4, 63A-5, 63AA-2, 63AA-4, 63AA-6, and 63AA-9 indicated a temperature increase during failure. The samples 63A-4 and 63AA-2 pointed out a considerable temperature increase on the failure plane, whereas other samples showed low temperature increase. The determination of the failure surface of the sample 63A-4 can be seen in Figure 4.3 as an example. The other samples which show temperature increase during failure can be seen in Appendix B.

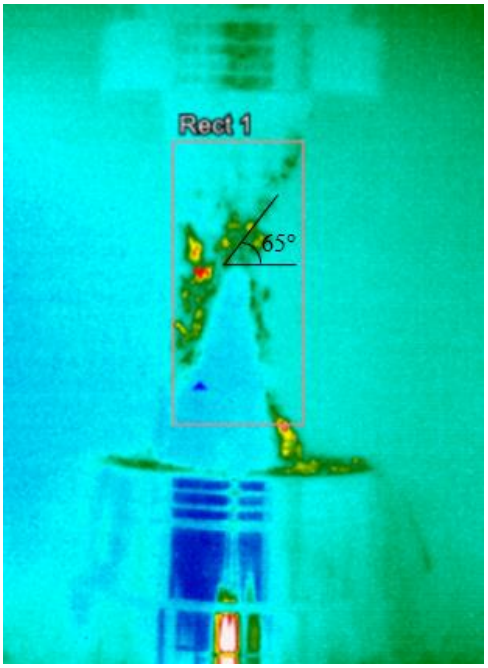

Figure 4.3. Failure plane detection of the 63A-4 sample by the thermal camera

According to Figure 4.3, red, yellow and green regions shows the failure planes. Relationship between the stress concentration regions, failure plane and high temperature difference regions can be seen from this figure. The angle of the failure plane was measured as 65° from the thermographic image.

Figure 4.4 shows the force-time and temperature change-time graphs of the sample 63A-4.

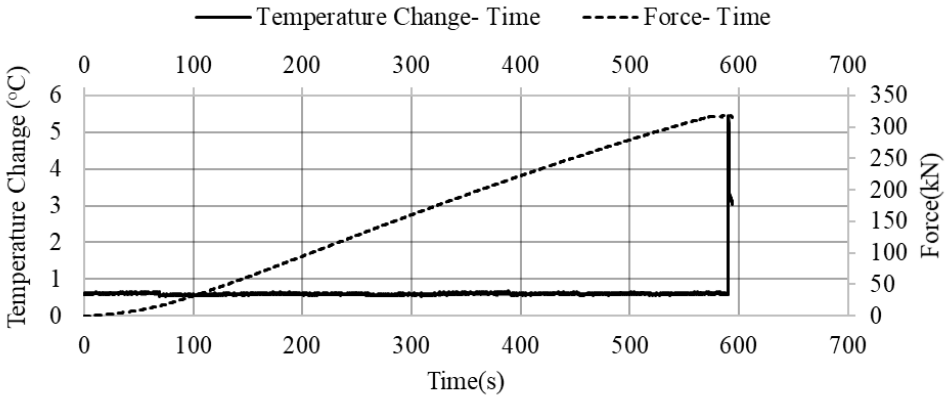

Figure 4.4. Temperature change- Force- Time graph of the 63A-4 sample

As it can be seen from Figure 4.4, this andesite sample failed at a load of 316.6 kN, and the temperature increase at this force value was found to be 5.44 ℃. The graphs of the other andesite samples with a diameter of 63 mm are provided in Appendix C. Table 4.2 summarizes the results of the andesite samples with a diameter of 63 mm.

Table 4.2. *The UCS test results of the andesite samples with a diameter of 63mm*

Sample Code	**Failure Load(kN)**	**Temperature Increase(℃)**
63A-1	300.50	1.75
63A-2	270.90	1.08
63A-3	249.20	-
63A-4	316.60	5.44*
63A-5	304.30	1.56
63AA-1	291.36	-
63AA-2	249.99	3.46*
63AA-3	199.14	-
63AA-4	208.73	1.61
63AA-5	269.87	-
63AA-6	175.70	1.65
63AA-7	282.19	-
63AA-8	285.99	-
63AA-9	263.02	1.3
Average	261.96	1.49

By considering Table 4.2, it is seen that the average failure load of the andesite samples with 63 mm diameter is found as 261.96 kN. The samples 63A-4 and 63AA-2 were evaluated individually by a comparison with only high temperature increase samples, the average temperature increase is found 1.49 ℃.

The heat might be generated due to friction of the grains. As given in Table 4.1 and 4.2, high temperature change could easily be observed during the catastrophic failure of rock specimens. Hence, it is considered that brittle failure causes the sudden temperature increase at the failure moment.

4.1.1.3. Thermographic analysis of andesite samples with 53 mm diameter

The samples were named as 53A-1, 53A-2, 53A-3, 53A-4 and 53A-5, respectively. As a result of the UCS tests, samples 53A-1, 53A-4, and 53A-5 indicated a temperature increase during failure. The determination of the failure surface of the sample named 53A-1 can be seen in Figure 4.5 as an example. The other samples which show temperature increase during failure are provided in Appendix B.

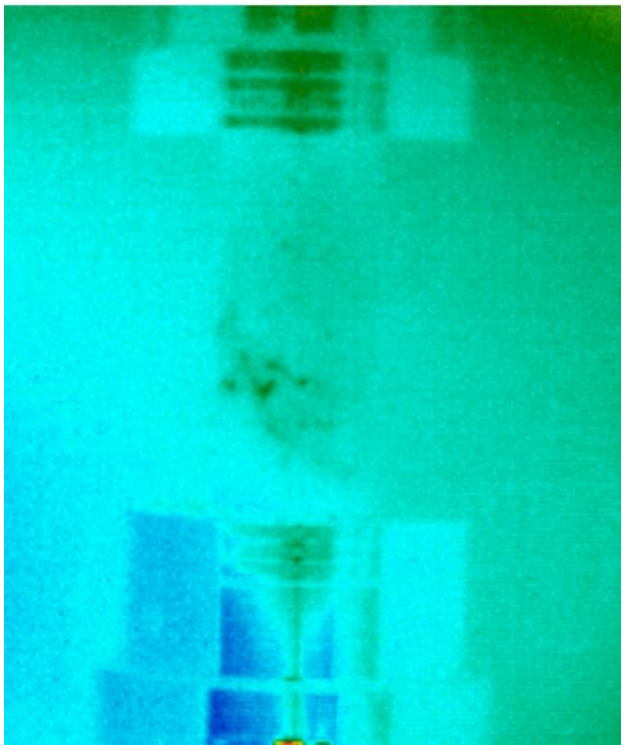

Figure 4.5. Failure plane detection of the 53A-1 sample by the thermal camera

According to Figure 4.5, there is no catastrophic failure by considering the temperature change during experiment. It can be still said that dark green regions can be represented as the failure region. Hence, detection of failure region can be analyzed even if the temperature increase at the failure plane is low.

Figure 4.6 represents the force-time and temperature change-time graphs of the sample 53A-1.

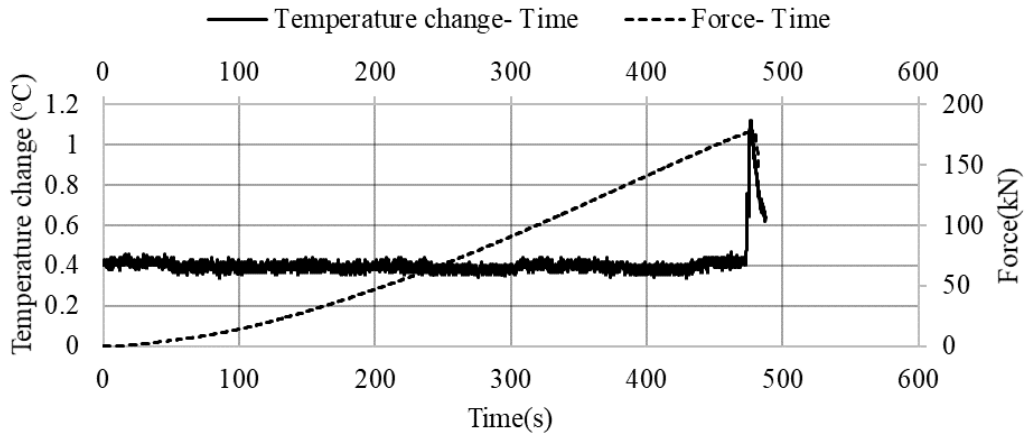

Figure 4.6 Temperature change- Force- Time graph of the 53A-1 sample

As it can be seen from Figure 4.6, this andesite sample failed at a load of 175.7 kN, and the temperature increase at this force value was found to be 1.12 ℃. The graphs of the other andesite samples with a 53 mm diameter are provided in Appendix C. Table 4.3 summarizes the results of the andesite samples with a diameter of 53 mm.

Table 4.3. *The UCS test results of the andesite samples with a diameter of 53 mm*

Sample Code	**Failure Load(kN)**	**Temperature Increase(℃)**
53A-1	175.70	1.12
53A-2	87.80	-
53A-3	186.30	-
53A-4	142.70	0.71
53A-5	193.40	0.67
Average	157.20	0.83

According to Table 4.3, The average failure load of the 53 mm diameter andesite samples is found as 157.2 kN. The average temperature increase is found as 0.83 ℃.

4.1.1.4. Thermographic analysis of andesite samples with 42 mm diameter

The samples were named 42A-1, 42A-2, 42A-3, 42A-4 and 42A-5, respectively. As a result of the experiments, samples 42A-2 and 42A-5 represented a temperature increase during failure. The determination of the failure surface of the sample 42A-2 can be seen in Figure 4.7 as an example. Other samples indicating a temperature increase during failure are provided in Appendix B.

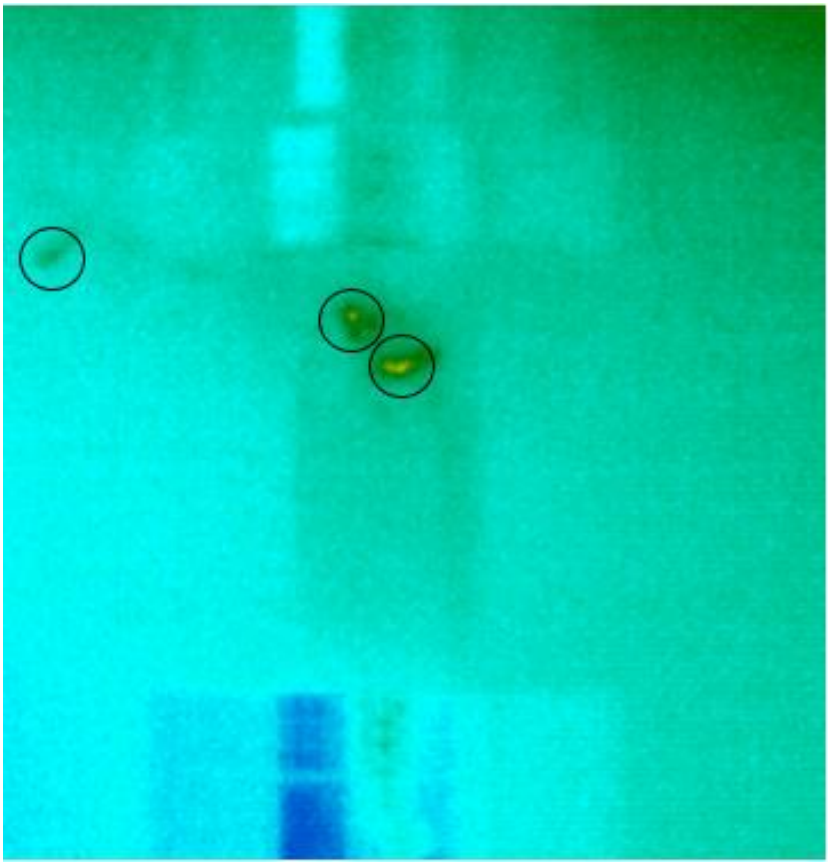

Figure 4.7. Failure plane detection of sample 42A-5 by the thermal camera

Figure 4.7 shows the temperature change during the UCS test. Yellow region in the figure represent the particle ejection region. Failure plane is also represented with this color and dark green region. Therefore, detection of failure plane could be obtained with the thermal camera.

Figure 4.8 shows the force-time and temperature change-time graphs of the sample 42A-5.

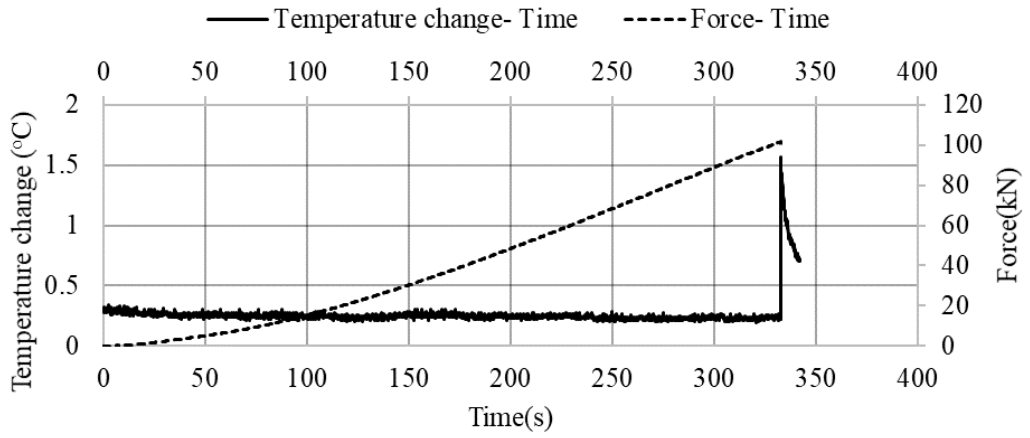

Figure 4.8. Temperature change- Force- Time graph of the 42A-5 sample

As it can be seen from Figure 4.8, this andesite sample failed at a load of 100.6 kN, and the temperature increase at this force value was found to be 1.57 ℃. The graphs of the other andesite samples with a diameter of 42 mm are provided in Appendix C. Table 4.4 summarizes the results of the andesite samples with a diameter of 42 mm.

Table 4.4. *The UCS results of the andesite samples with a diameter of 42mm*

Sample Code	**Failure Load(kN)**	**Temperature Increase(℃)**
42A-1	78.20	-
42A-2	115.60	0.61
42A-3	76.90	-
42A-4	59.50	-
42A-5	100.60	1.57
Average	86.20	1.09

According to Table 4.4, the average failure load of the andesite samples with 42 mm diameter is found as 86.2 kN. The average temperature increase is found as 1.09 ℃.

4.1.2. Thermal Responses of Marble Specimens

The sudden temperature increase observed on the failure plane of the andesite samples was not the case for the marble specimens. In contrast, marble samples showed a cooling behavior at the failure plane. The reason for this, as it is mentioned by other researchers in this field, could be explained by samples having different structures that is related to both the mineralogy and the structural composition of the material (Mineo & Pappalardo, 2006).

4.1.2.1. Thermographic analysis of marble specimens with 75 mm diameter

The temperature change could not be observed at any marble specimen with a diameter of 75 mm. Table 4.5 summarizes the results of the marble samples with a diameter of 75 mm.

Table 4.5. *The UCS results of the marble samples with a diameter of 75 mm*

Sample Code	Failure Load(kN)	Temperature Change(°C)
75M-1	224.20	-
75M-2	287.40	-
75M-3	404.90	-
75M-4	253.40	-
75M-5	299.90	-
Average	311.40	-

According to Table 4.5, the average failure load of the marble samples having 75 mm diameter is found 311.4 kN, and no temperature change was not observed.

4.1.2.2. Thermographic Analysis of Marble specimens with 63 mm diameter

The marble samples were named 63M-1, 63M-2, 63M-3, 63M-4,63M-5, 63MM-1, 63MM-2, 63MM-3 and 63MM-4, respectively. As a result of the experiments, the samples 63M-2, 63M-3 and 63M-4 showed a cooling behavior during experiments. The determination of the failure surface of the 63M-3 sample can be seen in Figure

4.9 as an example. Other samples indicating cooling behavior during experiments are provided in Appendix B.

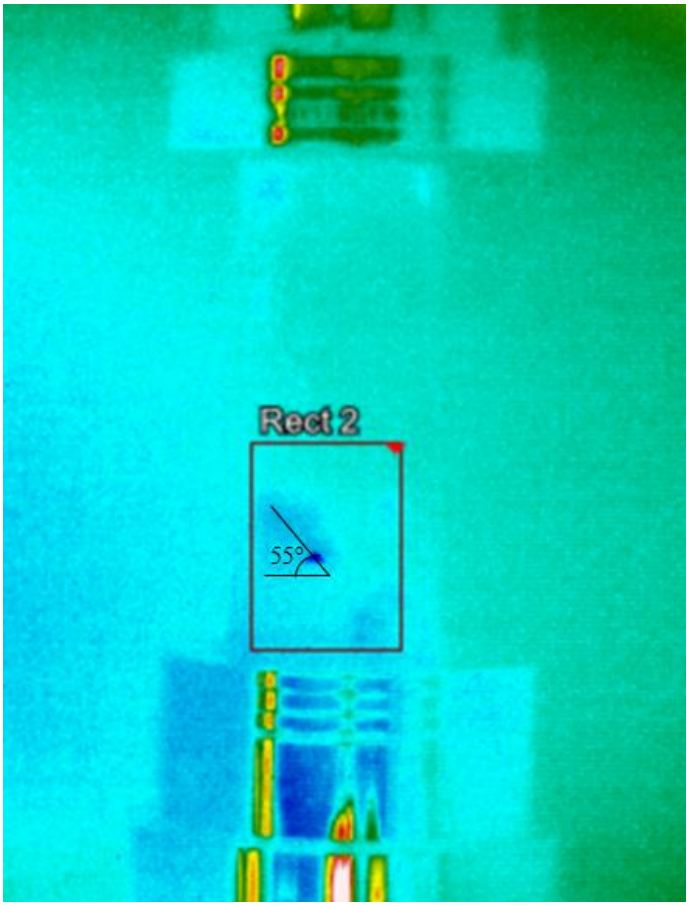

Figure 4.9. Failure plane detection of the 63M-3 sample by the thermal camera

Dark blue regions show the cooling regions at the sample. Accordingly, failure plane can be detected by analyzing these regions since the cooling behavior was seen at these points. Figure 4.10 shows the force-time and temperature change-time graphs of the sample 63M-3. The angle of the failure plane was measured as 55° from the thermographic image.

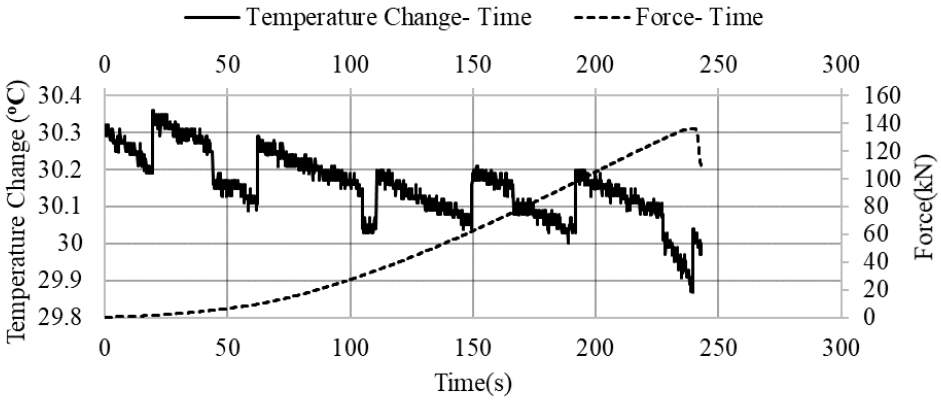

Figure 4.10. Temperature change- Force- Time graph of the 63M-3 sample

As it can be seen from Figure 4.10, this marble sample failed at a load of 135.2 kN, and the temperature decreased from 30.36 ℃ to 29.87 ℃. Therefore, the temperature change was found as 0.49 ℃. The graphs of the remaining marble samples with 63 mm diameter are given in Appendix C. Some marble samples showed a scattered temperature change during the experiments. In combination with the acoustic emission system and a thermal camera, this problem can be overcome, and a more accurate relationship can be achieved. Table 4.6 summarizes the results of the marble samples with a diameter of 63 mm.

Table 4.6. *The UCS results of the marble samples with a diameter of 63 mm*

Sample Code	**Failure Load(kN)**	**Temperature Change(℃)**
63M-1	125.20	-
63M-2	205.20	-0.64
63M-3	135.20	-0.49
63M-4	175.90	-0.38
63M-5	127.60	-
63MM-1	152.93	-
63MM-2	157.94	-
63MM-3	136.31	-
63MM-4	91.78	-
Average	145.34	-0.50

According to Table 4.6, The average failure load of the 63 mm diameter marble samples is found as 145.34 kN and the average temperature decrease is found as 0.50 ℃.

4.1.2.3. Thermographic Analysis of Marble specimens with 53 mm diameter

The marble samples were named 53M-1, 53M-2, 53M-3, 53M-4 and 53M-5, respectively. As a result of the experiments, three samples showed a cooling behavior during experiments. The determination of the failure surface of the sample 53M-2 can be seen in Figure 4.11 as an example. Other samples representing a cooling behavior during experiments are provided in Appendix B.

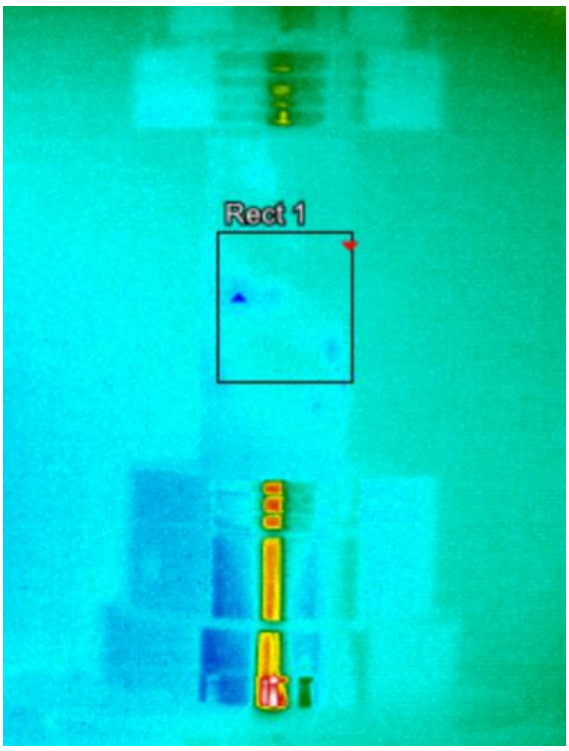

Figure 4.11. Failure plane detection of the 53M-2 sample by the thermal camera

According to Figure 4.11, failure plane for the marble sample could not be detected visually with the thermal camera. Instead of this, rectangular region is selected with the help of the software of thermal camera, and data from these region was transferred to computer. By analyzing this data, temperature decrease was followed during the

experiment from this region. Figure 4.12 shows the force-time and temperature change-time graphs of the sample 53M-2.

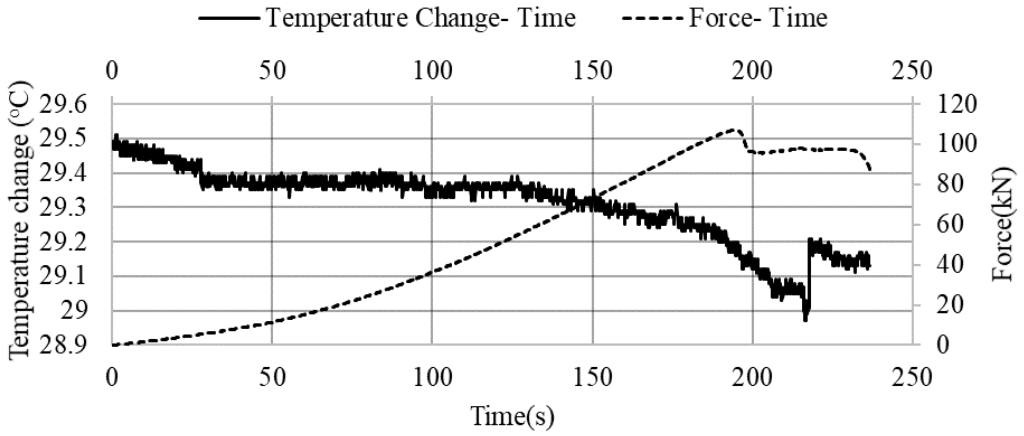

Figure 4.12. Temperature change- Force- Time graph of the 53M-2 sample

As it can be seen from Figure 4.12, this marble sample failed at a load of 106.1 kN, and the temperature decreased from 29.51 ℃ to 28.97 ℃. Therefore, the temperature change was found as 0.54 ℃. The graphs of the other marble samples with a 53 mm diameter are provided in Appendix C. Table 4.7 summarizes the results of the marble samples with a diameter of 53 mm.

Table 4.7. *The UCS results of the marble samples with a diameter of 53 mm*

Sample Code	**Failure Load(kN)**	**Temperature Change(℃)**
53M-1	110.10	-0.54
53M-2	106.10	-0.54
53M-3	119.30	-
53M-4	66.60	-0.66
53M-5	71.90	-
Average	94.80	-0.58

According to Table 4.7, The average failure load of the 53 mm diameter marble samples is found as 94.8 kN and the average temperature decrease is found as 0.58 ℃.

4.1.2.4. Thermographic Analysis of Marble Specimens with 42 mm diameter

The marble samples were named 42M-1, 42M-2, 42M-3, 42M-4 and 42M-5, respectively. As a result of the experiments, the samples 42M-2, 42M-3 and 42M-5 showed a cooling behavior during experiments. The determination of the failure surface of the sample 42M-3 can be seen in Figure 4.13 as an example. Other samples which indicate cooling behavior during experiments are provided in Appendix B.

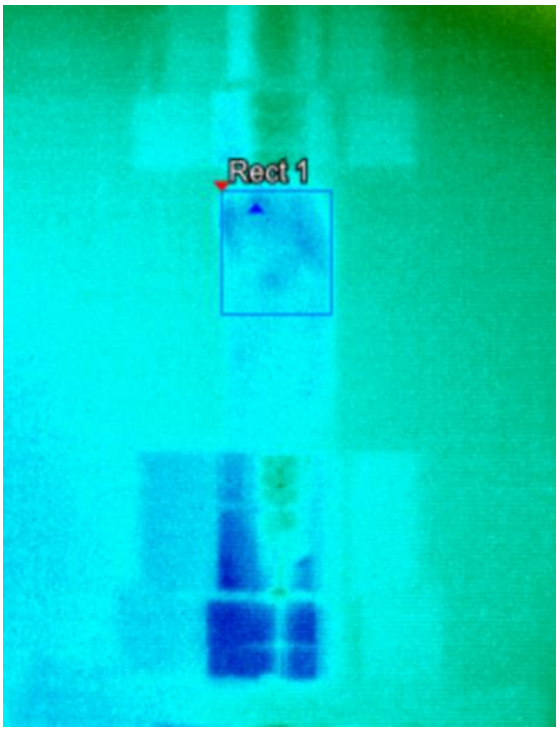

Figure 4.13. Failure plane detection of the 42M-3 sample by the thermal camera

According to Figure 4.13, failure plane and cooling behavior region of the sample can be detected with the help of the thermal camera. Dark blue regions show the cooling points of the sample during the experiment. Figure 4.14 shows the force-time and temperature change-time graphs of the 42M-3 sample.

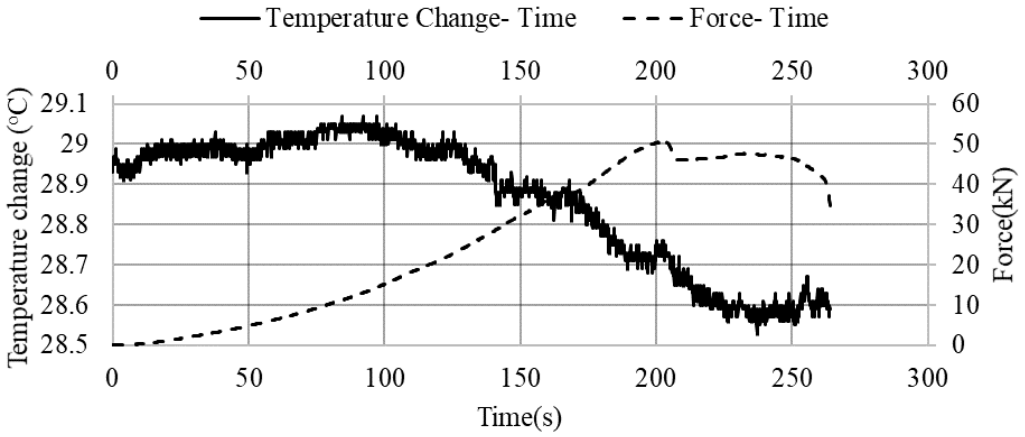

Figure 4.14. Temperature change- Force- Time graph of the 42M-3 sample

As it can be seen from Figure 4-14, this marble sample failed at a load of 49.5 kN, and the temperature decreased from 29.07 ℃ to 28.53 ℃. Therefore, the temperature change was found as 0.54 ℃. Results of other marble samples with a 42 mm diameter are provided in Appendix C. Table 4.8 summarizes the results of the marble samples with a diameter of 42 mm.

Table 4.8. *The UCS results of the marble samples with a diameter of 42 mm*

Sample Code	**Failure Load(kN)**	**Temperature Change(℃)**
42M-1	99.09	-
42M-2	44.00	-0.47
42M-3	49.40	-0.54
42M-4	12.30	-
42M-5	45.80	-0.46
Average	50.12	-0.49

According to Table 4.8, The average failure load of the 42 mm diameter marble samples is found as 50.12 kN and the average temperature decrease is found as 0.49 ℃.

4.1.3. Thermal Responses of Gneiss- Schist Specimens

Twenty-five gneiss samples were prepared for UCS tests at a displacement rate of 0.2 mm/s. The thermal camera monitored the specimens throughout the experiments. As a result of the experiments, eleven samples showed a sudden increase in the temperature value at the failure moment.

The determination of the failure surface of the sample NLUCS-56 can be seen in Figure 4.15 as an example. Other samples which show temperature increase at failure moment are provided in Appendix B.

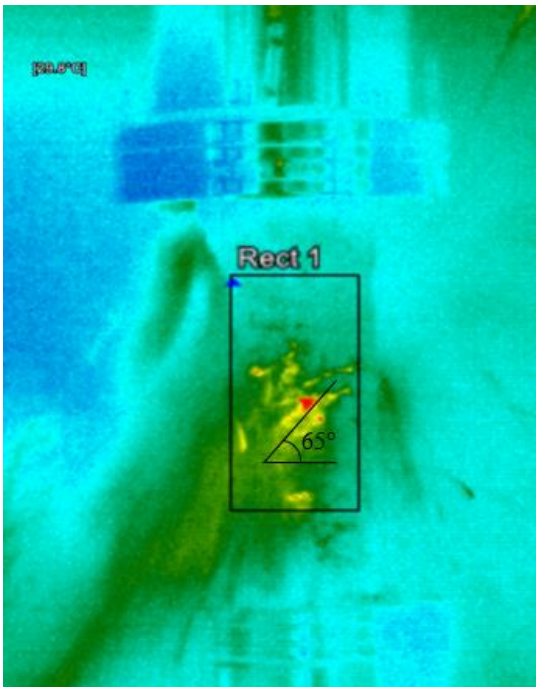

Figure 4.15. Failure plane detection of the NLUCS-56 sample by the thermal camera

From the Figure 4.15, failure plane could detect with thermal camera clearly. The red and yellow color regions directly related with the stress concentration regions. These regions represent the failure plane of the specimen. Particle spalling from the sample can be also detect with the help of the thermal camera. Figure 4-16 shows the force-time and temperature change-time graphs of the sample NLUCS-56. The angle of the failure plane was measured as 65° from the thermographic image.

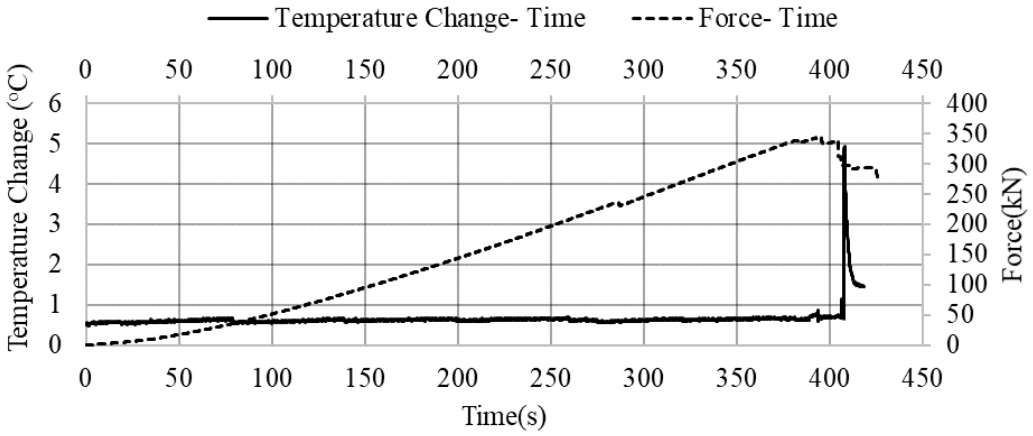

Figure 4.16. Temperature change- Force- Time graph of the NLUCS-56 sample

As it can be seen from Figure 4.16, this sample failed at a load of 345.8 kN, and the temperature increase at this force value was found to be 4.94 ℃. The graphs of the remaining gneiss-schist samples with 63 mm diameter are provided in Appendix C. Table 4.9 summarizes the results of the gneiss-schist samples with a diameter of 63 mm. As in the andesite samples, high-temperature increasing cases and lower temperature changing samples were investigated separately in two different groups. The samples which showed high temperature change at the failure moments were marked with "*" at the following Table 4.9.

Table 4.9. The UCS results of the gneiss-schist samples with a diameter of 63 mm

Sample Code	**Failure Load (kN)**	**Temperature Increase(°C)**
NLUCS-46	480.15	-
NLUCS-40	443.69	18.27*
NLUCS-37	104.13	3.2
NLUCS-55	243.97	2.41
NLUCS-56	345.80	4.94*
NLUCS-59	228.82	-
NLUCS-50	327.02	-
NLUCS-54	177.39	-
NLUCS-42	240.97	-
NLUCS-49	419.31	5.51*
NLUCS-39	161.01	-
NLUCS-57	242.49	3.84
NLUCS-53	401.50	-
NLUCS-58	118.47	3.08
NLUCS-45	453.70	-
NLUCS-41	146.40	1.04
NLUCS-14	668.91	-
NLUCS-62	152.04	1.46
NLUCS-34	386.08	-
NLUCS-38	468.24	-
NLUCS-47	355.94	2.53
NLUCS-35	193.66	-
NLUCS-48	337.05	2.73
NLUCS-44	269.75	-
NLUCS-61	410.31	-
Average	311.07	2.54, 9.57*

According to Table 4.9, the average failure load of the 63 mm diameter gneiss- schist samples is found 311.07 kN and the average temperature increase for samples indicating low temperature change is found as 2.54 ℃, whereas the average temperature increase for samples showing high temperature increase is found as 9.57 ℃.

4.2. Determination of Radiation Energy of Rock Specimens

As a result of the deformation of rock samples, energy is released in different forms, such as elastic energy, plastic energy, radiation energy, and kinetic energy (Zhao & Xie, 2008). The total amount of the released energy can be measuring the area under stress-strain graphs (Roylance, 2001). With the help of the thermal camera, it is possible to obtain temperature difference values during the experiment and at the moment of failure. By using these values, the amount of energy from the radiation can be found ("Rates of Heat Transfer", 2019). The thermal exchange rate can be found with the help of the following formula;

$$Thermal\ Exchange\ Rate = k \times \frac{A}{h} \times (\Delta T) \quad (7)$$

The obtained value can be multiplied by the duration of the experiment, and the amount of the radiation energy generated during the experiment can be estimated.

$$Radiation\ Energy\ = Thermal\ Exchange\ Rate\ \times (\Delta t) \quad (8)$$

The total released energy amount can be found from stress-strain graphs and the ratio of the radiation energy to the total energy amount can be estimated.

Different types of rocks were used in the experiments, and the thermal conductivity coefficients for each of these rocks are different, given as follows (Cermak & Ryback, 1982 for andesite, marble, gneiss and schist as 3.20, 3.00, 3.24, 3.14, respectively.

For gneiss- schist samples, the average of gneiss and schist values was taken as 3.19. As a result, different rates of thermal exchange rates were found for each sample.

4.2.1. Radiation Energy of Andesite Specimens

Andesite samples of different diameters were prepared for UCS tests at a displacement rate of 0.002 mm/s. As a result, dissipated radiation energies of the specimens were compared with each other. Tables 4.10 shows the radiation energy of the andesite samples with 75 mm diameter. The samples which showed high temperature change at the failure moments were marked with "*" in Table 4.10.

Table 4.10. *The amount of radiation energy of andesite samples with different diameter*

Diameter(mm)	Sample Code	Total Energy (kJ)	Radiation Energy (kJ)	Radiation Energy (%)
75	75A-1*	364.58*	297.18*	81.51*
	75A-3	355.80	121.43	34.13
	75A-4	290.40	83.55	28.77
	75A-5	272.20	93.02	34.18
	Average	306.10	99.33,297.18*	32.36,81.51*
63	63A-1	362.40	95.62	26.38
	63A-2	324.50	87.88	27.08
	63A-4*	421.50*	148.57*	35.24*
	63A-5	364.10	124.64	34.23
	63AA-2*	331.27*	129.85*	39.20*
	63AA-4	244.99	106.62	43.52
	63AA-6	193.25	118.55	61.35
	63AA-9	331.82	113.57	34.23
	Average	303.51	107.81,139.21*	37.79,37.22*
53	53A-1	328.80	60.33	18.35
	53A-4	250.90	61.82	24.64
	53A-5	333.00	46.81	15.65
	Average	304.20	56.32	19.55
42	42A-2	293.70	26.02	8.86
	42A-5	251.90	15.15	6.01
	Average	272.80	50.59	7.44

As mentioned before, specimens that indicated a low temperature increase and high temperature increase were compared separately in the two groups. Table 4.11 shows the overall results for the samples showing low temperature increase at the failure moment.

Table 4.11. *The overall results of the andesite samples with low temperature increase*

Rock Type	Failure Load (kN)	Temperature Increase (°C)	Radiation Energy (kJ)	Radiation Energy (%)
Andesite	223.21	1.21	82.50	28.39

Table 4.11 provides information about the overall outcome of temperature increase and the energy amount of andesite samples with low temperature increase. Accordingly, the average load at failure of these andesite samples was 223.21 kN. The average temperature increase amount at the failure plane was found to be 1.21°C. The radiation portion of the total energy had an average of 82.50 kJ. This energy amount has a percentage of 28.39 of total energy amount.

Table 4.12 shows the overall results for the samples showed high temperature increase at the failure moment.

Table 4.12. *The overall results of the andesite samples with high temperature increase*

Sample Code	Failure Load (kN)	Temperature Increase (°C)	Radiation Energy (kJ)	Radiation Energy (%)
75A-1	437.60	10.29	297.18	81.51
63A-4	316.60	5.44	148.57	35.24
66AA-2	249.99	3.46	129.85	39.20
Average	334.75	6.49	191.87	51.98

According to Table 4.12, the temperature increase at the moment of failure for andesite samples with 75 mm diameter were about 6 °C higher compared to the temperature readings taken from 63 mm diameter samples. In addition, it has been observed that

the amount of radiation energy was about 170 kJ higher than the amount of the radiation energy of 63 mm diameter samples. Hence, temperature and released radiation energy amounts were increased with the increased diameter size of the specimens. Therefore, more failure load causes more temperature increase at the specific region and more energy release from this region. As a result, the average temperature increases for the samples with high temperature increase at the failure moment was found as 6.49 ℃. Average radiation energy amount was found as 191.87 kJ.

The reason of the energy dissipation from the specimen is considered as dislocation of the grains from the failure plane of the specimens. Figure 4.17 shows the microscopic image of the failure plane of andesite specimen.

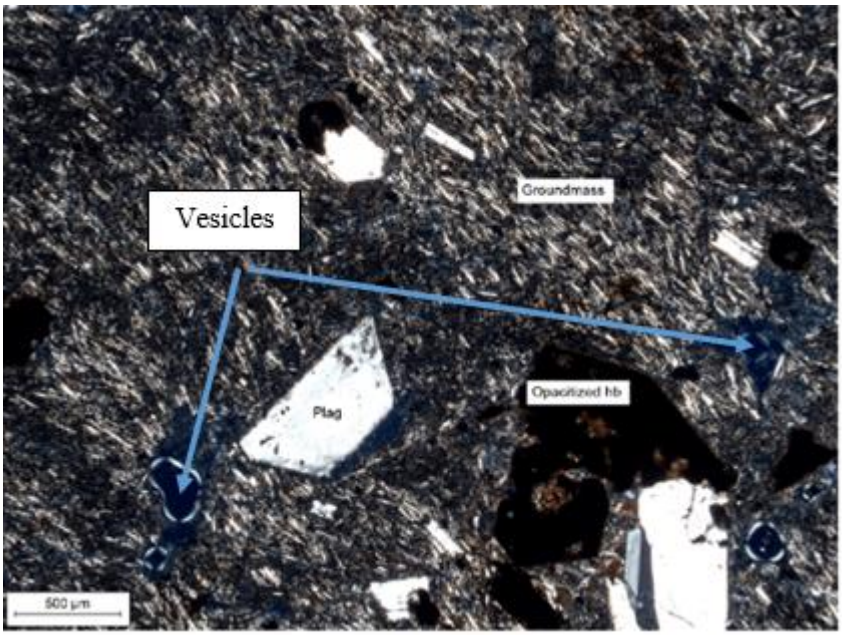

Figure 4.17. Microscopic image of the andesite samples

According to Figure 4.17, vesicle development at some regions were detected under microscope. These vesicles arise from the dislocation of the grains around these regions. Hence, dislocation of the grains and the formation of the vesicles causes more radiation energy release from the specimen.

4.2.2. Radiation Energy of Marble Specimens

Marble samples of different diameters were prepared for UCS tests at a displacement rate of 2 mm/s. As a result, dissipated radiation energy amounts were compared with each other. No temperature decrease was detected in the 75 mm diameter marble samples. Tables 4.13 shows the results of the marble samples with different diameter.

Table 4.13. *The result of the energy examination of marble samples with different diameter*

Diameter(mm)	Sample Code	Total Energy (kJ)	Radiation Energy (kJ)	Radiation Energy (%)
63	63M-2	141.60	24.03	16.97
	63M-3	76.95	7.01	9.11
	63M-4	107.33	22.12	20.61
	Average	108.63	17.72	15.56
53	53M-1	93.37	15.08	16.15
	53M-2	100.78	12.95	12.85
	53M-4	130.61	26.84	20.55
	Average	108.25	18.29	16.52
42	42M-2	90.39	12.13	13.42
	42M-3	132.62	12.97	9.78
	42M-5	98.11	12.95	13.20
	Average	107.04	12.68	12.13

By considering the different diameters, Table 4.14 summarizes the overall energy results of all marble samples.

Table 4.14. *The result of the energy examination of all marble samples*

Rock Type	Failure Load (kN)	Temperature Decrease (°C)	Radiation Energy (kJ)	Radiation Energy (%)
Marble	145.94	0.53	16.24	14.74

Table 4.14 provides information about the overall outcome of the energy amount of marble samples. Accordingly, the average failure load of marble samples was 145.94 kN. The average temperature decrease amount at the failure plane was found to be 0.53 ℃ and the radiation portion of the total energy had an average of 7.33 kJ.

4.2.3. Radiation Energy of Gneiss- Schist

As in the andesite samples, high-temperature increase indicating samples and low temperature increasing samples were investigated separately in two different groups. Table 4.15 summarizes the overall result for the gneiss- schist samples with low temperature increase at the failure plane.

Table 4.15. *The overall results of the gneiss- schist samples with low temperature increase*

Sample Code	Failure Load (kN)	Temperature Increase (℃)	Radiation Energy (kJ)	Radiation Energy (%)
NLUCS-37	104.14	3.20	24.94	43.27
NLUCS-55	243.97	2.41	63.22	27.13
NLUCS-57	292.49	3.84	40.81	17.96
NLUCS-58	118.47	3.08	10.37	19.54
NLUCS-41	146.40	1.04	31.63	37.40
NLUCS-62	152.04	1.46	21.90	29.41
NLUCS-47	355.94	2.53	106.16	28.91
NLUCS-48	337.05	2.73	71.11	21.84
Average	218.82	2.54	46.27	28.18

Table 4.15 provides information about temperature increase and radiation energy at the failure moments for the gneiss-schist samples. Accordingly, it was observed that released radiation energy amounts is increased with higher failure load. As a result, for the first group of gneiss- schist samples, average failure load, temperature increase and radiation energy were found as 218.82 kN, 2.54 ℃ and 48.27 kJ, respectively.

Table 4.16 provides information about the second group samples which showed high temperature increase at the failure plane.

Table 4.16. *The overall results of the gneiss- schist samples with high temperature increase*

Sample Code	Failure Load (kN)	Temperature Increase (°C)	Radiation Energy (kJ)	Radiation Energy (%)
NLUCS-56	345.80	4.94	91.81	28.37
NLUCS-49	419.31	5.51	192.21	41.78
NLUCS-40	443.69	18.27	288.36	55.99
Average	402.93	9.57	190.79	42.05

As it can be seen from Table 4.16, released radiation energy and temperature increase at the failure plane increased with the failure load. As a result, it was observed that average failure load, temperature increase and radiation energy were 402.93 kN, 9.57 °C and 190.79 kJ, respectively.

4.3. Thermographic and Energy Analysis of Rock Specimens

As a result of the experiments, energy types such as radiation energy, kinetic energy, acoustic energy are revealed by the failure of the samples (Zhao & Xie, 2008). In this thesis study, the amount of radiation energy was examined by the temperature difference, which was measured with the help of a thermal camera. Experiments were carried out on different rock types and different specimen diameters. Hence, the effect of the temperature and energy change on these samples were examined.

4.3.1. Thermographic and Energy Analysis of Different Types of Rock Samples with Same Diameter

Specimens that indicated a high temperature increase and a low temperature profile were compared separately as two different groups. Table 4.17 provides overall information about the 63 mm diameter samples with low temperature increase at the failure plane. Since different types of samples were compared, relationship between the UCS value, temperature change, and released radiation energy amounts were compared. A temperature increase was observed for andesite and gneiss-schist

samples at the failure moment. However, for marble samples, temperature decrease was observed during the experiments.

Table 4.17. *Average results of the 63 mm diameter size Andesite, Gneiss- Schist and Marble Samples with low temperature increase at the failure plane*

Rock Type	UCS (MPa)	Temperature Change (°C)	Radiation Energy (kJ)	Radiation Energy (%)
Andesite	79.10	1.49	107.81	37.79
Gneiss- Schist	99.10	2.54	46.27	28.18
Marble	48.70	-0.50	17.72	15.56

According to the results of the andesite and gneiss-schist samples, it was seen that the increase in the strength results defined a similar trend in the temperature increase at the failure moment. On the contrary, there was a decrease in the amount of radiation energy emitted with increasing strength. The main reason for this is thought to be the effect of the structural differences such as the grain structures of different rock types on the failure behavior (Salami et al., 2017). As a result, it is concluded that the increase in the UCS values is proportional to the increase in the temperature at the time of failure. In Figure 4.18, the amount of the temperature recorded for andesite and gneiss- schist samples according to failure load values for each sample can be illustrated individually.

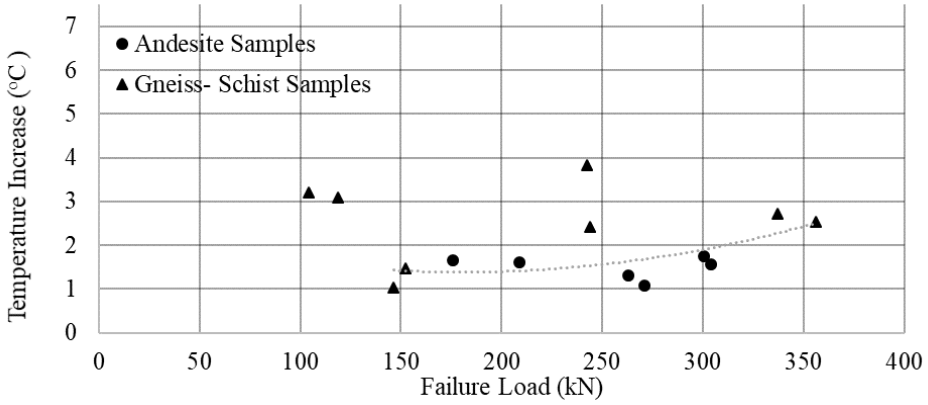

Figure 4.18. Temperature Increase- Failure Load graph of Andesite and Gneiss- Schist Samples with low temperature increase

According to Figure 4.18, andesite samples follow the trend line, whereas gneiss-schist samples showed more scattered behavior. Hence, for the samples with the low temperature increase at the failure plane, investigation of the results separately can be misleading. Figure 4.19 shows the graphs of the amount of radiation energy released and failure load of andesite and gneiss-schist samples.

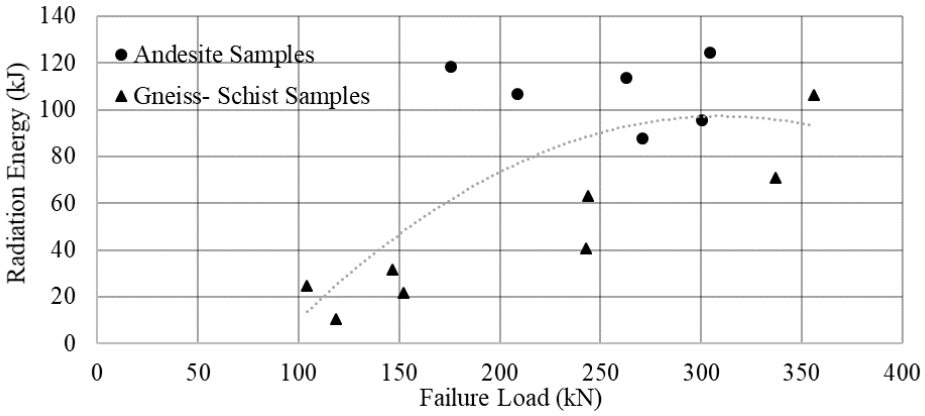

Figure 4.19. Radiation Energy- Failure Load graph of Andesite and Gneiss- Schist Samples with low temperature increase

According to Figure 4.19, the samples with a low temperature profile also not follow a distinctive trend and it can be said that released energy amounts increase with the increasing failure load values.

As a result, the samples with low temperature increase at the failure plane indicate that there is a relationship between the failure load, the temperature increase at failure moment, and the released energy amounts. Since the thermal camera used during the experiments is not a high-speed device, these results cannot be considered as representing the thermography of the specimens completely. The results can be considered as preliminary and indicated that the increase of failure load is observed similarly in both the temperature and the amount of energy produced.

The temperature and energy release occur through the pores of the material. Porosity rates of the samples taken from rock blocks were compared and the relationship

between the porosity and released energy was also investigated. In this context, porosity ratios of andesite and marble samples were measured. The effective porosity and total porosity rates of the andesite samples was 5.65% and 20.97%, respectively. The effective and total porosity rates of the marble samples was 0.59% and 10.79, respectively. Radiation energy amounts from the andesite and marble samples were 107.81 kJ and 17.72 kJ, respectively. Hence, it can be said that greater porosity is related with greater amount of released energy from the samples.

As in the low temperature increase samples, the samples with high temperature increase were investigated in a similar way. Table 4.18 summarizes the overall information about the 63 mm diameter size samples with high temperature increase at the failure plane.

Table 4.18. *Average results of the 63 mm diameter size Andesite, Gneiss- Schist and Marble Samples with high temperature increase at the failure plane*

Rock Type	**UCS (MPa)**	**Temperature Change (°C)**	**Radiation Energy (kJ)**	**Radiation Energy (%)**
Andesite	79.10	4.45	139.21	37.22
Gneiss- Schist	99.10	9.58	190.79	42.05

According to the results of the andesite and gneiss- schist samples, it was seen that the increase in the strength results is similar to the temperature increase at the failure moment. There was also an increase in the amount of radiation energy emitted. These results can be analyzed better in the samples with high temperature change as it can be seen from Table 4.18. The reason is that more data was obtained from these experiments compared to samples with low temperature increase at the failure moment. As a result, it is concluded that the increase in the UCS values is proportional to the increase in the temperature at the time of failure. In Figure 4.20, the amount of the temperature produced by andesite and gneiss- schist samples according to failure load values for each sample can be seen separately.

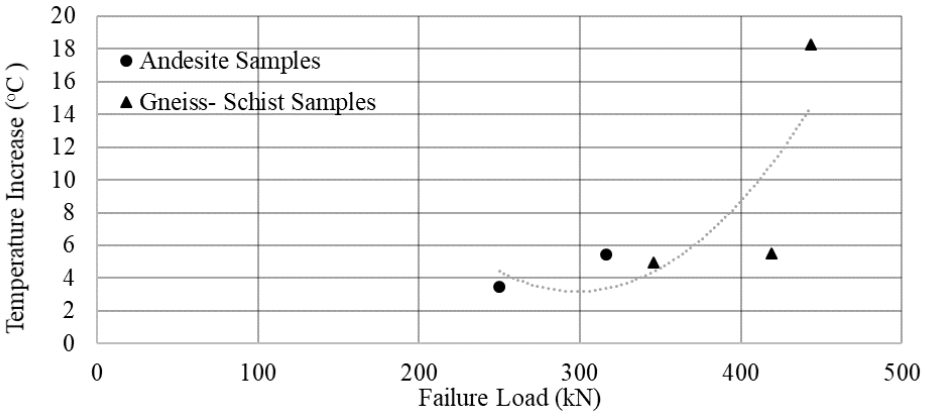

Figure 4.20. Temperature Increase- Failure Load graph of Andesite and Gneiss- Schist Samples with high temperature increase

According the Figure 4.20, there is a strong correlation between the increase in the failure load and temperature increase at the moment of failure. This graph also supports that analysis of the samples with high temperature changes at the failure plane provides more reliable and accurate results. As a result, failure load and temperature increase on the gneiss- schist samples were higher than the andesite samples. Released radiation energy amounts were also compared. Figure 4.21 shows graphs of the amount of radiation energy released and failure load of andesite and gneiss- schist samples.

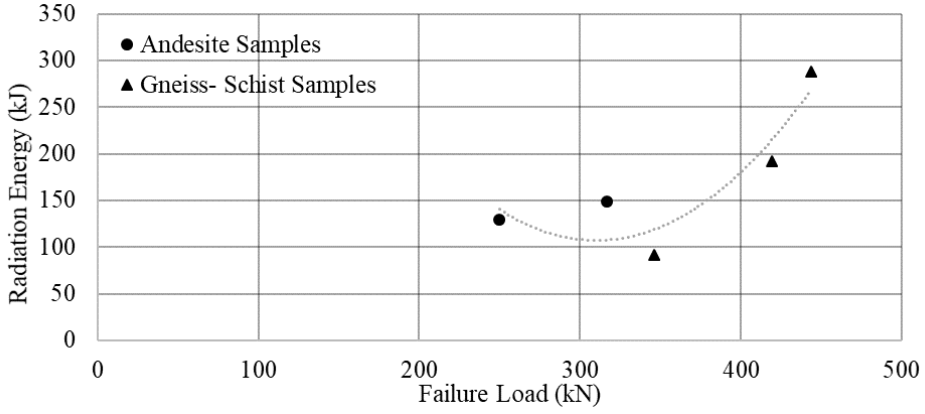

Figure 4.21. Radiation Energy- Failure Load graph of Andesite and Gneiss- Schist Samples with high temperature increase

According to Figure 4.21, there is also a strong correlation between the radiation energy amount and failure load. Accordingly, gneiss- schist samples release more radiation energy during the UCS tests since they are able to resist higher load values.

For andesite and gneiss-schist samples with high temperature increase, correlation between the angle of failure plane and temperature increase at the failure moment was also investigated. Figure 4.22 shows the relationship between the angle of failure plane and temperature increase at the failure moment of andesite samples.

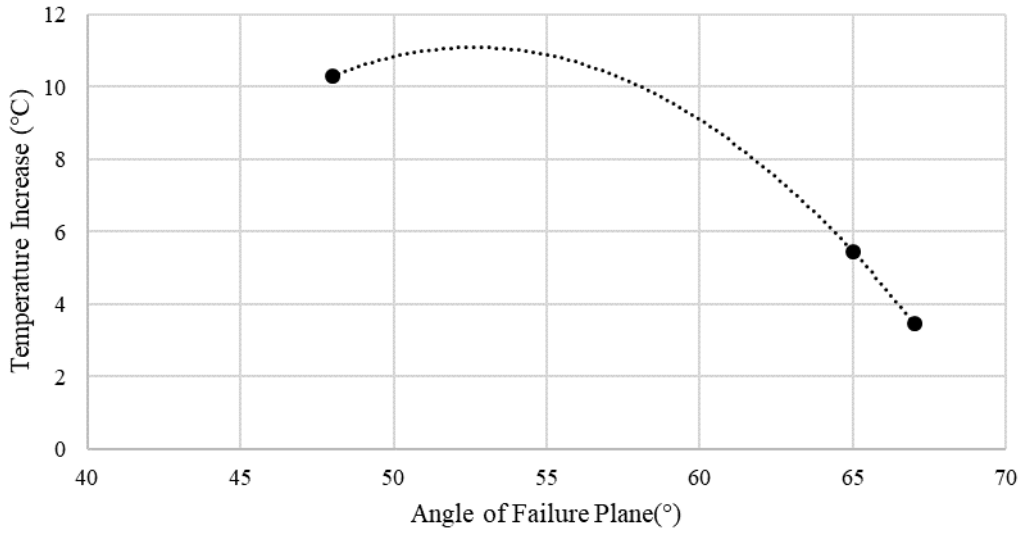

Figure 4.22. Angle of Failure Plane- Temperature Increase graph of Andesite Samples with high temperature increase

According to Figure 4.22, lower temperature increase at the failure moment was observed with the increase in the failure plane angle. The mechanism of the lower temperature increase in specimens with higher failure plane angle could be explained by the relatively lower amount of shear force and friction observed. An extreme case for this behavior is vertical splitting of the specimen where a temperature increase might not be recorded. Same analysis and results were obtained for gneiss-schist type of samples. Figure 4.23 shows the relationship between the angle of failure plane and temperature increase of gneiss-schist samples.

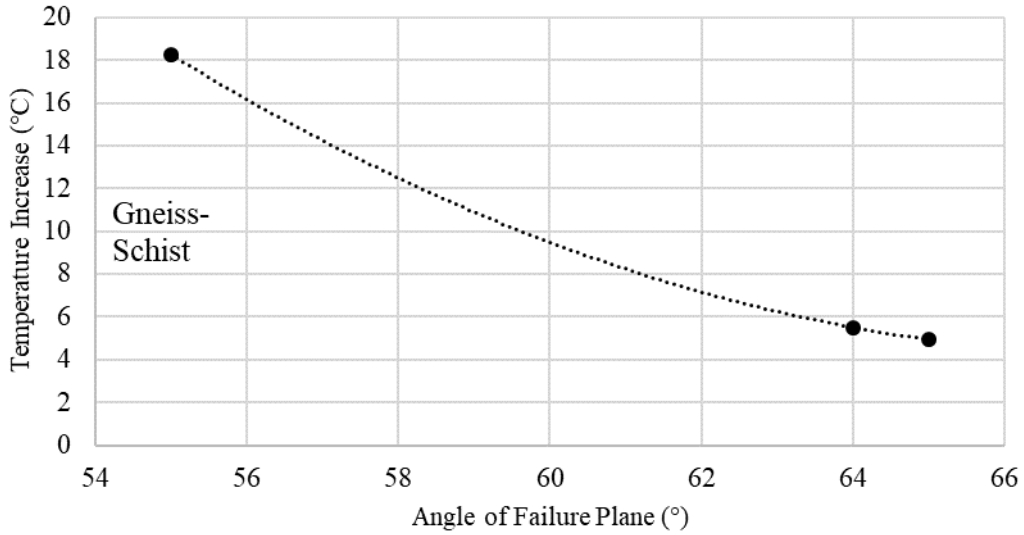

Figure 4.23. Angle of Failure Plane- Temperature Increase graph of Gneiss-Schist Samples with high temperature increase

According to Figure 4.23, as in the results of andesite samples, lower temperature increase was obtained at the failure moment of gneiss-schist samples with the increase in the failure plane angle. Lower failure plane angle causes more contact between the grains. Therefore, this contact results in higher temperature increase at the failure moment of the specimens. As also stated in various studies in the literature, this behavior represents brittle rock behavior. Hence, it is seen that brittle rocks cause higher temperature increase at the failure moment.

4.3.2. Thermographic and Energy Analysis of Same Type of Rock Samples with Different Diameters

In this thesis study, andesite rock samples with different diameters were prepared and tested. 75 mm, 63 mm, 53 mm, and 42 mm diameter andesite samples were used UCS tests and the resulting temperature change and the released radiation energy amounts were compared. Table 4.19 summarizes the overall results of the andesite samples of different diameters with low temperature increase at the failure plane.

Table 4.19. *Average results of different size of Andesite samples with low temperature increase at the failure plane*

Sample Diameter (mm)	Failure Load (kN)	Temperature Increase (°C)	Radiation Energy (kJ)	Radiation Energy (%)
75	354.63	1.12	99.33	32.36
63	253.86	1.49	107.81	37.80
53	170.60	0.83	56.32	19.55
42	108.10	1.09	20.59	7.44
Average	236.79	1.22	82.50	28.39

Table 4.19 indicates that the failure load of the andesite samples increased with larger diameter, as expected. However, the relationship between the temperature increase and the failure load could not be represented accurately. The reason is that the range between the temperature changes of the samples during failure were very close to each other. Hence, the relationship between the increase in the failure load and the increase in the temperature change is not clear. An analysis of the high temperature change during the failure may lead to more accurate results. Figure 4.24 shows the amount of the temperature change recorded for the andesite samples with different diameter sizes according to the failure load values for each sample.

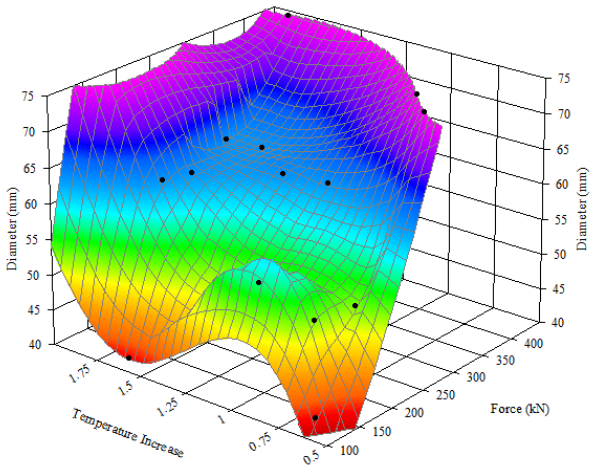

Figure 4.24. Temperature Increase-Failure Load graph of Andesite Samples with low temperature increase

According to Figure 4.24, higher temperature increase trend can be observed with the increasing diameter and failure load for the andesite samples with low temperature increase. Hence, preliminary results and inferences can be obtained with the longwave thermal camera if the temperature increase is low at the failure moment.

Figure 4.25 represents the graphs of the amount of radiation energy released and failure load of andesite samples with different diameter.

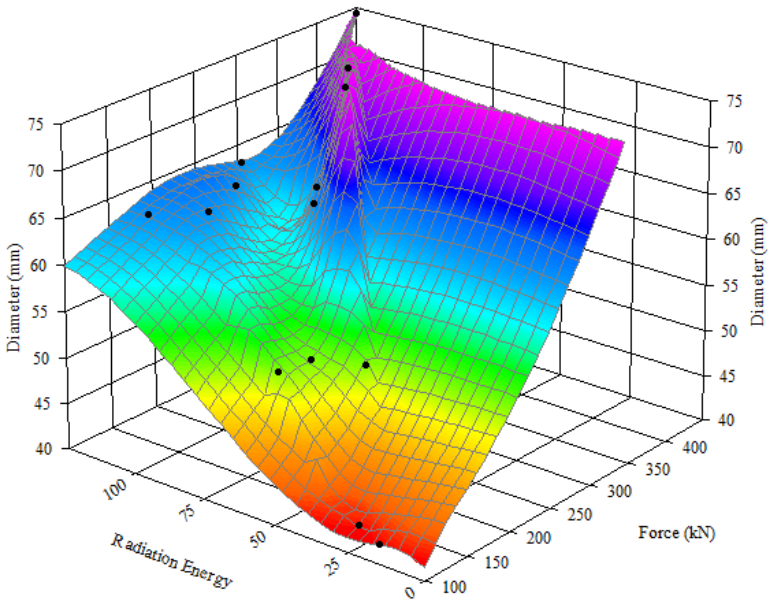

Figure 4.25. Radiation Energy-Failure Load graph of Andesite Samples with low temperature increase

Similar to the temperature increase behavior, released radiation energy with the increasing failure load follows a trend for this case. With increasing diameter of the samples, an increase in the amount of released radiation energy is observed. Nevertheless, investigation of the high temperature increase samples will lead to more accurate results. Table 4.20 shows the overall results of the andesite samples of different diameters with high temperature increase at the failure plane.

Table 4.20. *Average results of different size of Andesite samples with high temperature increase at the failure plane*

Sample Diameter (mm)	**Failure Load (kN)**	**Temperature Increase (°C)**	**Radiation Energy (kJ)**	**Radiation Energy (%)**
75	437.60	10.29	297.18	81.51
63	283.29	4.45	139.21	37.22
Average	334.73	6.40	191.87	51.98

According to Table 4.20, the temperature increase at the moment of failure for andesite samples with 75 mm diameter were 5.84 °C higher compared to the temperature readings taken from 63 mm diameter samples. In addition, it has been observed that the amount of radiation energy was 160 kJ higher than the amount of the radiation energy of 63 mm diameter samples. Hence, it can be said that there is a strong correlation between the increase in the failure load, temperature increase, and radiation energy. When the results are compared with the low temperature changing samples, it can be concluded that the results observed with high temperature change are more accurate. Since the temperature increase at the failure moment is a very sudden event, and the thermal camera might not capture the exact temperature increase at the failure. Therefore, the high temperature changes are considered as more accurate results and the analysis of these values can lead to more solid conclusions. Figure 4.26 represents the amount of the temperature change recorded for the andesite samples according to failure load values for each sample.

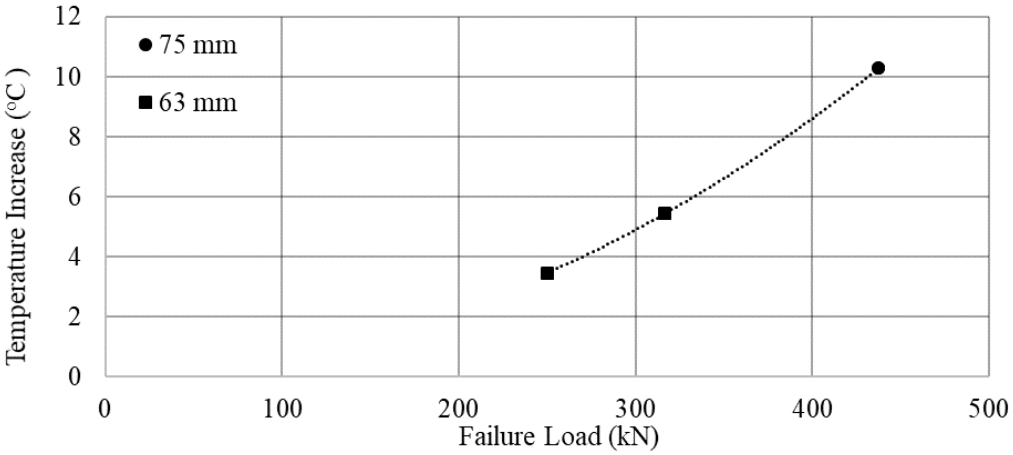

Figure 4.26. Temperature Increase- Failure Load graph of Andesite Samples with high temperature increase

According to Figure 4.26, there is a very strong relation between the temperature increase and the increase of the failure load of sample. With the increasing diameter size, both temperature at the failure moment and the failure load increased. Similarly, graphs of the amount of radiation energy released and failure load of andesite samples can be seen from Figure 4.27.

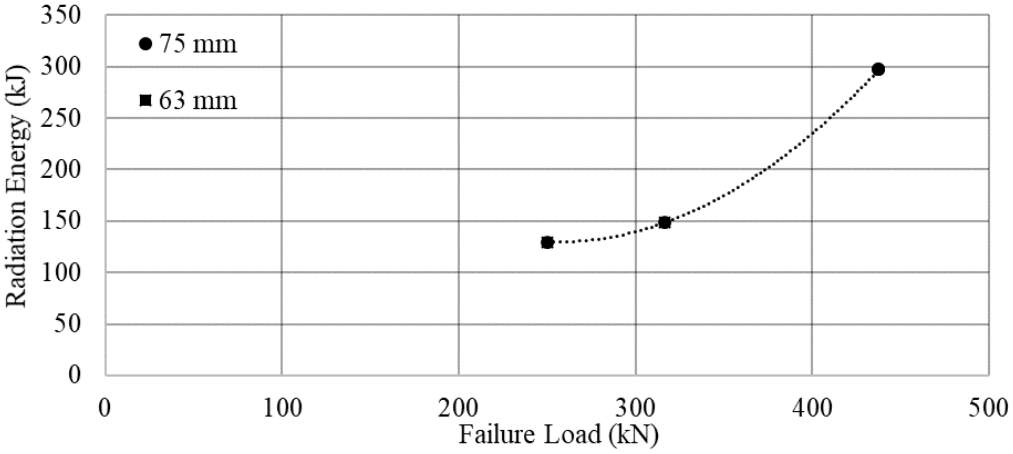

Figure 4.27. Radiation Energy- Failure Load graph of Andesite Samples with high temperature increase

Accordingly, same behavior for released radiation energy amount can be seen with the increase in the failure load. Hence, a relationship between failure load, temperature increases at the moment of failure and released energy exists for andesite samples.

Similar to the andesite samples, marble samples with 75 mm, 63 mm, 53 mm and 42 mm diameter were prepared for UCS tests performed at a displacement rate of 0.002 mm/s. On the contrary to the behavior of the andesite samples, the temperature monitored on the surface of marble specimens decreased during the test period. Table 4.21 shows the overall results of the marble samples of different diameters.

Table 4.21. *Average results for different sizes of marble samples*

Sample Diameter (mm)	**Failure Load (kN)**	**Temperature Decrease (°C)**	**Radiation Energy (kJ)**	**Radiation Energy (%)**
75	293.90	-	-	-
63	153.80	0.50	17.72	15.56
53	94.80	0.58	18.29	16.52
42	46.20	0.49	12.68	12.13
Average	147.20	0.53	16.23	14.74

According to Table 4.21, it was observed that the temperature decrease remained constant at about 0.5-0.6 °C regardless of the diameter of the marble specimen. Similarly, released radiation energy amount remained almost constant with the different diameters. Figure 4.28 shows the relationship between temperature decrease during the experiments and failure load of the marble sample with different diameter sizes.

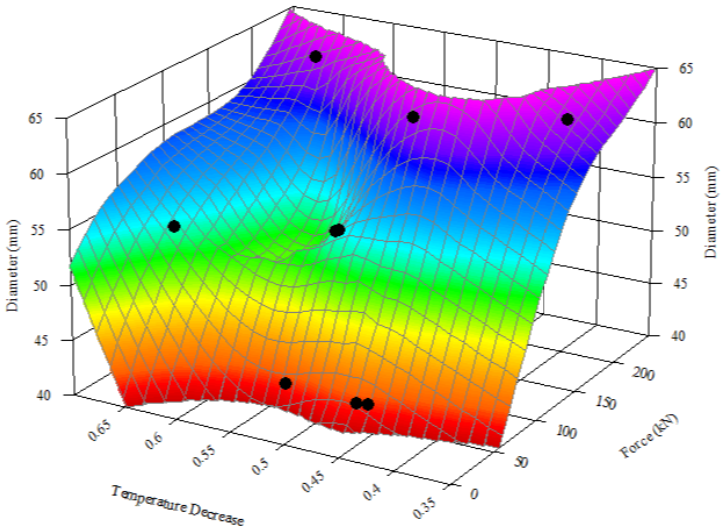

Figure 4.28. Temperature Decrease-Failure Load-Diameter Size of the Marble Samples

As it can be seen from Figure 4.28, as in Table 4.26, the temperature decrease remained constant at approximately 0.5 to 0.6 ℃ regardless of the diameter of the sample. More temperature decrease trend can be still observed with the increasing in the diameter sizes of the sample. Similarly, Figure 4.29 shows the relationship between the released energy amount and failure load of the different sizes of samples.

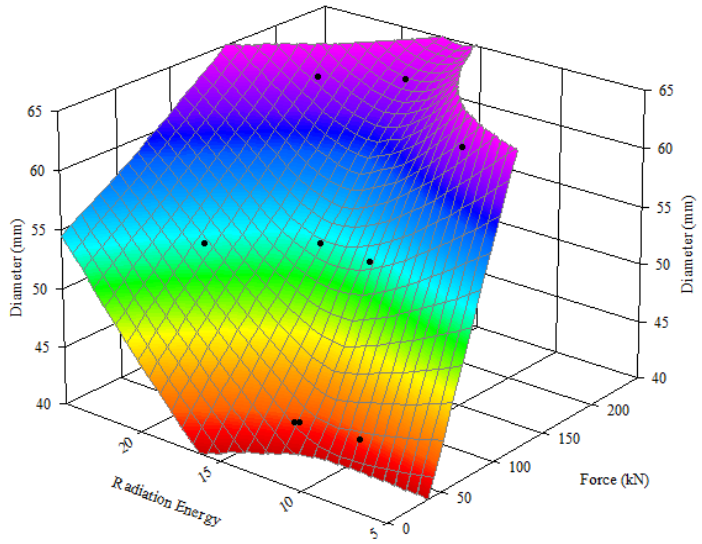

Figure 4.29. Radiation Energy- Failure Load- Diameter Size of the Marble Samples

According to Figure 4.29, there was a slight increase in the amount of radiation energy emission with increasing diameter of marble samples.

As a result, the study indicated that a relationship between failure load, temperature increases at the moment of failure and released energy exists. The increasing uniaxial compressive strength values had a similar trend to the temperature increase and the amount of radiation energy emitted.

CHAPTER 5

CONCLUSIONS AND RECOMMENDATIONS

In this study, the behavior of different types of rock samples as a result of UCS tests was investigated with the help of thermographic analysis. The failure behavior of same type of rocks was investigated by varying specimen diameters. Main findings of the study can be summarized as follows;

- For andesite type rock samples, results were investigated as two individual groups. According to results of the first group of the samples, which indicate low temperature change at the failure plane, there was no distinct relationship between the failure load and the temperature change. The reason for this is explained by the thermal camera not being able to capture the instantaneous temperature change by recording high speed images. Therefore, the andesite samples classified as the first group may provide preliminary information for the actual case. From the second group samples, which show high temperature increase at the failure plane, it was observed that larger diameter size together with greater failure load, ranging from 283 kN to 437 kN, is related with the increase of the temperature from 4.45 ℃ to 10.29 ℃ at the failure plane and the increase of the generated energy from 139 kJ to 297 kJ.
- For gneiss-schist type rock samples, the first group of samples which show low temperature change at the failure plane, average temperature change at the failure plane was found as 2.54 ℃ with a radiation energy of 46 kJ. From the second group of gneiss- schist samples, the temperature rise at the failure plane was increased from 4.94 ℃ to 18.27 ℃ with an increase in the failure load from 345 kN to 443 kN. Besides, the amount of energy produced was found to increase from 91 kJ to 288 kJ with increasing load.
- By considering the andesite and gneiss- schist types samples, respectively, there is a direct proportional relationship between the failure load and the

amount of temperature change recorded at the failure moment together with the released energy from the sample.

- For different types of rock samples with same sizes, the temperature increase monitored on the failure plane and released energy from the sample is higher for the samples with higher UCS values. For the andesite type of samples, the UCS, temperature increase, and the released energy amounts were 79 MPa, 4.45 ℃ and 139 kJ, respectively. For gneiss-schist type samples, the UCS, temperature increase and the energy release amounts were 99 MPa, 9.58 ℃ and 190 kJ. Therefore, it can be concluded that there is a directly proportional relationship between the UCS, the amount of temperature generated during the failure moment, and the energy released from the sample for different types of rock samples.
- According to the structure of the rock, a temperature decrease can be seen instead of a temperature increase in some rock types. For marble samples, it was found that the temperature decrease value remained constant between 0.5 ℃ and 0.6 ℃ regardless of the diameter size of the sample. However, it was observed that the amount of released energy was increased from 12 kJ to 17 kJ with the increase in the failure load from 46 kN to 153 kN.
- For samples taken from the blocks, porosity rates were obtained. Accordingly, andesite and marble samples have 5.65% and 0.59% effective porosity, respectively, and 20.97% and 10.79% total porosity rates, respectively These rates were compared with the released radiation energy amounts. Released radiation energy amounts were found as 107 kJ and 17 kJ for andesite and marble samples, respectively. As a result, it can be said that more porosity rates are also related to the estimated radiation energy of the samples.

In this study, the temperature increases at the moment of failure, and the amount of radiation energy for different type of rock samples was aimed to be determined. Most of the studies in the literature about this research topic investigate the temperature profile at the failure moment by using mid-wave high-speed thermal

cameras. In this study, a longwave length thermal camera, which has less sensitivity for images and record lower frame per second, was used. Hence, sometimes the temperature rise at the failure plane could not observed at the failure plane. In this context, longwave thermal cameras can give preliminary results for these types of studies. The failure behavior of rocks could be investigated in more detail by supporting these results with other available technologies such as acoustic emission, DIC and high-speed thermal cameras. The failure plane of the specimens could be detected at only one surface of the specimen due to a single thermal camera. However, sometimes failure plane occurred on the other surface of the specimens. In these cases, the failure surface could not be detected. Recording the other surface of the specimen with the help of a second thermal camera may be a solution to this problem. In addition to these suggestions, different type of rock specimens can be pre-heated to elevated temperatures. This will provide a wider temperature range that is recorded by the thermal camera. Therefore, temperature change at the failure moment might be observed more distincly. In this thesis study, loading rate was kept constant. For future studies, different loading rates and cyclic loading may be used to analyze the effect of the loading rate on the specimens.

REFERENCES

Akdag, S., Karakus, M., Taheri, A., Nguyen, G., & Manchao, H. (2018). Effects of Thermal Damage on Strain Burst Mechanism for Brittle Rocks Under True-Triaxial Loading Conditions. *Rock Mechanics and Rock Engineering, 51*(6), 1657-1682.

Almeida, L. R., Marques, E. G., Vargas , E., & Barros, W. T. (1998). Characterisation and utilisation of tensile strength and toughness of granitic and gneissic rocks of Rio de Janeiro City - a proposal for optimising rock blasting processes. *International Congress International Association for Engineering Geology and the Environment* (pp. 351-357). Vancouver: A.A. Balkema.

Antony, S. J., Olugbenga, A., Ozerkan, N., Marumoame, O., & Okeke, G. (2017). Sensing Temperature and Stress Distributions on Rock Samples under Mechanical. *15th Biennial ASCE Conference on Engineering, Science, Construction, and Operations in Challenging Environments.* Leeds: White Rose University Consortium.

Aydan, Ö., & Ulusay, R. (2013). Geomechanical Evaluation of Derinkuyu Antique Underground City and its Implications in Geoengineering. *Rock Mechanics and Rock Engineering, 46*(4), 731-754.

Aydan, Ö., Malistani, N., & Tokashiki, N. (2017). The Possibility of Infrared Camera Thermography for Assessing the Real-Time Stability of Tunnels Against Rockburst. *51st U.S. Rock Mechanics/Geomechanics Symposium.* San Fransisco: American Rock Mechanics Association.

Aydan, Ö., Manav, H., Yaoita, T., & Yagi, M. (2014). Multi-parameter Thermo-dynamic Response of Minerals and Rocks during Deformation and Fracturing.

ISRM International Symposium - 8th Asian Rock Mechanics Symposium. Sapporo: International Society for Rock Mechanics and Rock Engineering.

Bae Mountain Mining Corporation. (n.d.). *New Liberty Open Pit Litholofical Description.*

Baud, P., Wong, T.-f., & Zhu, W. (2014). Effects of porosity and crack density on the compressivestrength of rocks. *International Journal ofRock Mechanics & Mining Sciences, 67*, 202-211.

Belrhiti, Y., Dupre, J., Pop, O., Germaneau, A., Doumalin, P., Huger, M., & Chotard, T. (2017). Combination of Brazilian test and digital image correlation for mechanical characterization of refractory materials. *Journal of the European Ceramic Society*, *37*(5), 2285-2293.

Cai, C., Li, G., Huang, Z., Shen, Z., Tian, S., & Wei, J. (2014). Experimental study of the effect of liquid nitrogen cooling on rock pore structure. *Journal of Natural Gas Science and Engineering*, 507-517.

Cai, M., & Kaiser, P. K. (2005). Assessment of excavation damaged zone using a micromechanics model. *Tunnelling and Underground Space Technology*, *20*(4), 301-310.

Cermak, V., & Rybach, L. (1982). Thermal properties: Thermal conductivity and specific heat of minerals and rocks. In M. Beblo, *Geophysics- Physical Properties of Rocks* (pp. 305-343). Springer.

Dearman, W. R., Baynes, F. J., & Irfan, T. Y. (1978). Engineering grading of weathered granite. *Engineering Geology, 12*, 345-374.

Deb, D., & Verma, A. K. (2016). *Fundamentals and Applications of Rock Mechanics.* New Delhi: PHI Learning.

Di Benedetto, C., Cappeletti, P., Favaro, M., Graziano, S. F., Langella, A., Calcaterra, D., & Colella, A. (2015). Porosity as key factor in the durability of two

historical building stones:Neapolitan Yellow Tuff and Vicenza Stone. *Engineering Geology, 193*, 310-319.

Dunn, D. E., LaFountain, L. J., & Jackson, R. E. (1973). Porosity Dependance and Mechanism of Brittle Fracture in Sandstone. *Journal of Geophysical Research, 78*(14), 2403-2417.

Engelder, T., & Plumb, R. (1984). Changes in in situ ultrasonic properties of rock on strain relaxation. *International Journal of Rock Mechanics and Mining Sciences & Geomechanics Abstracts, 21*(2), 75-82.

Fematek. (2018). *Termal Teknoloji*. Retrieved November 11, 2018, from Fematek: http://fat.fematek.com/tr/fematek-askeri-goruntuleme-teknolojileri/termal-teknoloji/

Fitzner, B. (1994). Volcanic tuffs-the description and quantitative recording of their weathered state. *Lavas and volcanic tuffs: preprints of the contributions to the international meeting*, (pp. 125-139). Chile.

Ghabraie, B., Ren, G., Smith, J., & Holden, L. (2015). Application of 3D laser scanner, optical transducers and digital image processing techniques in physical modelling of mining- related strata movement. *Internation Journal of Rock Mechanics & Mining Sciences, 80*, 219-230.

Gong, W. L., Wang, J., Gong, Y. X., & Guo, P. Y. (2012). Thermography analysis of a roadway excavation experiment in 60 inclined. *International Journal of Rock Mechanics and Mining Sciences, 60*, 134-147.

Gong, W., Peng, Y., Sun, X., He, M., Zhao, S., Chen, H., & Xie, T. (2015). Enhancement of low-contrast thermograms for detecting the stressed tunnel in horizontally stratified rocks. *International Journal of Rock Mechanics and Mining Sciences, 74*, 69-80.

He, M., Sousa, R., Miranda, T., & Zhu, G. (2015). Rockburst laboratory tests database-Application of data mining techniques. *Engineering Geology, 185*, 116-130.

Hedley, D. G. (1992). *Rockburst handbook for Ontario hardrock mines.* Ontario Mining Association.

Kaiser, P. K., MacCreath, D. R., & Tannant, D. D. (1996). *Canadian rockburst support handbook: prepared for sponsor of the Canadian rockburst resarch program 1990-1995.* Geomechanics Research Centre.

Li, Z., Yin, S., Niu, Y., Cheng, F., Liu, S., Kong, Y., . . . Wei, Y. (2018). Experimental study on the infrared thermal imaging of a coal fracture under the coupled effects of stress and gas. *Journal of Natural Gas Science and Engineering, 55*, 444-451.

Liu, S., Wu, L., & Wu, Y. (2006). Infrared radiation of rock at failure. *International Journal of Rock Mechanics and Mining Sciences, 43*, 972-979.

Lou, Q., & He, X. (2018). Experimental study on infrared radiation temperature field of concrete under uniaxial compression. *Infrared Physics and Technology, 90*, 20-30.

McWilliams, J. (1966). The role of microstructure in the physical properties of rock. In *Testing techniques for rock mechanics.*

Mineo, S., & Pappalardo, G. (2016). The Use of Infrared Thermography for Porosity Assessment of Intact Rock. *Rock Mechanics and Rock Engineering, 49*(8), 3027-3039.

Palchik, V., & Hatzor, Y. H. (2004). *The Influence of Porosity on Tensile and Compressive Strength of Porous Chalks.* Beer- Sheva: Rock Mechanics and Rock Engineering.

Pappalardo, G., Mineo, S., Zampelli, S. P., Cubito, A., & Calcaterra, D. (2016). InfraRed Thermography proposed for the estimation of the Cooling Rate Index in the remote survey of rock masses. *International Journal of Rock Mechanics & Mining Sciences*, 182-196.

Patel, S., & Martin, C. D. (2018). Application of Flattened Brazilian Test to Investigate Rocks Under Confined Extension. *Rock Mechanics and Rock Engineering, 51*(12), 3719-3736.

Qin, L., Zhai, C., Liu, S., & Xu, J. (2018). Infrared thermal image and heat transfer characteristics of coal injected with liquid nitrogen under triaxial loading for coalbed methane recovery. *International Journal of Heat and Mass Transfer, 118*, 1231-1242.

Rates of Heat Transfer. (2019). Retrieved from https://www.physicsclassroom.com: https://www.physicsclassroom.com/class/thermalP/Lesson-1/Rates-of-Heat-Transfer

Read, R. S. (2004). 20 years of excavation response studies at AECL's Underground Research Laboratory. *International Journal of Rock Mechanics and Mining Sciences, 41*(8), 1251-1275.

Roylance, D. (2001). *Stress-strain curves.* Cambridge: Massachusetts Institute of Technology study.

Salami, Y., Dana, C., & Hicher, P. Y. (2017). Infrared thermography of rock fracture. *Géotechnique Letters, 7*(1), 1-5.

Singh, B., & Goel, R. K. (2012). *Engineering Rock Mass Classification.* Elsevier.

Sousa, L. M., Suarez del Rio, L. M., Calleja, L., Ruiz de Argandona, V. G., & Rodriguez Rey, A. (2005). Influence of microfractures and porosity on the physico-mechanical properties and weathering of ornamental granites. *Engineering Geology, 77*(1-2), 153-168.

Sun, X., Chen, F., Miao, C., Song, P., Li, G., Zhao, C., & Xia, X. (2018). Physical modeling of deformation failure mechanism of surrounding rocks for the deep-buried tunnel in soft rock strata during the excavation. *Tunnelling and Underground Space Technology, 74*, 247-261.

Sun, X., Xu, H., He , M., & Zhang, F. (2017). Experimental investigation of the occurrence of rockburst in a rock specimen through infrared thermography and acoustic emission. *International Journal of Rock Mechanics and Mining Sciences, 93*, 250-259.

Sun, X.-m., Chen, F., He, M.-c., Gong, W.-l., Xu, H.-c., & Lu, H. (2017). Physical modeling of floor heave for the deep-buried roadway excavated in ten degree inclined strata using infrared thermal imaging technology. *Tunnelling and Underground Space Technology, 63*, 228-243.

Tan, Z. H., Tang, C. A., & Zhu, W. (2007). Infrared Thermal Image Study on Failure of Granite with Hole. *Key Engineering Materials*, 353-358.

Tuğrul, A., & Gürpinar, O. (1997). A proposed weathering classification for basalt and their engineering properties (Turkey). *Bulletin of Engineering Geology and the Environment, 55*(1), 139-149.

Ulusay , R., Aydan, Ö., Gerçek, H., Hindistan, M. A., & Tuncay, E. (2016). *Rock Mechanics and Rock Engineering: From the Past to the Future.* CRC Press.

Ulusay, R., & Hudson, J. A. (2007). *The Complete ISRM Suggested Methods For Rock Characterization, Testing and Monitoring.* Ankara: ISRM Turkish National Group.

Wang, C., Lu, Z., Liu, L., Chuai, X., & Lu, H. (2016). Predicting points of the infrared precursor for limestone failure under uniaxial compression. *International Journal of Rock Mechanics and Mining Sciences, 88*(10), 34-43.

Wang, S., Li , D., Li, C., Zhang, C., & Zhang, Y. (2018). Thermal radiation characteristics of stress evolution of a circular tunnel excavation under different confining pressures. *Tunneling and Underground Space Technology, 78*, 76-83.

Winkler, E. (1997). *Stone in Architecture: Properties, Durability.* Berlin: Springer-Verlag.

Wu, L., Liu, S., Wu, Y., & Wang, C. (2006). Precursors for rock fracturing and failure—Part I: IRR image abnormalities. *International Journal of Rock Mechanics and Mining Sciences, 43*(3), 473-482.

Yin, T., Li, X., Cao, W., & Xia, K. (2015). Effects of Thermal Treatment on Tensile Strength of Laurentian Granite Using Brazilian Test. *Rock Mechanics and Rock Engineering, 48*(6), 2213-2223.

Young, R. P., & Collins, D. S. (2001). Seismic studies of rock fracture at the Underground Research Laboratory, Canada. *International Journal of Rock Mechanics and Mining Sciences, 38*(6), 787-799.

Zhang, Q. B., & Zhao, J. (2014). A Review of Dynamic Experimental Techniques and Mechanical Behaviour of Rock Materials. *Rock Mechanics and Rock Engineering, 47*(4), 1411-1478.

Zhao, Z.-H., & Xie, H.-P. (2008). Energy transfer and energy dissipation in rock deformation and fracture. *Journal of Sichuan University*, 26-31.

APPENDICES

A. Test Photos of the Specimens

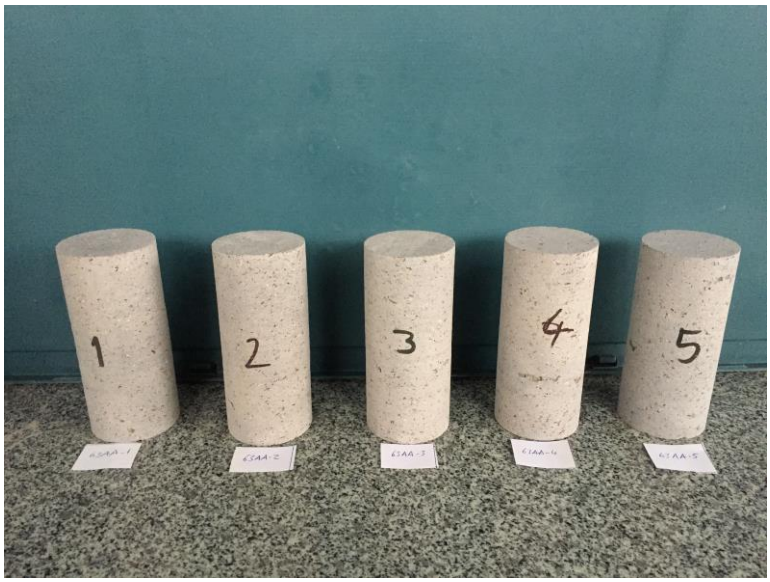

Figure A.1. Pre-test image of some of the 63 mm diameter andesite samples (63AA1 to 63 AA5)

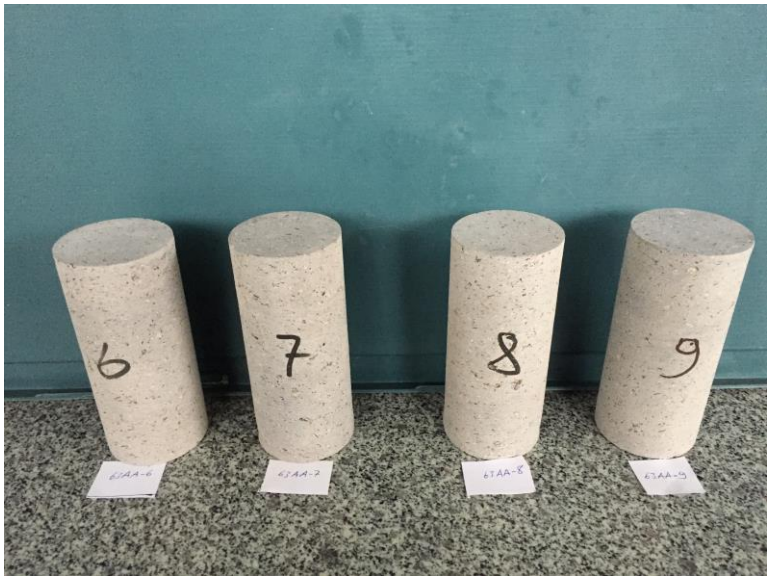

Figure A.2. Pre-test image of some of the 63 mm diameter andesite samples (63AA6 to 63 AA9)

Figure A.3. Post-test image of some of the 63 mm diameter andesite samples (63AA1 to 63 AA5)

Figure A.4. Post-test image of some of the 63 mm diameter andesite samples (63AA6 to 63 AA9)

Figure A.5. Pre-test image of some of the 63 mm diameter marble samples (63MM1 to 63 MM4)

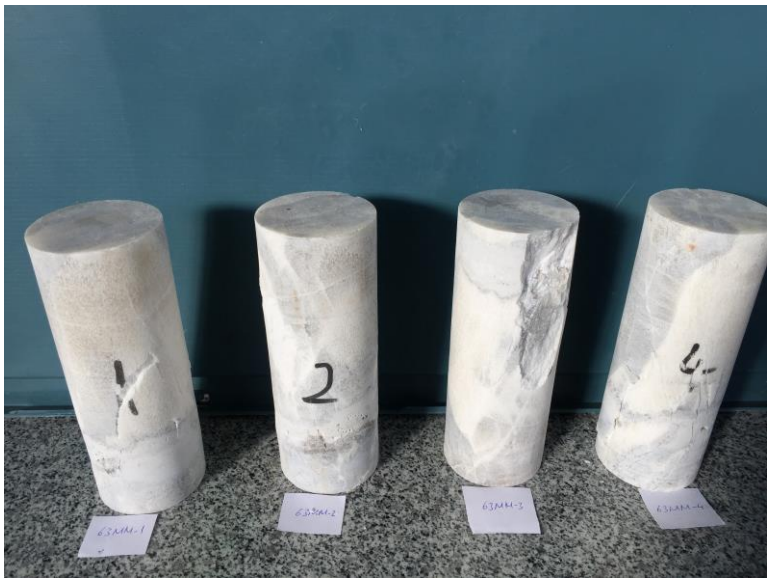

Figure A.6. Post-test image of some of the 63 mm diameter marble samples (63MM1 to 63 MM4)

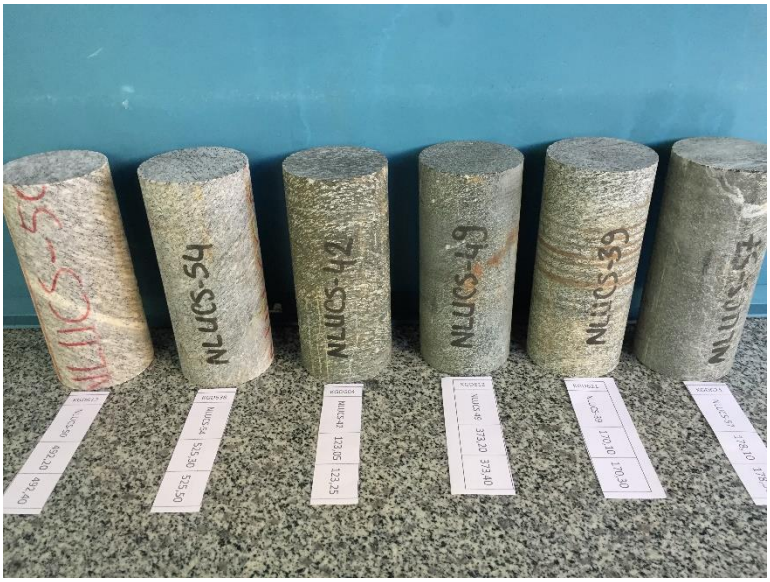

Figure A.7. Pre-test image of some of the gneiss-schist samples

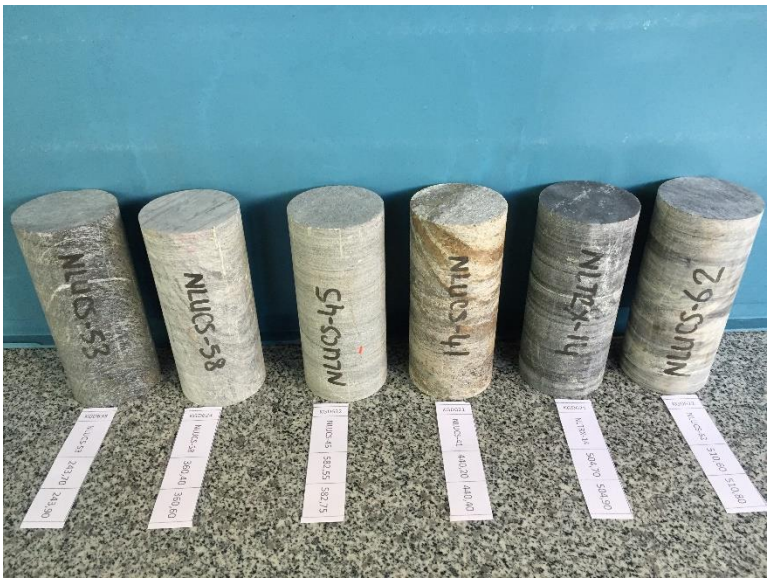

Figure A.8. Pre-test image of some of the gneiss-schist samples

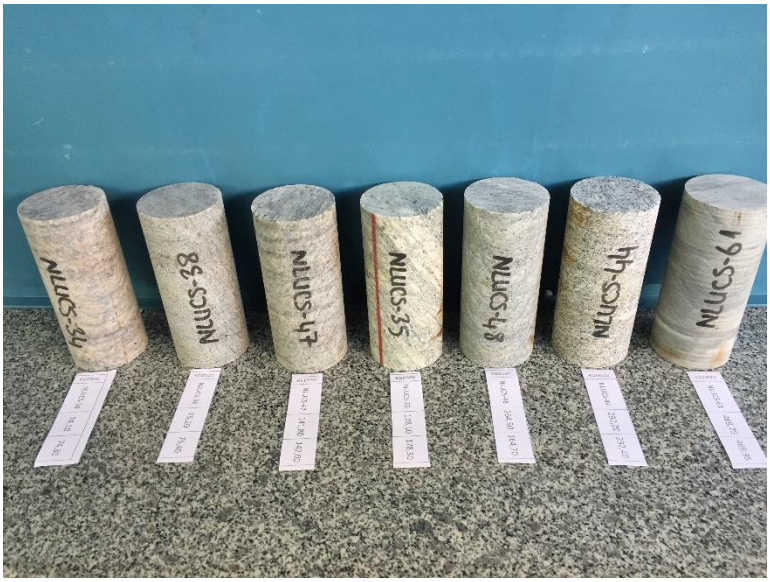

Figure A.9. Pre-test image of some of the gneiss-schist samples

Figure A.10. Post-test image of some of the gneiss-schist samples

Figure A.11. Post-test image of some of the gneiss-schist samples

Figure A.12. Post-test image of some of the gneiss-schist samples

B. Thermal Image of the Specimens

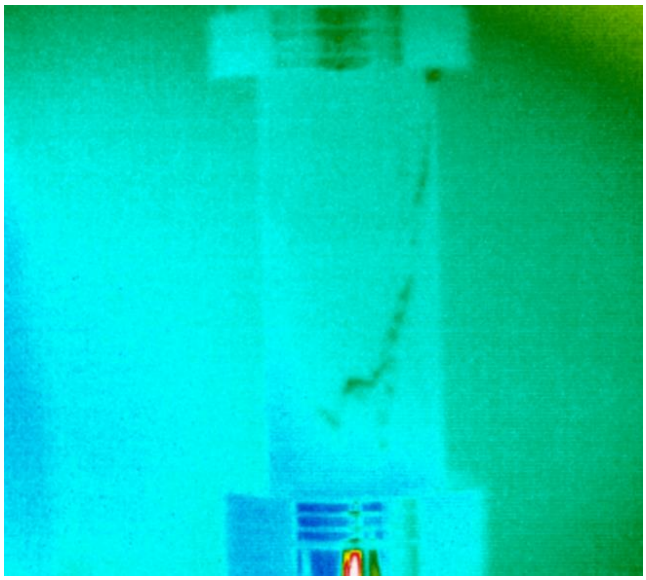

Figure B.1. Failure plane detection of the 75A-3 sample by the thermal camera

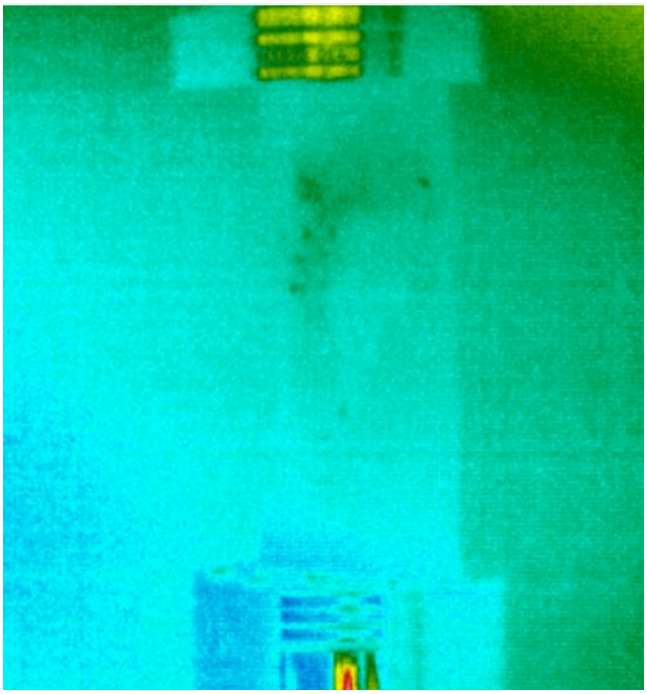

Figure B.2. Failure plane detection of the 75A-4 sample by the thermal camera

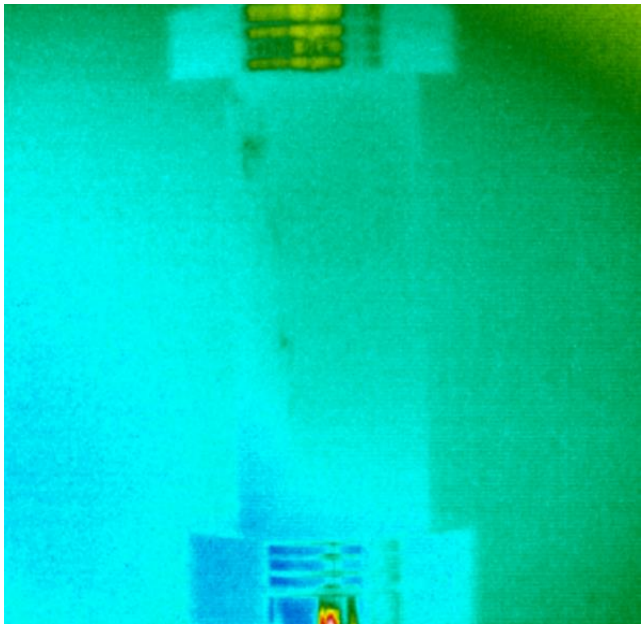

Figure B.3. Failure plane detection of the 75A-5 sample by the thermal camera

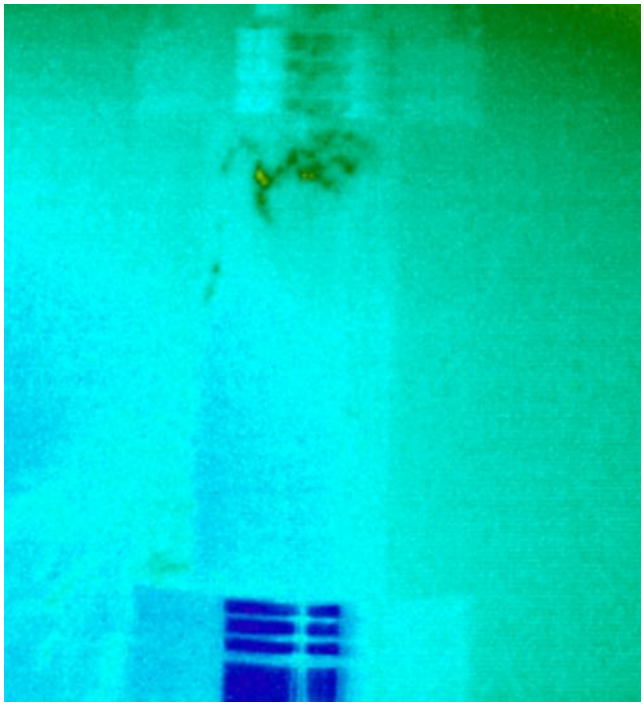

Figure B.4. Failure plane detection of the 63A-1 sample by the thermal camera

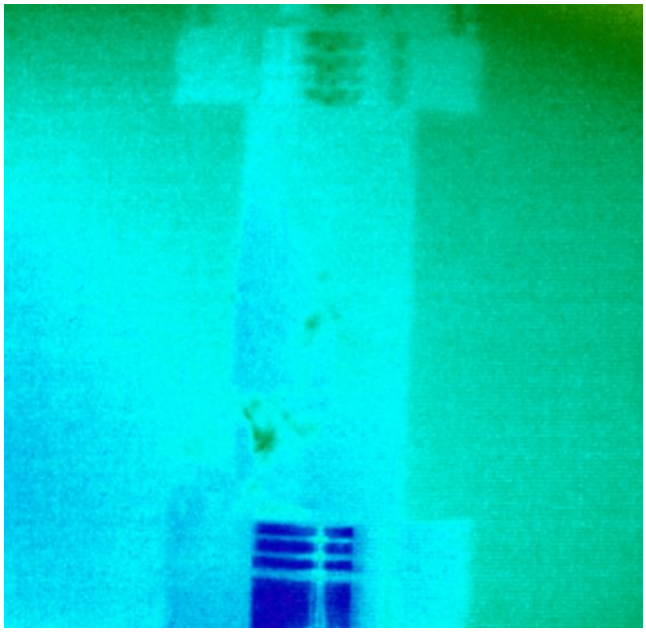

Figure B.5. Failure plane detection of the 63A-2 sample by the thermal camera

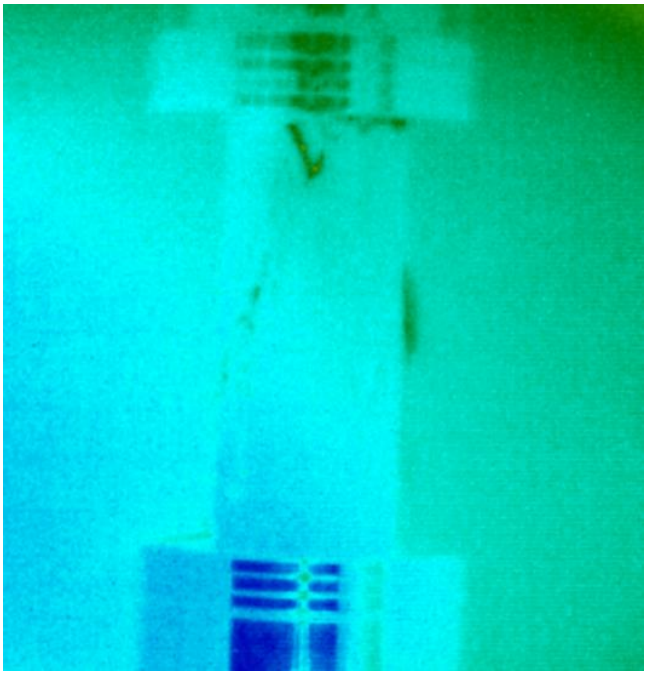

Figure B.6. Failure plane detection of the 63A-5 sample by the thermal camera

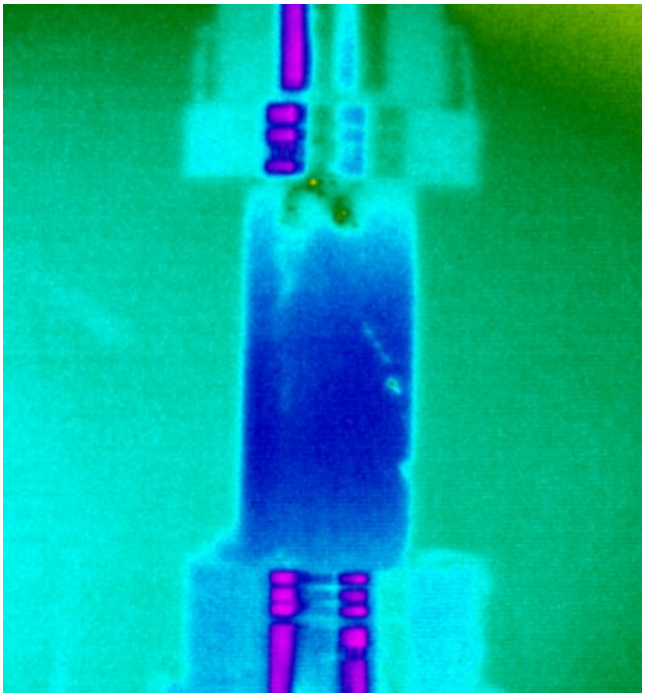

Figure B.7. Failure plane detection of the 63AA-2 sample by the thermal camera

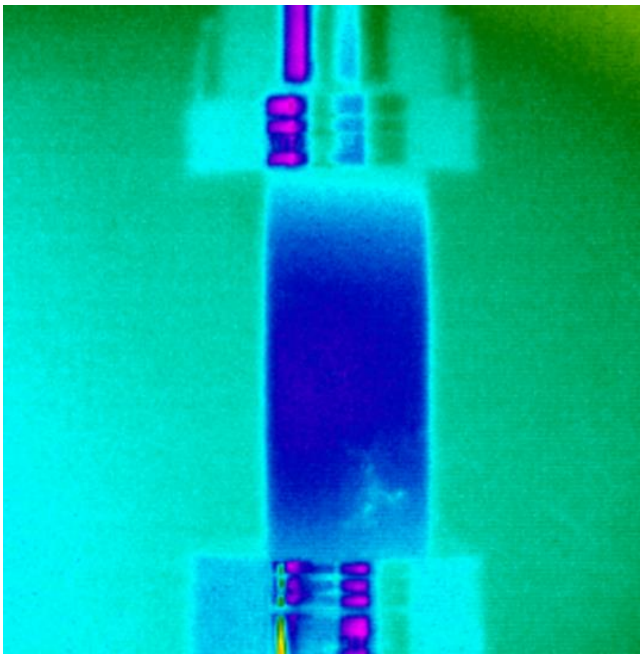

Figure B.8. Failure plane detection of the 63AA-4 sample by the thermal camera

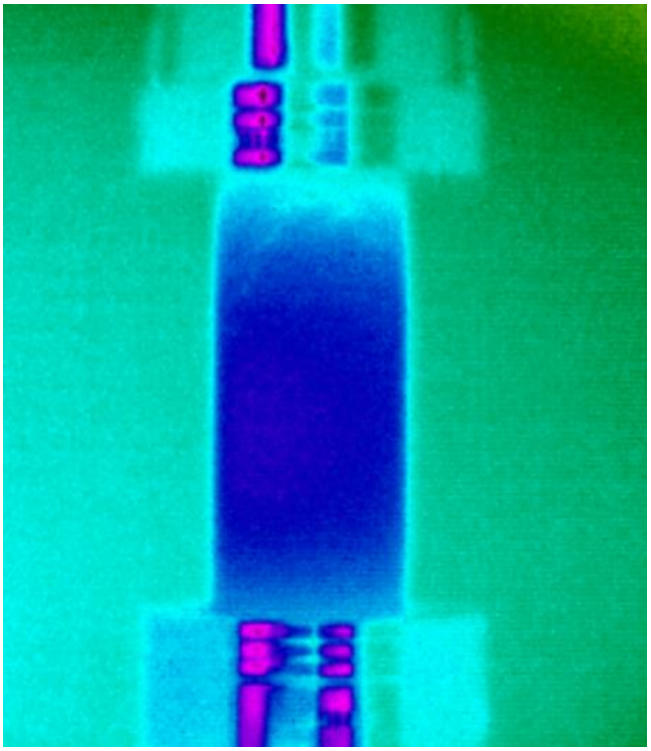

Figure B.9. Failure plane detection of the 63AA-6 sample by the thermal camera

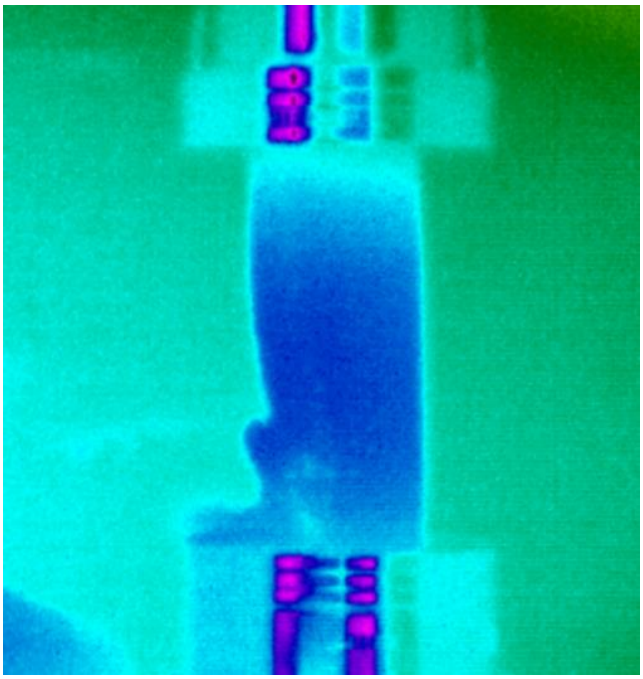

Figure B.10. Failure plane detection of the 63AA-9 sample by the thermal camera

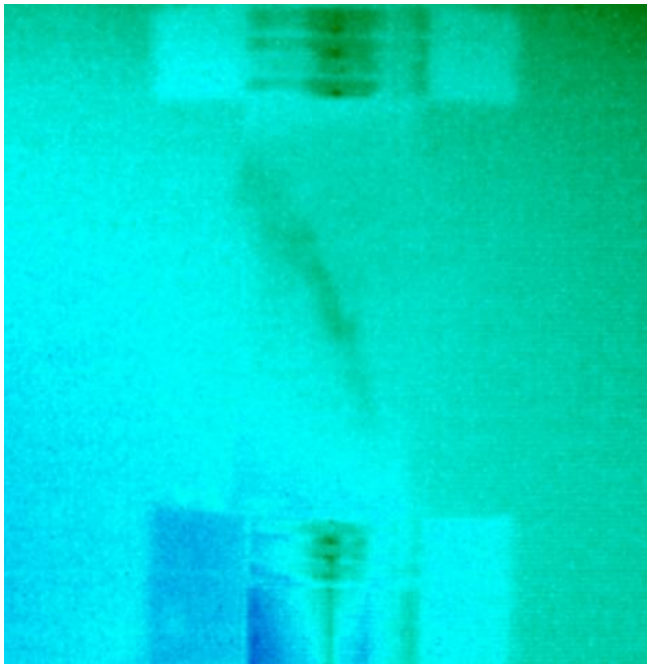

Figure B.11. Failure plane detection of the 53A-4 sample by the thermal camera

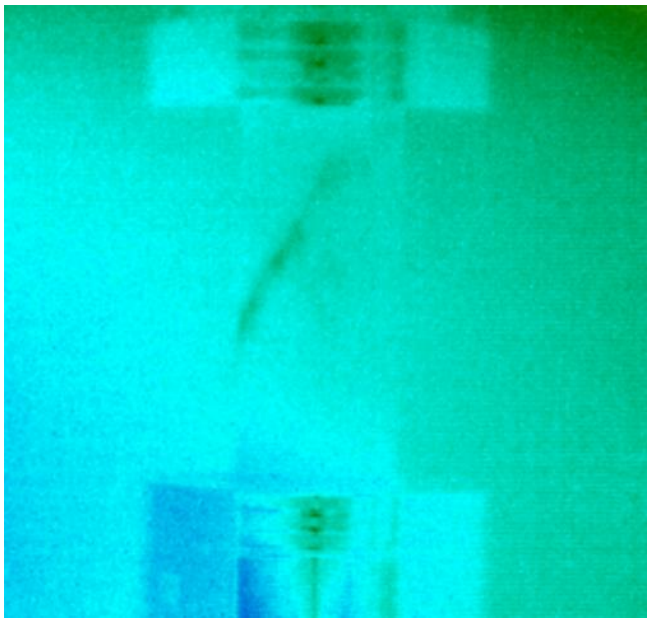

Figure B.12. Failure plane detection of the 53A-5 sample by the thermal camera

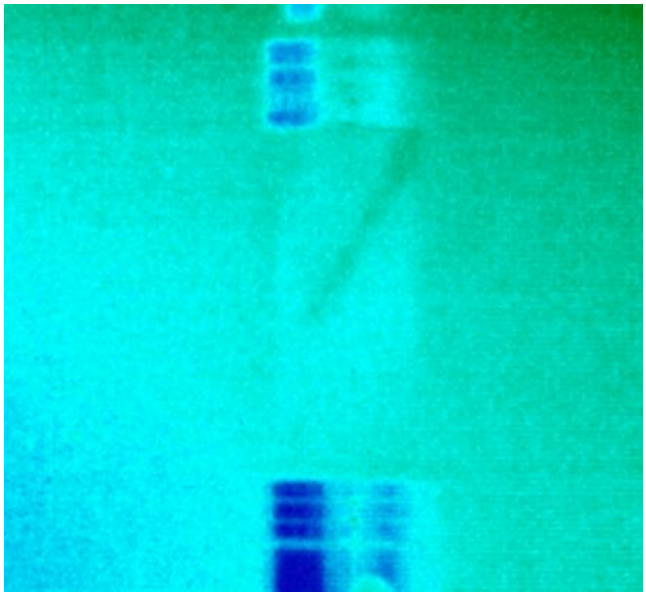

Figure B.13. Failure plane detection of the 42A-2 sample by the thermal camera

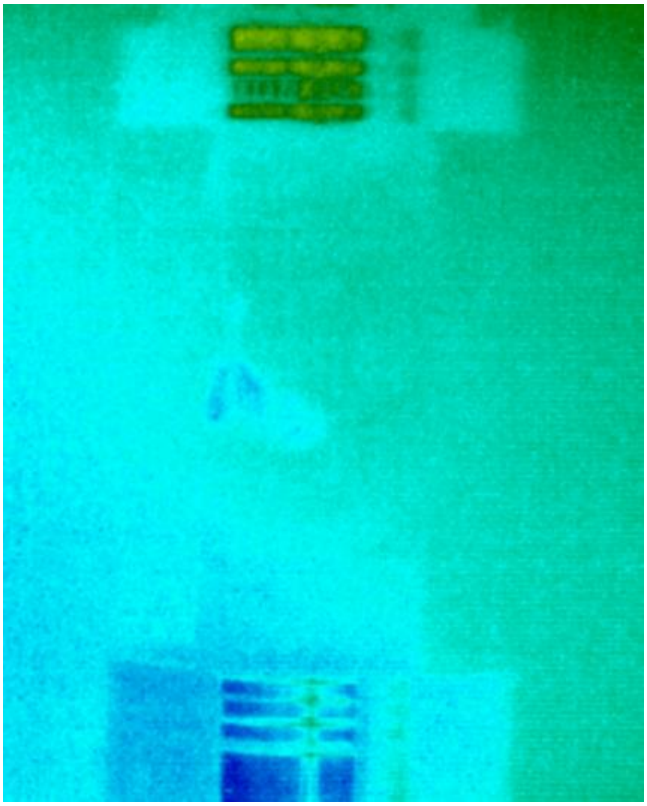

Figure B.14. Failure plane detection of the 63M-2 sample by the thermal camera

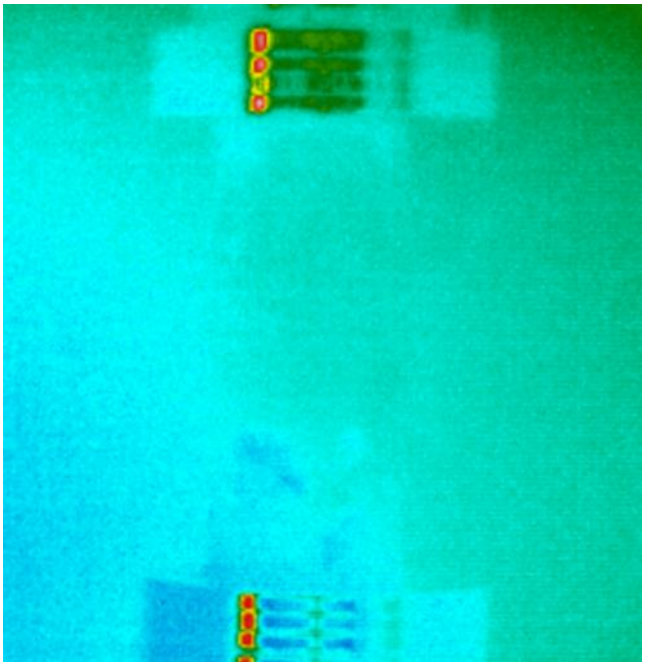

Figure B.15. Failure plane detection of the 63M-4 sample by the thermal camera

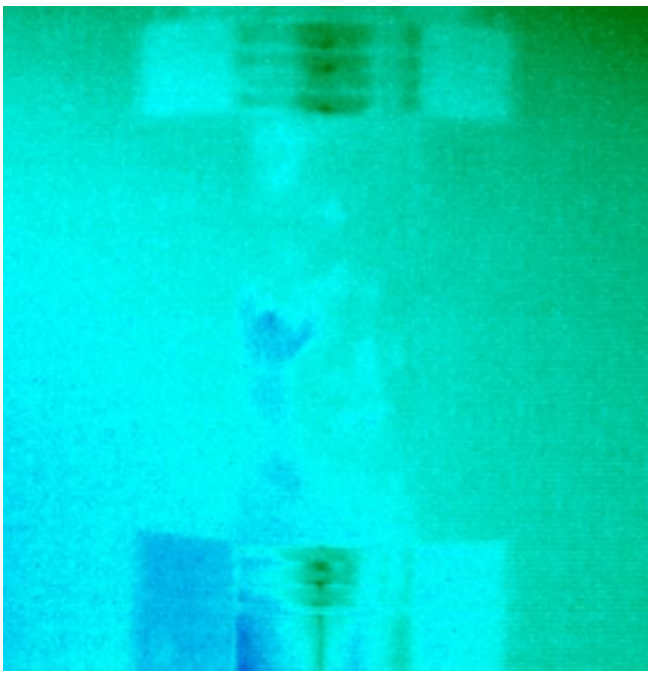

Figure B.16. Failure plane detection of the 53M-1 sample by the thermal camera

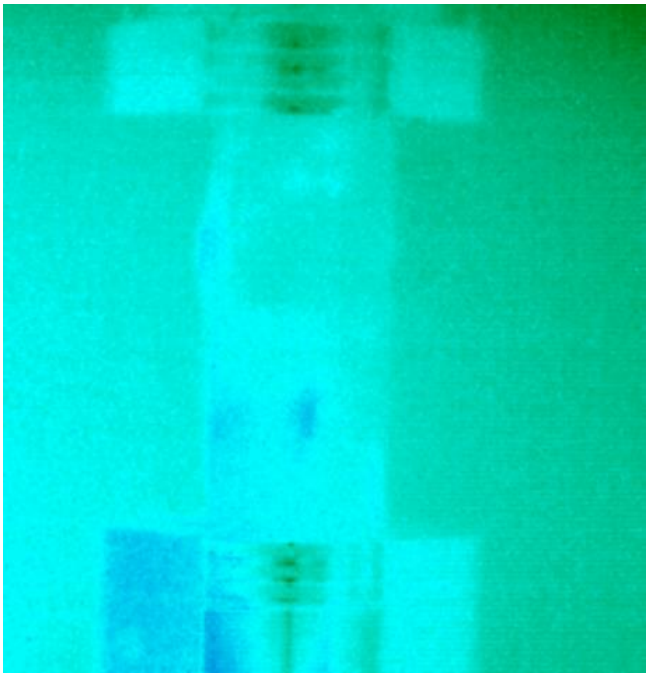

Figure B.17. Failure plane detection of the 53M-4 sample by the thermal camera

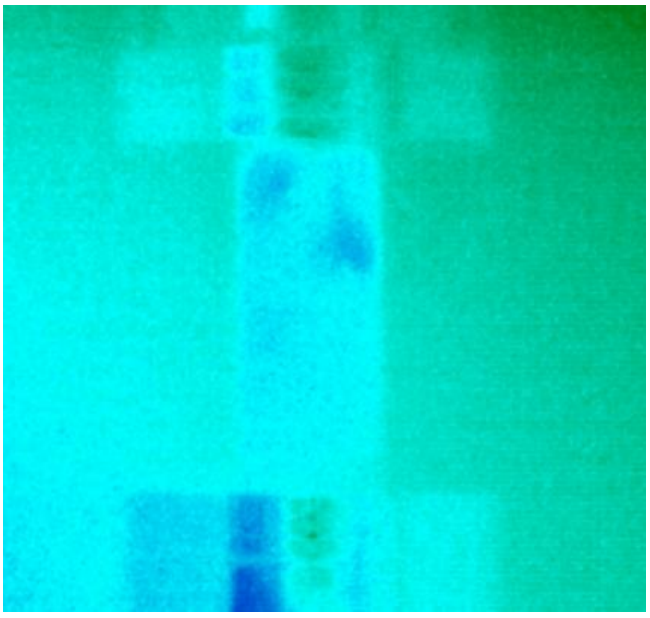

Figure B.18. Failure plane detection of the 42M-2 sample by the thermal camera

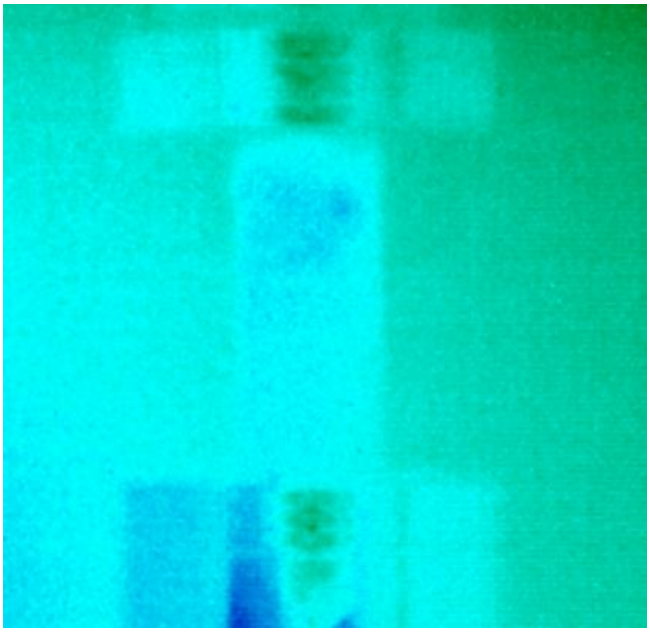

Figure B.19. Failure plane detection of the 42M-5 sample by the thermal camera

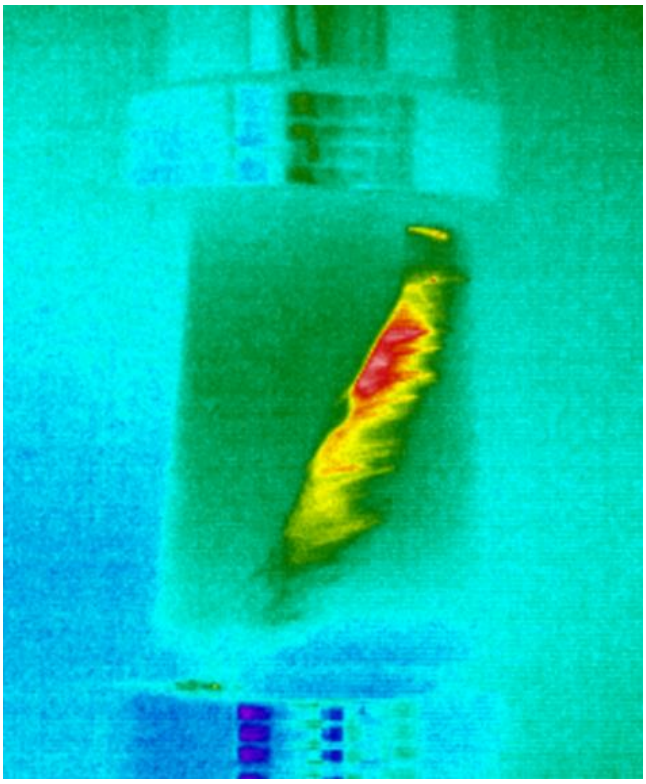

Figure B.20. Failure plane detection of the NLUCS-37 sample by the thermal camera

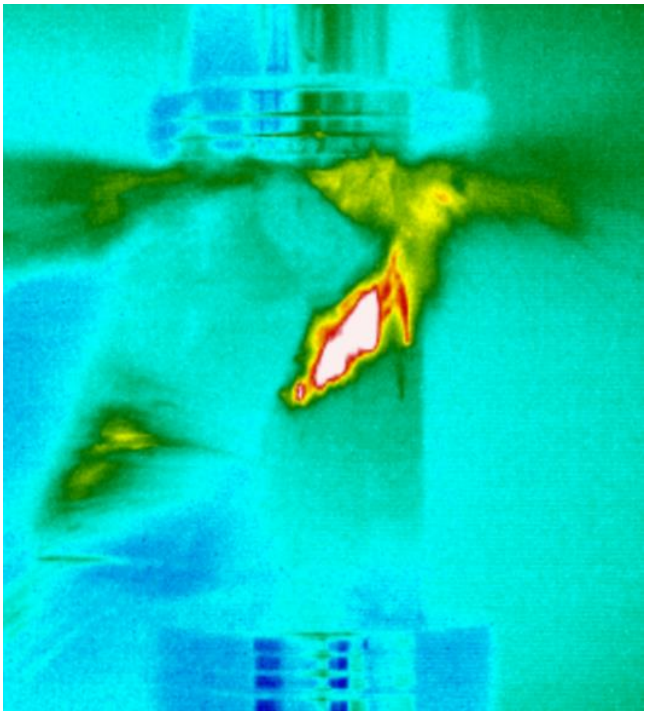

Figure B.21. Failure plane detection of the NLUCS-40 sample by the thermal camera

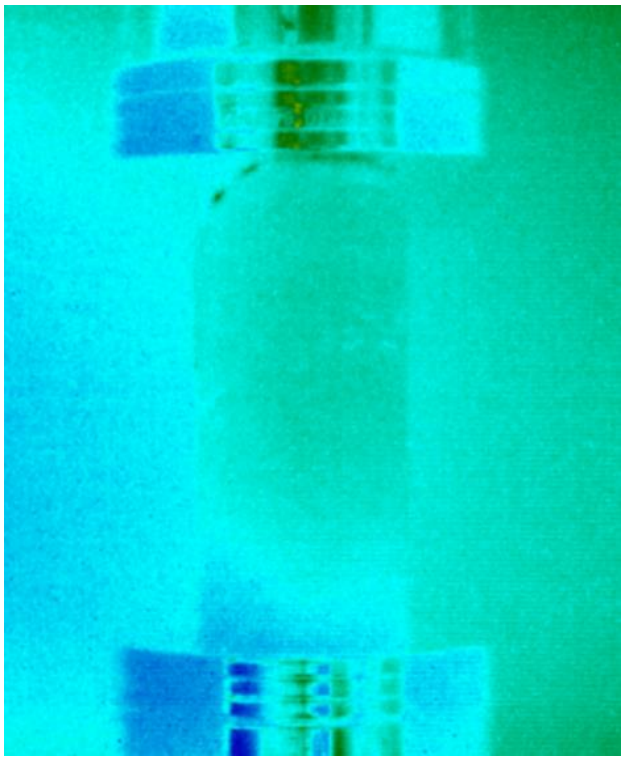

Figure B.22. Failure plane detection of the NLUCS-41 sample by the thermal camera

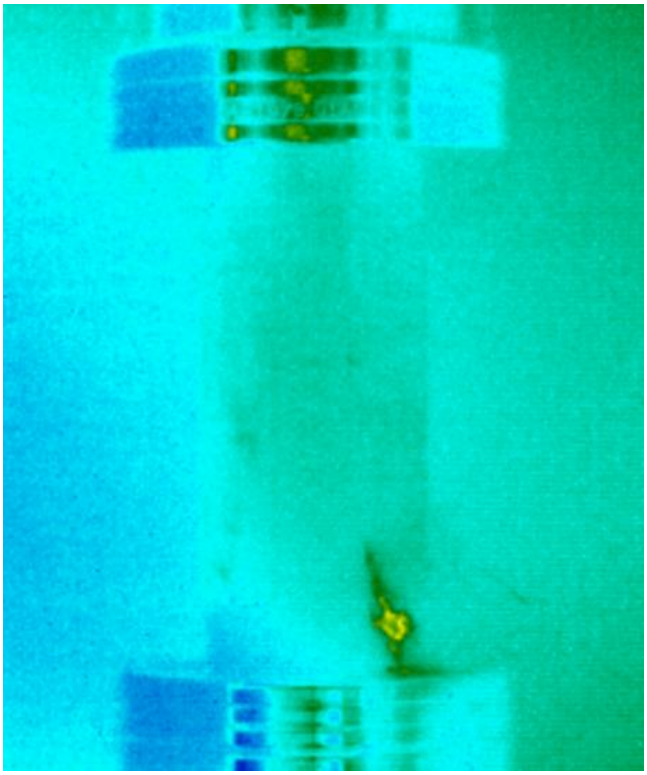

Figure B.23. Failure plane detection of the NLUCS-47 sample by the thermal camera

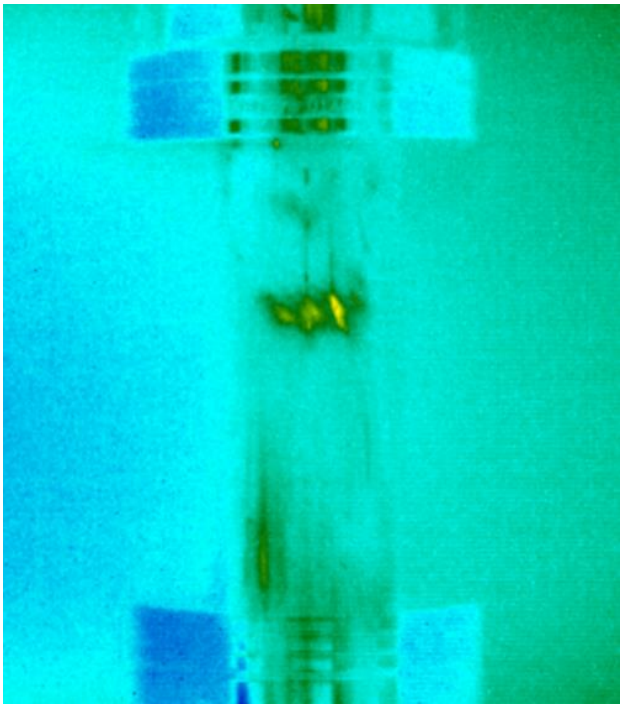

Figure B.24. Failure plane detection of the NLUCS-48 sample by the thermal camera

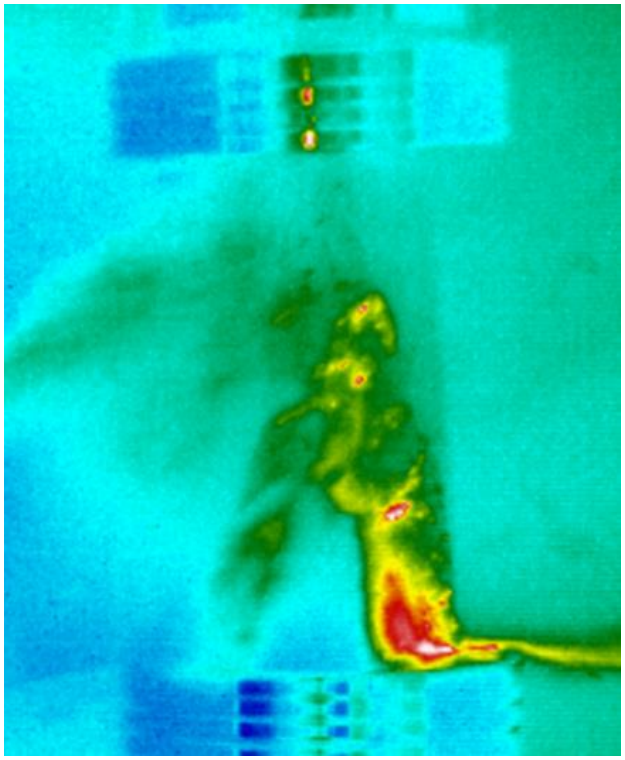

Figure B.25. Failure plane detection of the NLUCS-49 sample by the thermal camera

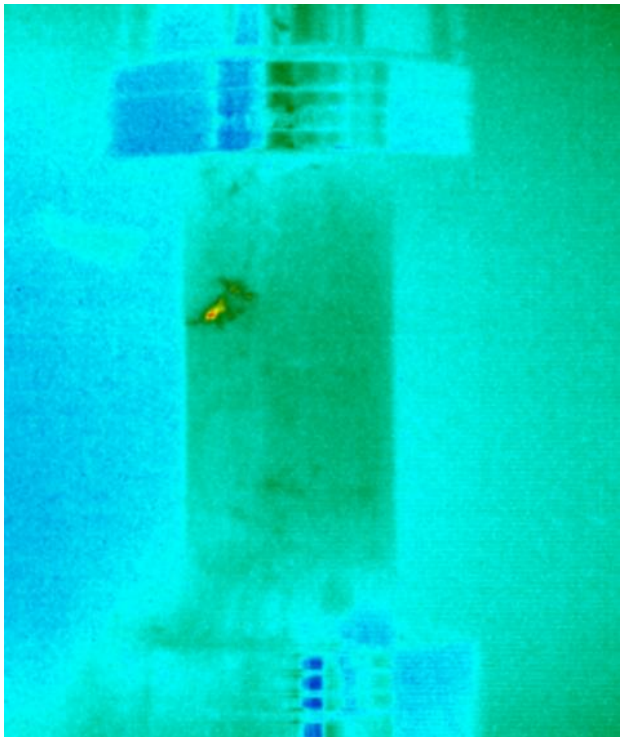

Figure B.26. Failure plane detection of the NLUCS-55 sample by the thermal camera

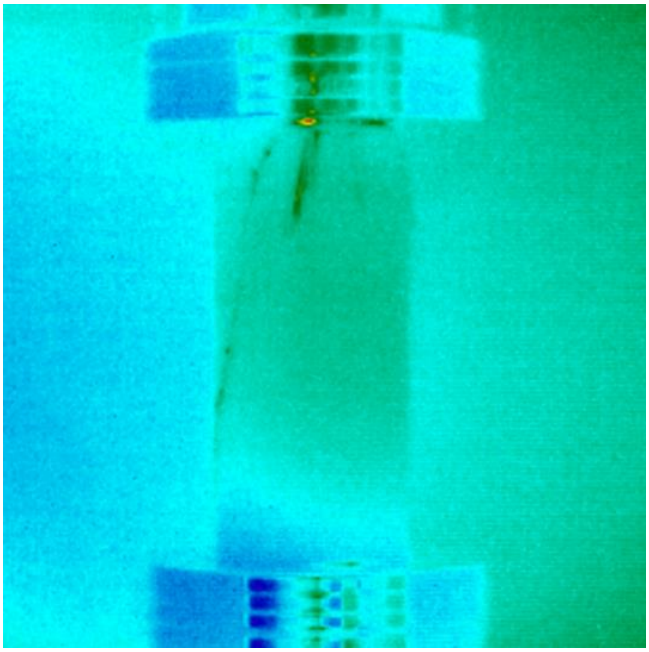

Figure B.27. Failure plane detection of the NLUCS-57 sample by the thermal camera

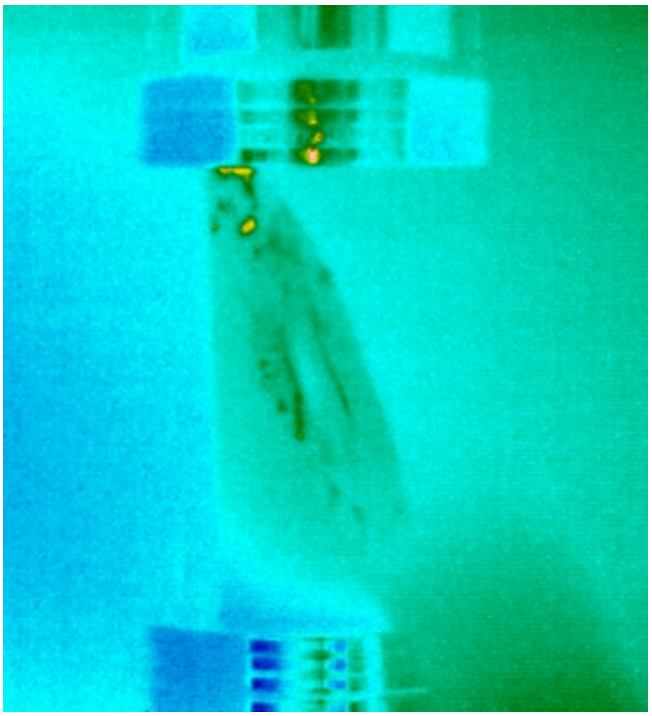

Figure B.28. Failure plane detection of the NLUCS-58 sample by the thermal camera

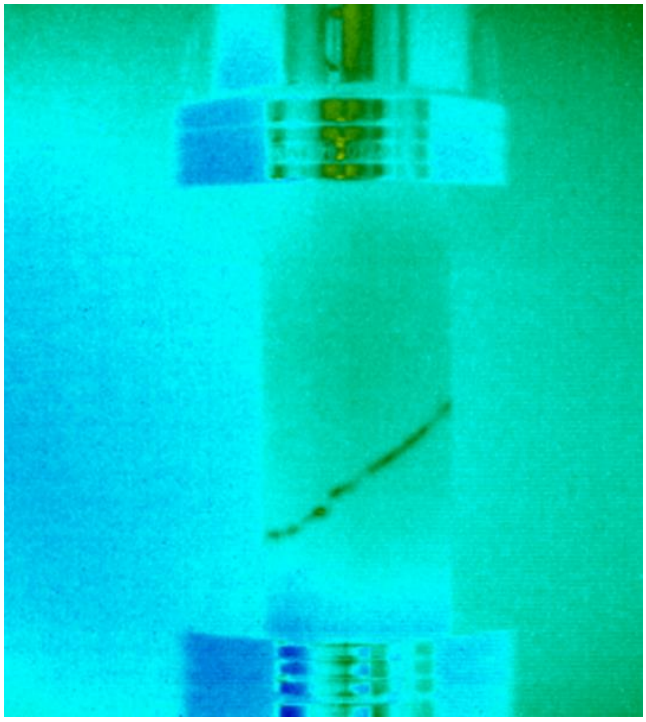

Figure B.29. Failure plane detection of the NLUCS-62 sample by the thermal camera

C. Force- Temperature Change- Time Graphs of the Specimens

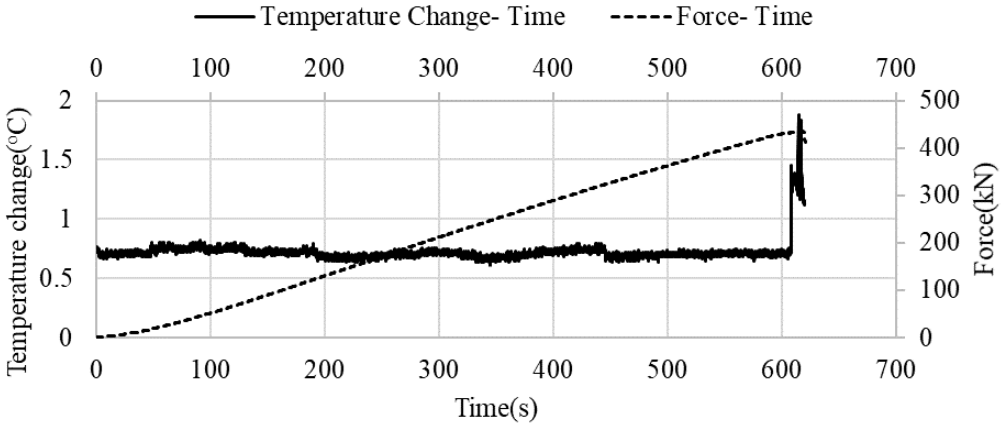

Figure C.1. Temperature change- Force- Time graph of the 75A-3 sample

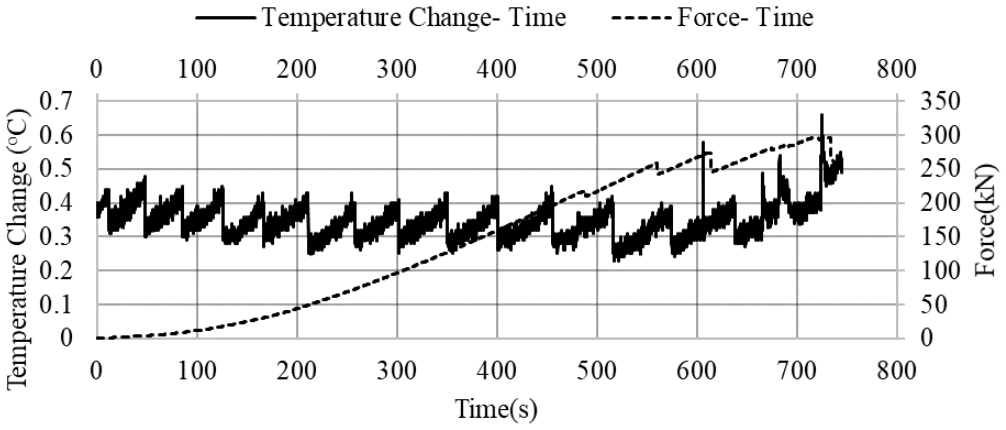

Figure C.2. Temperature change- Force- Time graph of the 75A-4 sample

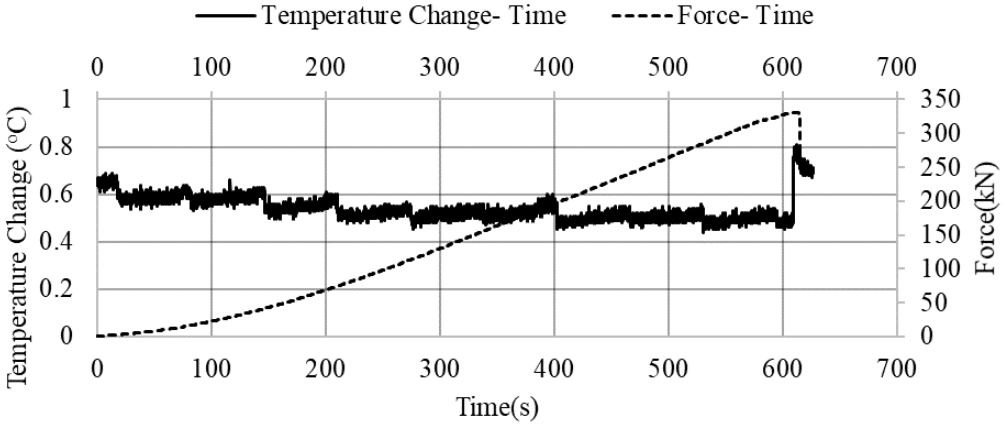

Figure C.3. Temperature change- Force- Time graph of the 75A-5 sample

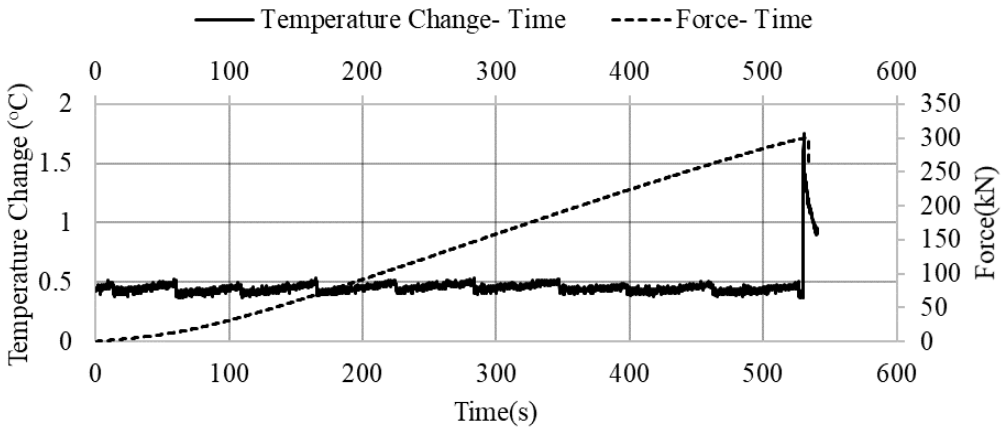

Figure C.4. Temperature change- Force- Time graph of the 63A-1 sample

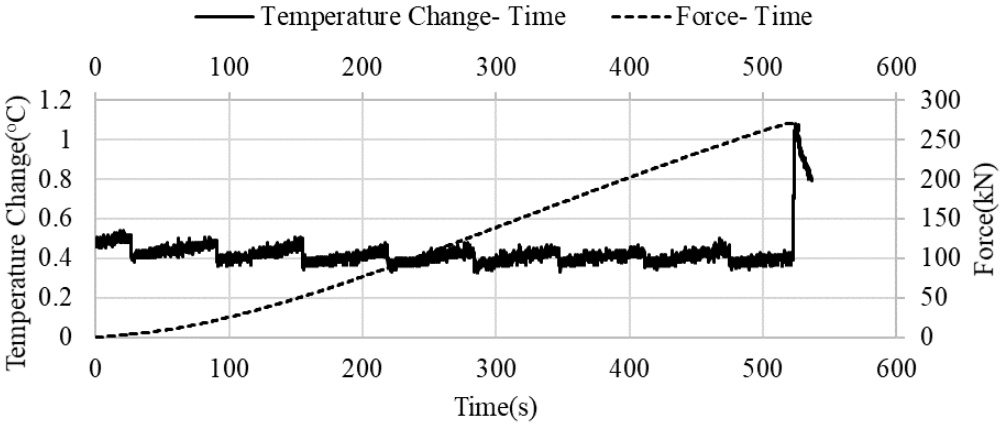

Figure C.5. Temperature change- Force- Time graph of the 63A-2 sample

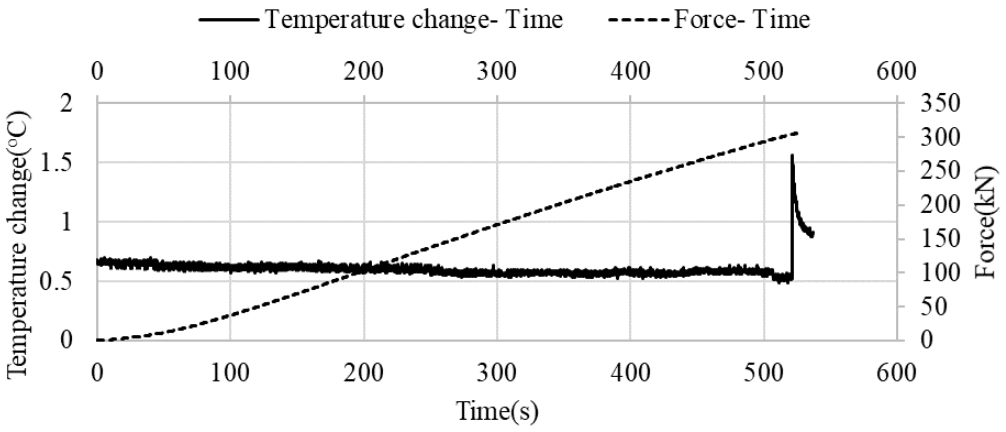

Figure C.6. Temperature change- Force- Time graph of the 63A-5 sample

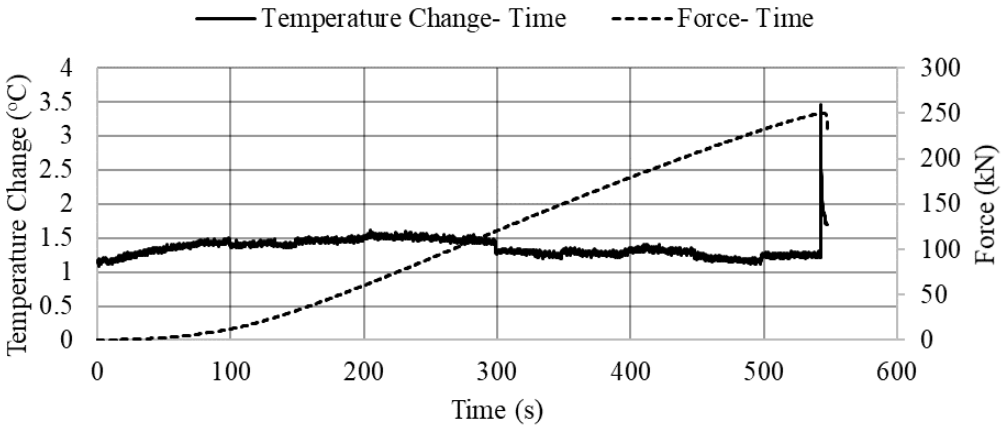

Figure C.7. Temperature change- Force- Time graph of the 63AA-2 sample

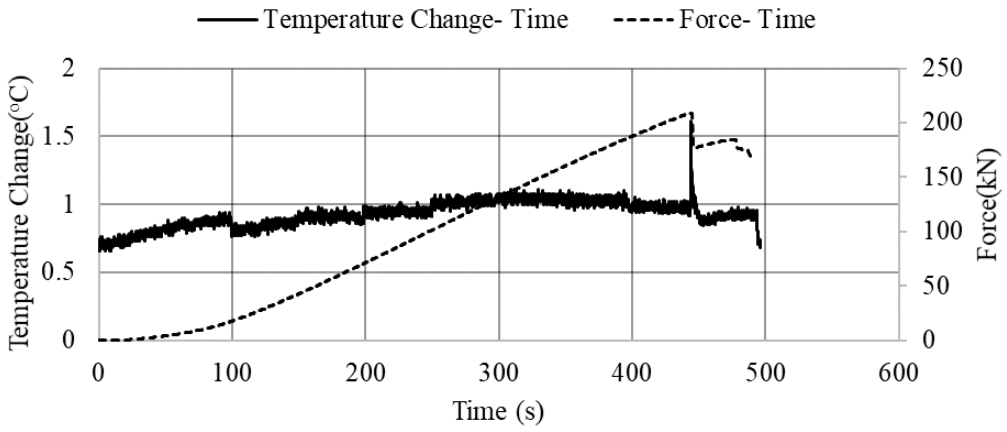

Figure C.8. Temperature change- Force- Time graph of the 63AA-4 sample

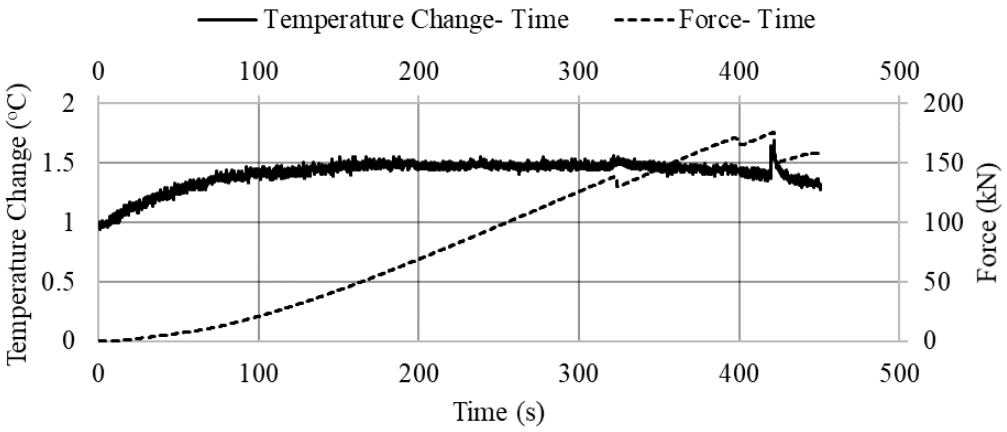

Figure C.9. Temperature change- Force- Time graph of the 63AA-6 sample

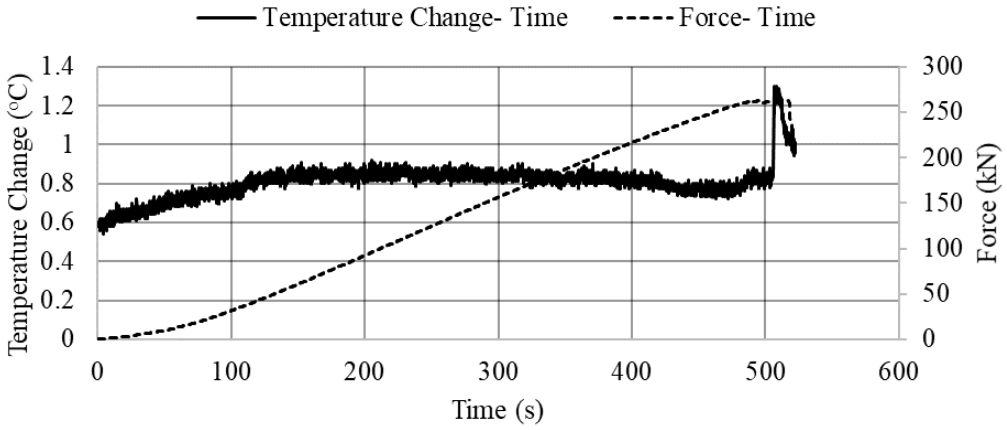

Figure C.10. Temperature change- Force- Time graph of the 63AA-9 sample

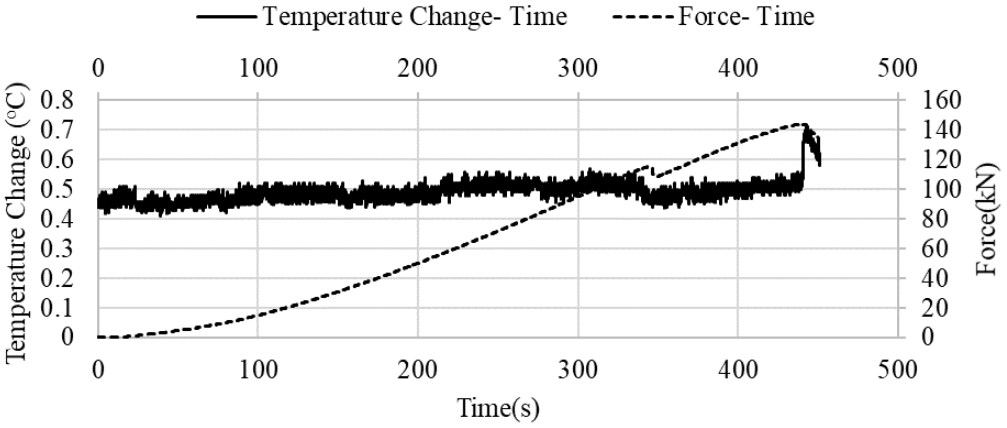

Figure C.11. Temperature change- Force- Time graph of the 53A-4 sample

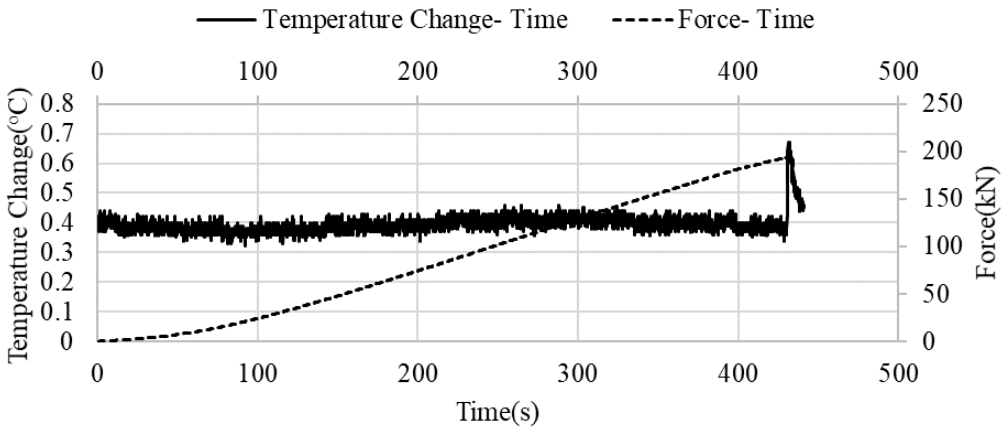

Figure C.12. Temperature change- Force- Time graph of the 53A-5 sample

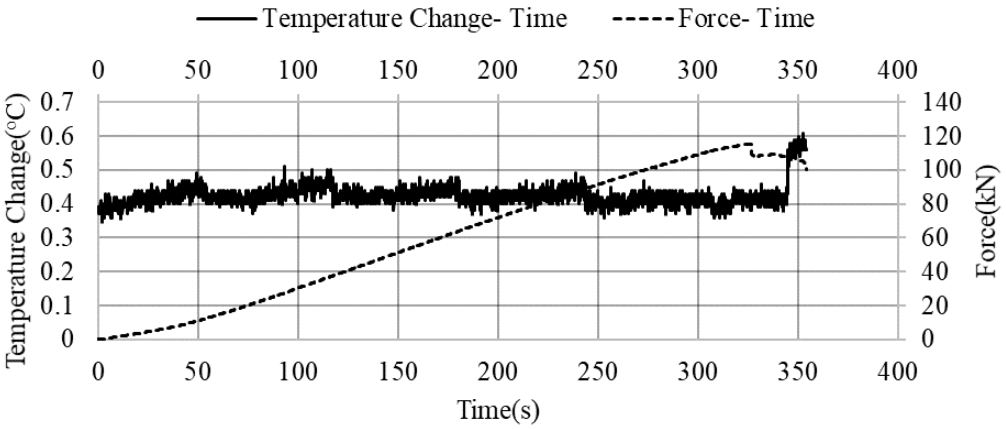

Figure C.13. Temperature change- Force- Time graph of the 42A-2 sample

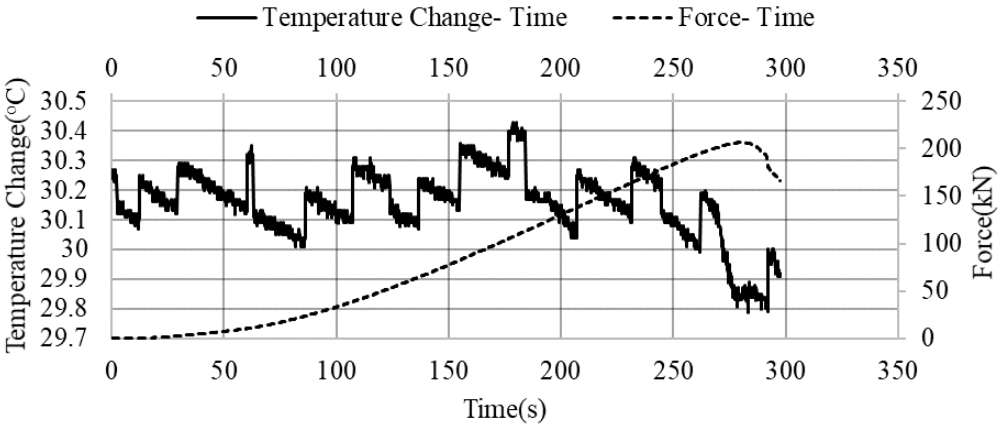

Figure C.14. Temperature change- Force- Time graph of the 63M-2 sample

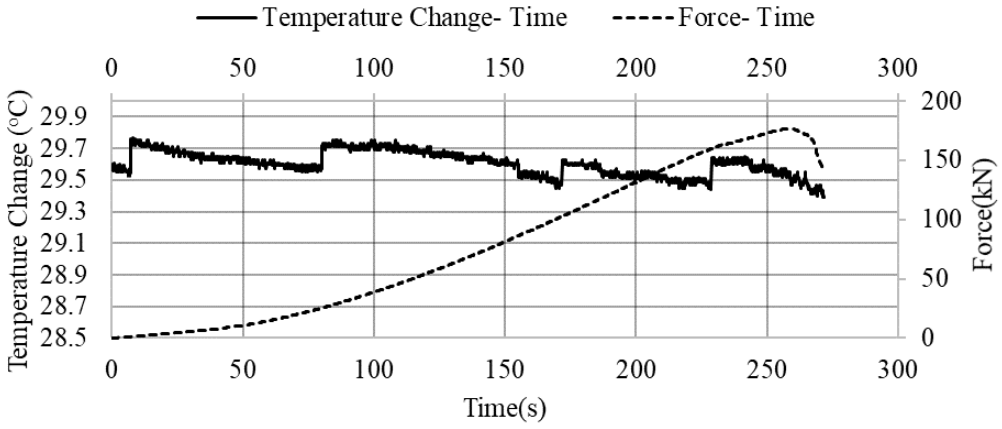

Figure C.15. Temperature change- Force- Time graph of the 63M-4 sample

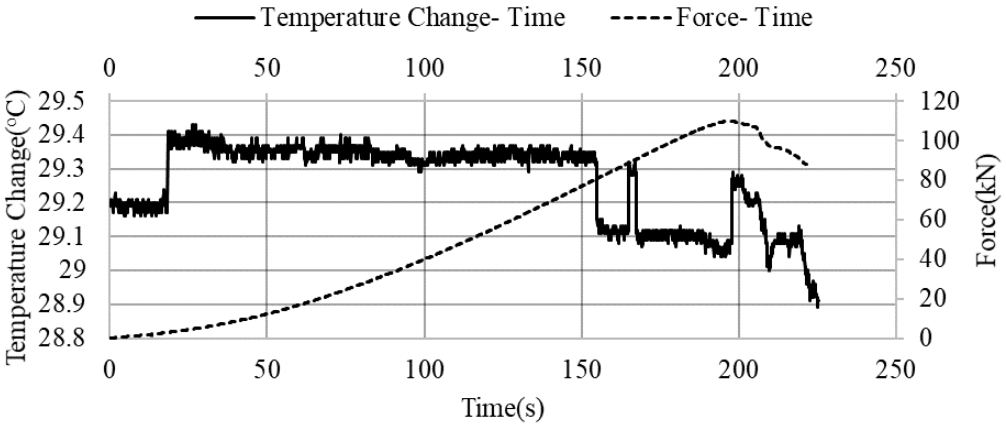

Figure C.16. Temperature change- Force- Time graph of the 53M-1 sample

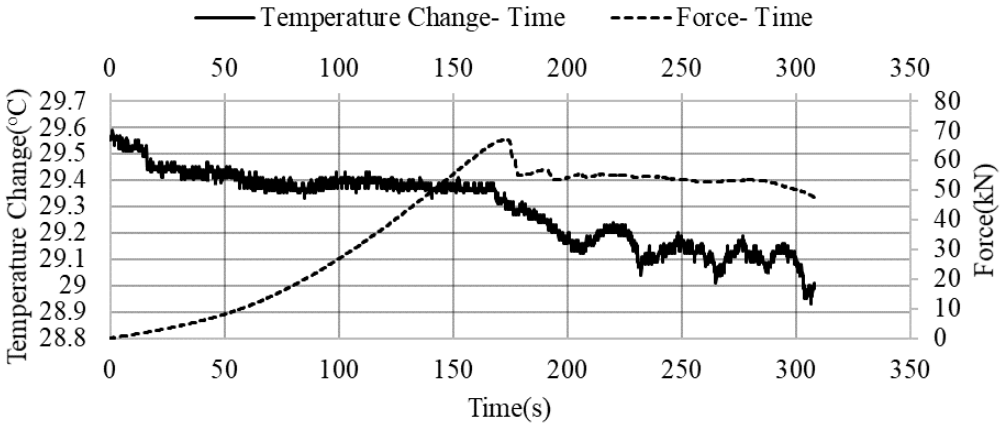

Figure C.17. Temperature change- Force- Time graph of the 53M-4 sample

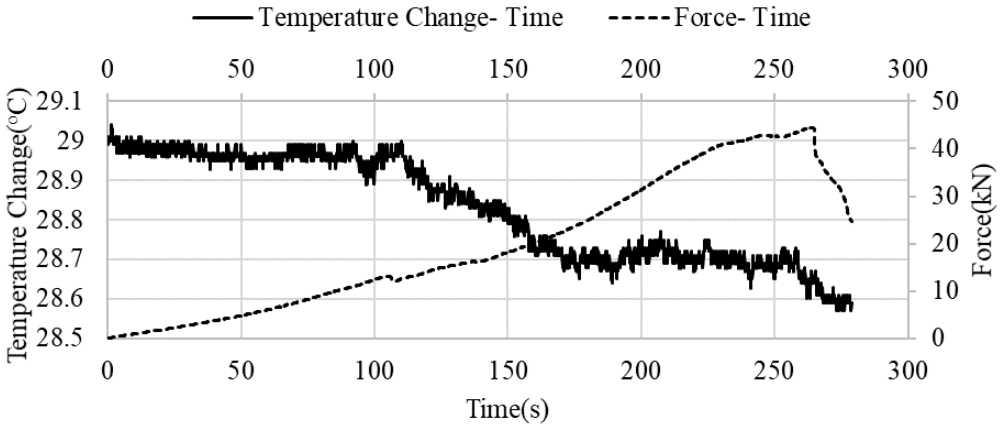

Figure C.18. Temperature change- Force- Time graph of the 42M-2 sample

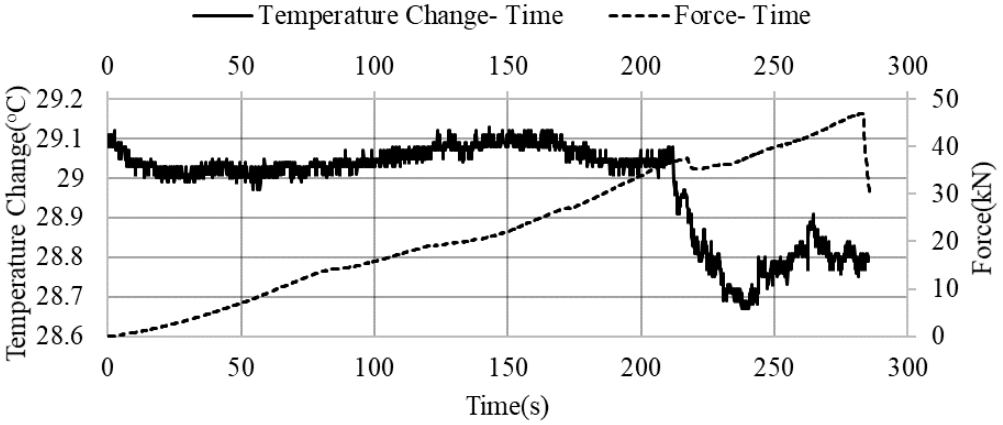

Figure C.19. Temperature change- Force- Time graph of the 42M-5 sample

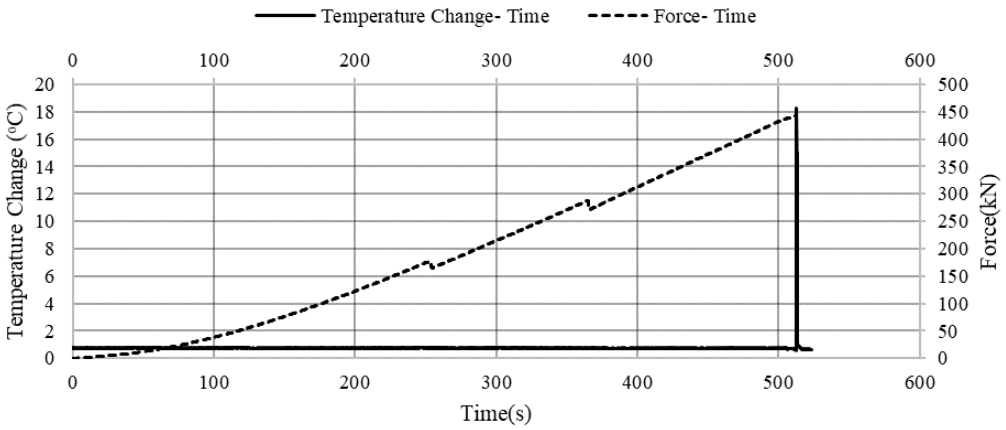

Figure C.20. Temperature change- Force- Time graph of the NLUCS-40 sample

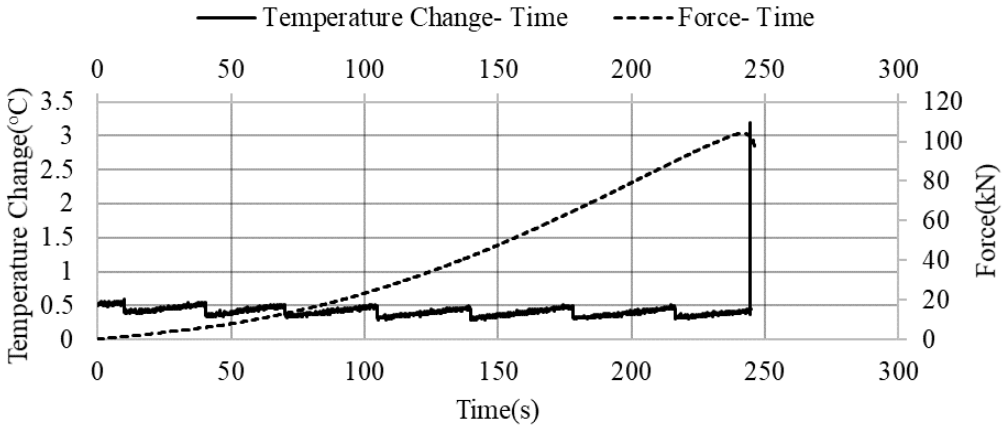

Figure C.21. Temperature change- Force- Time graph of the NLUCS-37 sample

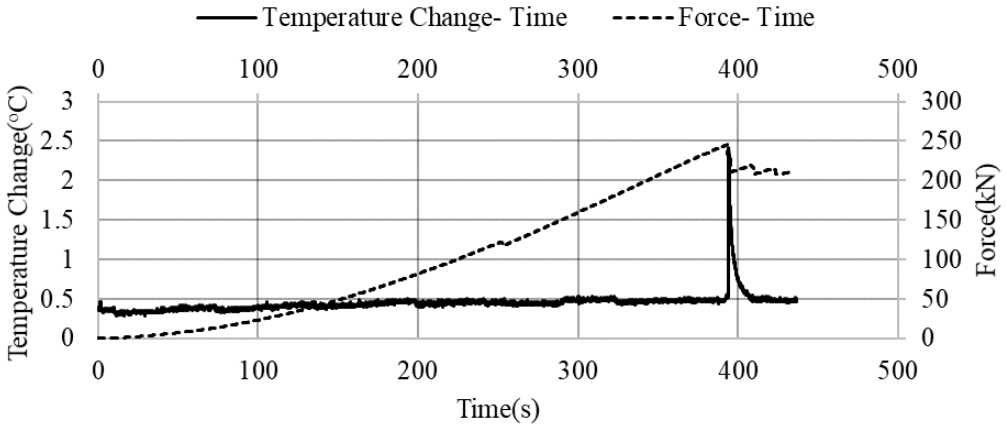

Figure C.22. Temperature change- Force- Time graph of the NLUCS-55 sample

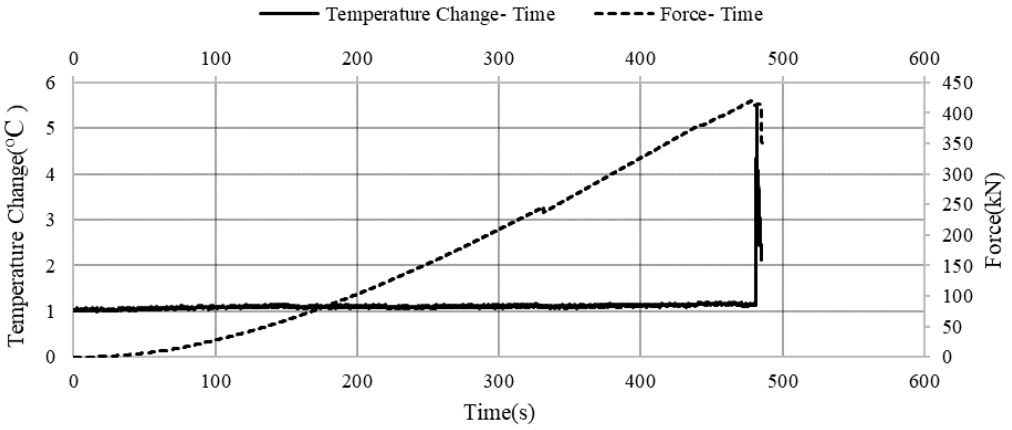

Figure C.23. Temperature change- Force- Time graph of the NLUCS-49 sample

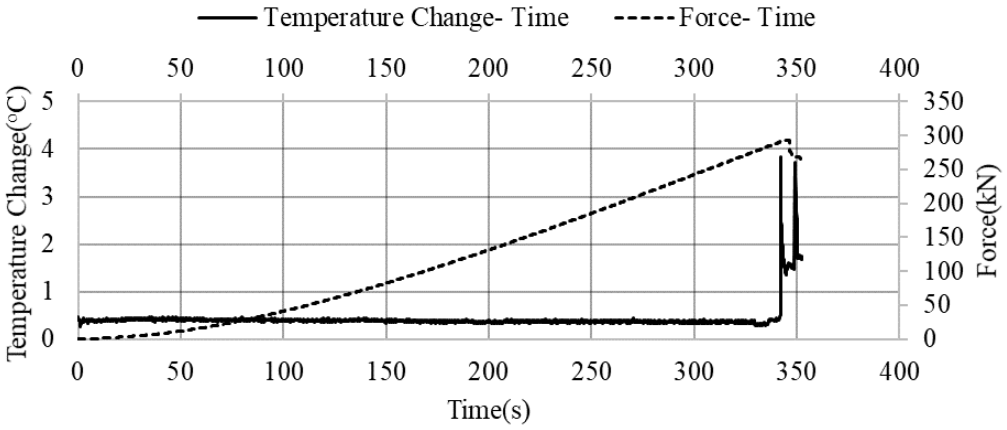

Figure C.24. Temperature change- Force- Time graph of the NLUCS-57 sample

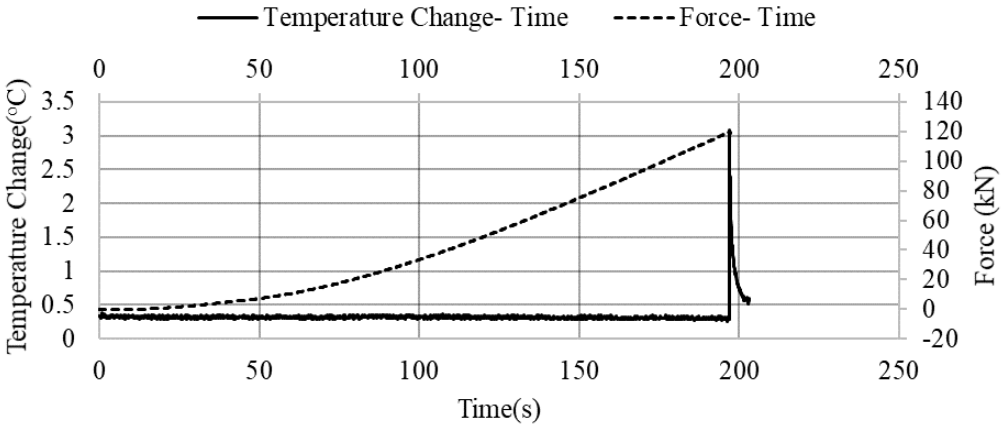

Figure C.25. Temperature change- Force- Time graph of the NLUCS-58 sample

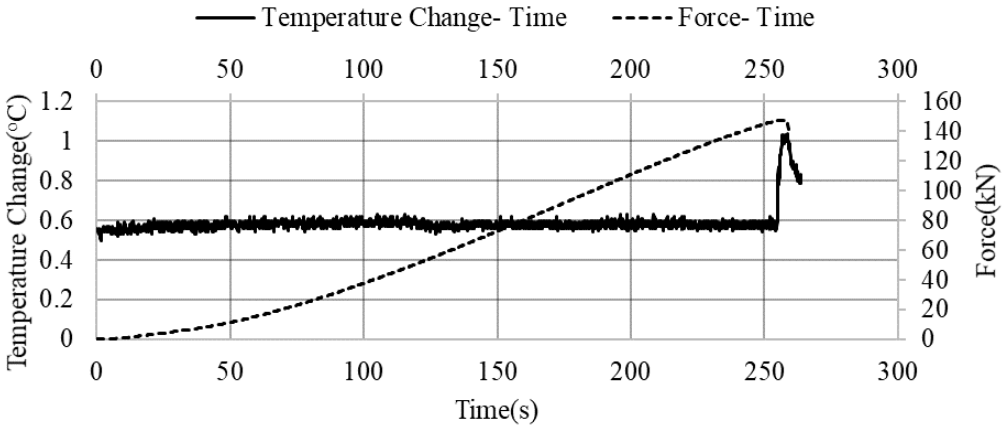

Figure C.26. Temperature change- Force- Time graph of the NLUCS-41 sample

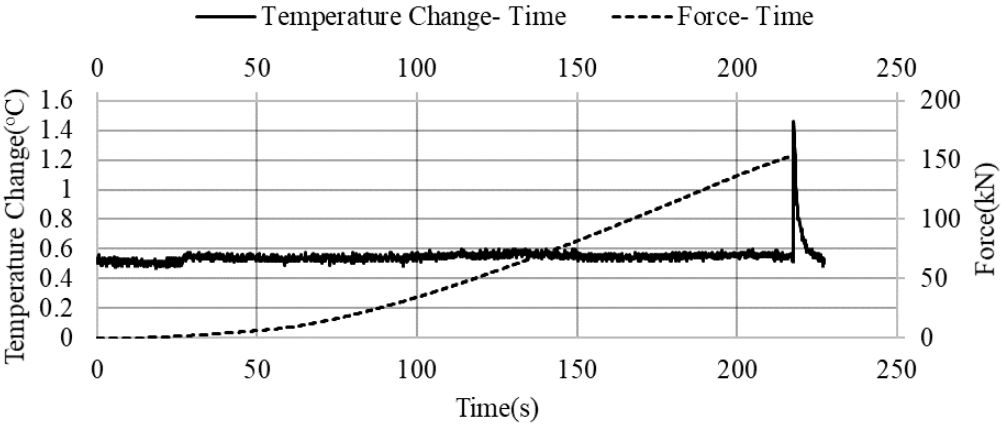

Figure C.27. Temperature change- Force- Time graph of the NLUCS-62 sample

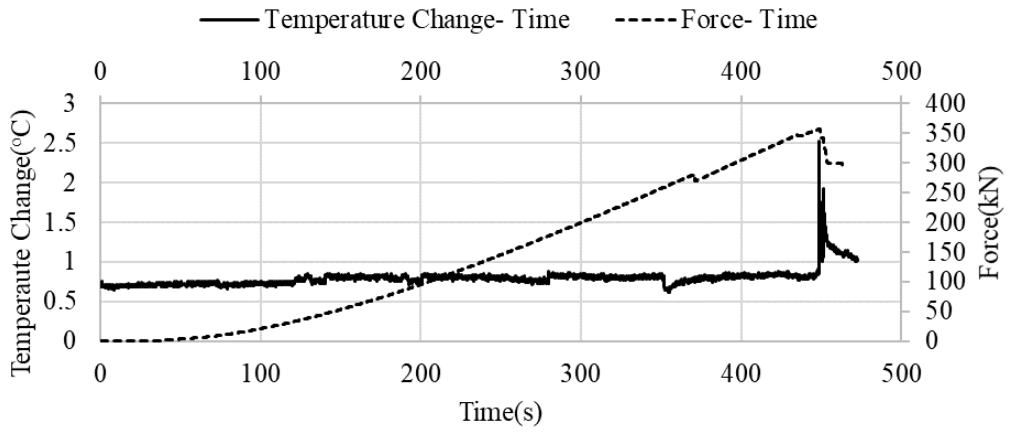

Figure C.28. Temperature change- Force- Time graph of the NLUCS-47 sample

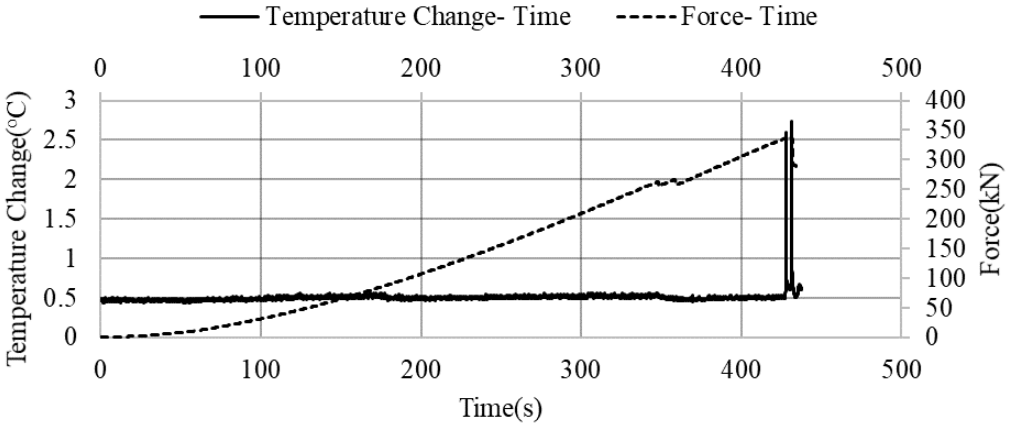

Figure C.29. Temperature change- Force- Time graph of the NLUCS-48 sample